E.O. Paton Electric Welding Institute of the National Academy of Science of Ukraine
International Association «Welding»

The Paton Welding Journal

11
2022

International Scientific-Technical and Production Journal ◊ Founded in January 2000 (12 Issues Per Year)

Address of Editorial Board
E.O. Paton Electric Welding Institute, 11 Kazymyr Malevych Str. (former Bozhenko), 03150, Kyiv, Ukraine
Tel./Fax: (38044) 205 23 90, E-mail: journal@paton.kiev.ua
https://patonpublishinghouse.com/eng/journals/tpwj

State Registration Certificate 24933-14873 ПР from 13.08.2021
ISSN 0957-798X, DOI: http://dx.doi.org/10.37434/tpwj

Subscriptions, 12 issues per year:
$384 — annual subscription for the printed (hard copy) version, air postage and packaging included;
$312 — annual subscription for the electronic version (sending issues in pdf format or providing access to IP addresses).

Representative Office of «The Paton Welding Journal» in China:
China-Ukraine Institute of Welding, Guangdong Academy of Sciences
Address: Room 210, No. 363 Changxing Road, Tianhe, Guangzhou, 510650, China.
Zhang Yupeng, Tel: +86-20-61086791, E-mail: patonjournal@gwi.gd.cn

The content of the journal includes articles received from authors from around the world in the field of welding, metallurgy, material science and selectively includes translations into English of articles from the following journals, published by PWI in Ukrainian:
- Automatic Welding (https://patonpublishinghouse.com/eng/journals/as);
- Technical Diagnostics & Nondestructive Testing (https://patonpublishinghouse.com/eng/journals/tdnk);
- Electrometallurgy Today (https://patonpublishinghouse.com/eng/journals/sem).

CONTENTS

ORIGINAL ARTICLES

*Translated Article(s) from «Automatic Welding», No. 11, 2022.

**Translated Article(s) from «Electrometallurgy Today», No. 4, 2022.

***Translated Article(s) from «Technical Diagnostics & Nondestructive Testing», No. 4, 2022.

DOI: https://doi.org/10.37434/tpwj2022.11.01

FEATURES OF THE INFLUENCE OF GRAIN BOUNDARIES DURING δ-γ-TRANSFORMATION ON THE FORMATION OF WELD METAL STRUCTURE (REVIEW)

V.V. Holovko

E.O. Paton Electric Welding Institute of the NASU
11 Kazymyr Malevych Str., 03150, Kyiv, Ukraine

ABSTRACT

A review of the literary research results is presented, on the basis of which it is seen that the algorithm of modeling the structural composition of the metal, prediction of its mechanical properties should contain a description of reactions on the formation and development of dendritic structure. The models built on the description of reactions of γ-α-transformation do not provide the possibility for evaluation of the process of the structure formation as an integral complex — from the beginning of dendrites nucleation to the final composition of the microstructure. The results of the studies, performed in recent decades describing the effect of refractory compounds, regarding inoculation to melts of low-alloyed steels and, in particular, welding pool, on the development of nucleation processes, growth and decay of dendrites during metal crystallization are presented. The probable influence of inoculants on the primary structure formation is shown in order to improve the properties of weld metal.

KEYWORDS: low-alloyed steel, welding pool, inoculation, dendrites, austenite, primary structure

INTRODUCTION

The widespread use of high-strength low-alloyed steels in manufacture of military equipment, infrastructure, power equipment and other structures of critical importance for Ukraine significantly increased the relevance of problems of providing high mechanical properties of welded joints. The complex of service properties of weld metal is determined by its structure. Therefore, a great attention in recent years has been paid to creating computer models for formation of weld microstructure and predicting its mechanical properties. The formation of microstructure of weld metal of low-alloy steels begins with the nucleation and growth of dendritic structure and processes of δ-γ-transformation [1, 2]. However, the main attention in these models is usually paid to the processes of γ-α-transformation [3, 4].

The processes of nucleation and decay of dendrites during cooling of the weld pool metal have a high activity at elevated temperatures, but until recently most experimental studies have been based on the observations of grain-boundary complexes at room temperature. The structure and features of the development of high-temperature complexes were more frequently studied by rapid cooling of a sample to room temperature. Moreover, in almost every case, the changes occurred in the structure and chemical composition of grains during cooling remained unknown. High-temperature S/TEM metallography, which has recently become available for studies, may turn out to be one of the best experimental methods for studying features of the dendritic structure development. The results of the experiments indicate that modern metallography allows observing the grain boundary complex under conditions of continuous cooling. Some observations of in situ reactions at elevated temperatures have become the basis for the creation of a numerical model of the dendritic structure formation [5], but this area of studies remains largely unexplored.

Studying the mechanisms of nucleation and growth of the new phase can potentially explain their spatial heterogeneity, as well as deepen understanding of methods for suppression of the coarse-grain structure formation that can be useful, for example, during thermostabilization of polycrystalline materials. The studies aimed at deepening understanding and control of processes on grain boundaries contribute to modeling interphase interactions and development of new materials with improved grain structure morphology and increased level of mechanical properties.

CHARACTERISTICS OF MAIN PROCESSES ON THE BOUNDARIES OF DENDRITIC STRUCTURE

The attempts to better understand the causes of microstructural formations with an increased tendency to brittle fractures of the metal motivated the development of process studies on the boundaries of structural grains. On the boundaries of dendrites, certain processes may proceed, associated with such properties as energy at the grain boundary, entropy, enthalpy and concentration of adsorbate. These processes may cause changes in such nonequilibrium properties of grain boundaries as mobility, cohesive strength and sliding resistance, which is a distinctive feature of in-

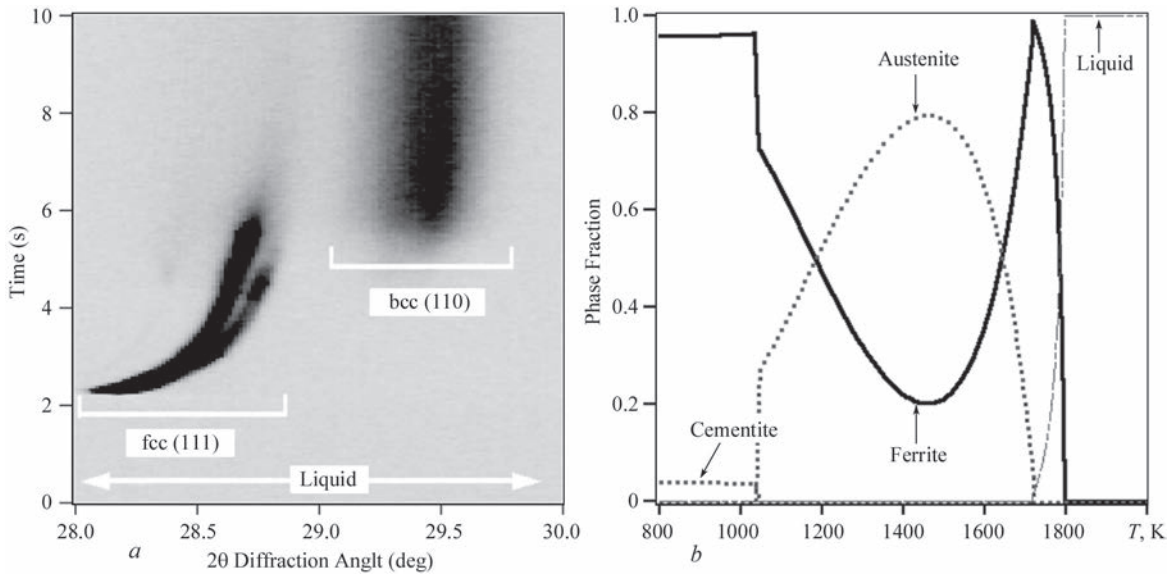

Figure 1. X-ray diffraction with resolution on cooling time of steel melt (*a*) and predicted equilibrium fraction of phase as a temperature function (*b*) [3]

tergranular interaction. Thermodynamics and kinetics of formation and decay of dendritic structure play a large role in the formation of microstructure and mechanical properties of welded joint metal.

In the peritectic systems, which include Fe–C alloys, at the stage of the dendritic structure formation, the high-temperature phase will easily overcool in the region of coexistence of high- and low-temperature phases, and the boundary between a high-temperature δ-phase and a liquid phase is the most probable place for nucleation of a low-temperature γ-phase (Figure 1).

The work of adhesion W_{ad} of the grain boundary is equal to the reverse work required for the transformation of the grain boundary into two free surfaces. For brittle fracture, such a dependence can be described by the ratio

$$W_{ad} = 2\gamma_S - \gamma_{GB},$$

where γ_S and γ_{GB} is the surface and grain boundary energy, respectively. Reduction in the energy of grain boundaries is associated with disordered transitions on grain boundaries, which involves an increase in the adhesion work and, therefore, grain boundary strength. However, in many systems studied experimentally, such transitions are associated with embrittlement of grain boundaries [6, 7]. Local features of the process can outweigh conventional thermodynamic considerations in such cases. For example, high-enthalpy bonds formed between adjacent structural lattices can significantly help to reduce marginal energy when interacting with low-enthalpy bonds in the interface, which can cause brittleness. This mechanism proposed by Luo et al. [7], allows explaining the brittleness in alloys. Alternatively, the energy on the grain boundary may be reduced by increasing entropy. An increase in entropy can be the result, for example, of an increase in a free volume of boundary or an increase in the concentration of liquants, which can also reduce the strength of the boundaries. The effect of a total work of adhesion on the strength and impact toughness of the metal is difficult to model in general on the basis of the abovementioned equation because the energy of two resulting surfaces is equally difficult to predict.

The coefficient of grain boundary self-diffusion D_{GB} can be described by a method similar to the volumetric self-diffusion coefficient using the frequency rate of jumps of atoms ν, the parameter of the lattice a_0, free energy of vacancies formation $\Delta G_{f,b}$, energy barrier of activation of migration atoms ΔG_m, geometric value g in the follwing way [8]:

$$D_{GB} = g\nu a_0^2 \exp\left(\frac{-\Delta G_{f,b}}{RT}\right)\exp\left(\frac{-\Delta G_{m,b}}{RT}\right).$$

The energy of grain boundaries is greatly affected by diffusion processes. Borysov et al. [9] for the first time suggested that a free energy of activation of grain boundary diffusion $\Delta G_b (=\Delta G_{f,b} + \Delta G_{m,b})$ is proportional to the corresponding free energy of diffusion activation in lattices ΔG_l minus free energy γ. Although, this rule is empirical, it gives a reasonable predictability in alloys. An energy decrease on the grain boundary, in which enthalpy prevails should increase the activation energy and reduce diffusion on the grain boundaries. However, when energy decreases, an increase in entropy prevails, which should lead to an increase in diffusion.

The processes of dendrites decay are associated with a decrease in the energy of grain boundaries. Thus, the measurement of energy of grain boundaries can be used to characterize transformations. For today, there are procedures that allow measuring changes in

the relative energy of the grain boundaries, but it is much more difficult to measure their absolute energy [10]. As a result, relative energy is usually measured. Relative energy of the grain boundary χ_{GB} along the adjacent surface of the grain χ_S can be expressed as a function of the diadric angle θ_S in the groove according to the equation [8]

$$\frac{\gamma_{GB}}{\gamma_S} = 2\cos\frac{\theta_S}{2}.$$

Using the analysis of Mullins [11], it is possible to determine the relative interphase energy of the grain boundary. However, this method includes a number of approximations and assumptions. For example, it is assumed that two surface energies are equal to each other, the grain boundary is normally located to the surface, the anisotropy of the interface energy is small. Although these assumptions are unfair for any boundary of one grain, it was found that for a large database on measuring dihedral angles of grain boundaries, the average value and the width of the distribution are reproduceable and significant values [12]. In recent years, the methods of X-ray in-situ diffraction, which have become widespread, have simplified these measurements. As a result, a special procedure was created for reliable measurement of the energy of grain boundaries [13].

Changes in the boundary energy of dendritic grains have an indirect effect on the distribution of γ-ferite grains in the metal. Comparative studies of anisotropy of distribution of grain size and anisotropy of grain boundary energy have shown that there is a reverse relationship between these two values in polycrystals, which involves the existence of relatively larger amount of grains with low boundary energy than high-energy grain boundaries [10, 14]. Thus, a change in the type of intergranular layer in the sample, which leads to changes in the energy of the grain boundaries, also affects changes in the size of grains in the process of transformation.

EFFECT OF WETTING PROCESSES ON DENDRITE DEVELOPMENT

On the boundaries of dendrites, a layer is formed, enriched with liquation elements, and also elements formed as a result of the interaction of dendrites with nonmetallic inclusions. The presence of these elements in the boundary layer determines the peculiarities of wetting the surface of dendrites, affects the kinetics of its development and the structural morphology. Dendrite wetting and development reactions have been the subject of study for the last several decades, as a result of which during the wetting process, a preliminary wetting stage was singled out [15, 16]. Preliminary wetting is the type of variation in the boundary structure, that occurs when the layer of material of a fixed equilibrium thickness is formed at the boundary interface in the thermodynamic vicinity of the wetting transition, i.e., near the temperature or composition, at which the wetting transition will occur. This term refers to the adsorption transition of the first kind, in which the film of the material separating two phases is broken both by adsorption composition as well as over the thickness.

In the process of growth, a dendrite moves in a metal melt. In this case, the boundaries of a dendrite are partially wettened with a liquid with a certain edge angle, when $\gamma_{lv} + \gamma_{sl} > \gamma_{sv}$ where γ_{lv} and γ_{sv} are the surface energy of the liquid and solid phase, and γ_{sl} is the surface energy of the boundary interface liquid/solid body. After the liquid completely wettens the surface and is distributed over it to form a continuous film, whose thickness depends on a number of liquation elements in the layer and has a surface energy $\gamma_{sv} \equiv \gamma_{lv} + \gamma_{sl}$ as is determined by thermodynamics. Preliminary wetting refers to the transition between partial and complete wetting, in which a thin layer of material is formed, which covers the surface, but has an equilibrium thickness, which is controlled by thermodynamic variables of the state (e.g., temperature, pressure) and does not depend on the amount of available liquid.

Wetting transitions can also occur at interfaces of solid bodies such as grain boundaries and phase boundaries. In addition, grain boundaries can be wettened either with a liquid or solid phase with a composition different from the main part, and in the first case, such wetting is associated not with a liquid metal and causes the embrittlement phenomenon [17, 18].

The process of crystallization of metal structure in welds of low-alloy steel, which begins with the epitaxial growth of delta-ferrite from the grains of a parent metal on the fusion surface because of high temperature gradients associated with the arc process, promotes the formation of a dendritic structure of a cell type with the grains of δ-ferrite, which have anisotropic columnar structure with main axes oriented in the direction of the maximum heat flow. At a further cooling of metal on the boundaries of cells δ/δ, allotriomphs of γ-phase are nucleated, which anisotropically grow along these boundaries, which leads to the formation of columnar grains of primary austenite. The kinetics of austenite formation and the size of its grains depends on the level of surface energy at the boundaries of δ/δ grains. The lower the surface energy on the dendrite boundaries, the higher the kinetics of austenite nucleation and the smaller the size of its grains [19].

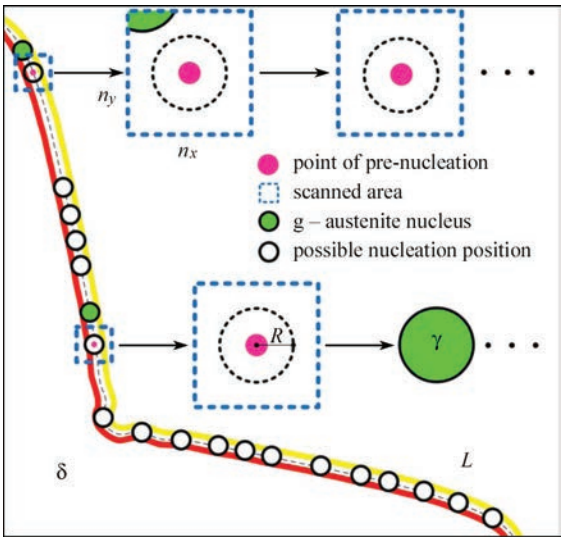

Figure 2. Schematic diagram of the austenitic phase formation [20]

EFFECT OF INOCULANTS ON KINETICS OF δ-γ-TRANSFORMATION

The process of metal crystallization in the conditions of peritectic reaction occurs in two separate stages. Initially, at the point of contact of three phases (liquid + δ-ferrite + γ-austenite) a bit lower than the peritectic temperature, a peritectic reaction ($L + \delta \rightarrow \gamma$) occurs, which leads to the formation of dendrites in the form of δ-ferrite with centers of γ-austenite nuclei at the interface boundary δ/*L*. In the future, the peritectic transformation begins with thickening of the γ-austenite layer on the surface of dendrites both due to δ-ferrite as well as liquid phases. The kinetics of this complex peritectic phase transition in the process of crystallization of steel depends on the composition of liquid layer on the surface of dendrites and the rate of melt cooling. The process of nucleation of γ-austenite represents a complex thermodynamic phenomenon in a nanoscale and is difficult for experimental observation, so for its research computer modeling methods are used.

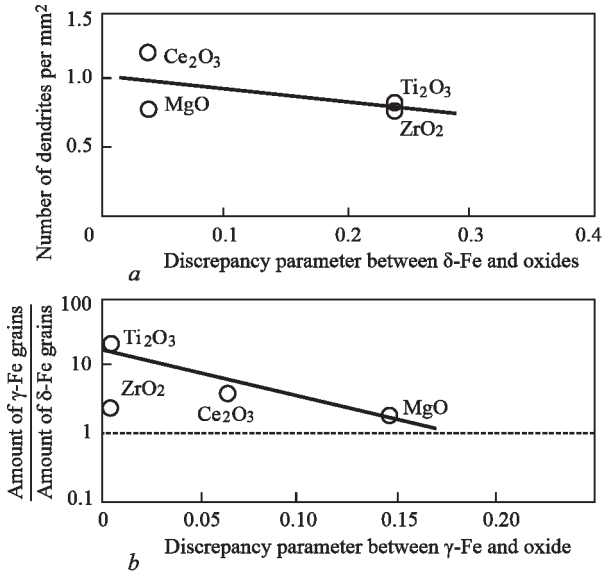

Figure 3. Effect of parameters of discrepancy of a crystal lattice of oxides to lattice parameters; *a* — δ-Fe; *b* — γ-Fe on the kinetics of crystallization [21]

The results of modeling, given in [20] showed (Figure 2) that the stages of γ-phase formation differ in the kinetics of the process. At the first stage, which corresponds to the preliminary wetting, on the dendrite surface, a limited number of nuclei of the new phase is formed. The formation of the main array of γ-phase occurs at the second stage.

Such a nature of the formation of nuclei is explained by the density of liquation elements in the liquid layer on the surface of dendrites. With a decrease in the melt temperature, the content of liquation elements in this layer increases, which affects the increased probability of the nucleation of a new phase.

At inoculation of refractory compounds to liquid metal, dendrites in the process of growth encounter nonmetallic inclusions and this may contribute to the change in the surface energy at the boundary interface *L*/δ.

The results of experiments on introduction of refractory oxides to metal metls, which are shown in Figure 3, *b*, demonstrate the ratio of an amount of γ-grains to δ-grains per unit area, applied to the diagram depending on the parameter of discrepancy of the lattice between γ-Fe and refractory oxide. The fact that this ratio increases with a decrease in the discrepancy parameter indicates that the rate of nucleation increases with an increase in the potential of this process. In other words, more than one nucleation event per one δ-grain occurs at the boundary interface δ/*L*.

The results shown in Figure 3, related to the effect of the discrepancy parameter on the size of the contact angle between the three phases — oxide, Fe(δ) and Fe(γ):

$$\cos\theta = (\gamma_{MO/Fe(\delta)} - \gamma_{MO/Fe(\gamma)})/\gamma_{Fe(\delta)/Fe(\gamma)}.$$

The mentioned results indicate that for a high rate of the γ-phase nucleation on the boundary interface δ/*L* (i.e. high value of cosθ), not only a low value of $\gamma_{MO/Fe(\gamma)}$ is required, which corresponds to the parameter of the discrepancy of lattice parameters between the oxide and γ-Fe, but also a high value of $\gamma_{MO/Fe(\delta)}$. On the upper diagram it is seen that this ratio does not increase with an increase in a number of particles per unit area N_A, indicating that the rate of nucleation of the γ-phase depends not only on a number of nucleation centers on the surface of dendrites. The value of a contact angle at the boundary of three phases has a much greater effect on the formation of a new phase.

Based on the mentioned results of the studies, it is seen that the algorithm of modeling the structural

composition of the metal, the prediction of its mechanical properties should contain a description of reactions on the formation and development of dendritic structure. The models that are built on the description of γ-α-transformation reactions do not allow evaluating the process of formation of structure as an integrated complex — from the beginning of the nucleation of dendrites to the final composition of the microstructure.

The recently published results of studies on the effect of inoculation of refractory compounds on melts of low-alloy steels, in particular, on weld pool metal [22], testify about the significant influence of physicochemical processes that occur at the stage of formation and development of dendrites, on the formation of a final structure of metal and confirm the need to take into account this stage of crystallization of welds when predicting their structural composition and the level of mechanical properties.

REFERENCES

1. Phelan, D., Dippenaar, R. (2004) Instability of the delta-ferrite/austenite interface in low carbon steels: The influence of delta-ferrite recovery sub-structures. *ISIJ Inter.*, 44(**2**), 414–421.
2. Yin, H., Emi, T., Shibata, H. (1999) Morphological instability ofd-ferrite/g-austenite interphase boundary in low carbon steels. *Acta Materialia*, 47(**5**), 1523–1535.
3. Babu, S.S., Vitek, J.M., David, S.A. et al. (2003) Characterization and prediction of austenite formation and decomposition in steel welds. *The Minerals, Metals & Materials Society*, **1**, 1–10.
4. Bhadeshia, H.K.D.H., Svensson, L.-E. (1993) *Modeling the evolution of microstructure in steel weld metal. Mathematical Modeling of Weld Phenomena*. Eds H. Cerjak, K.E. Easterling. Institute of Materials, London, 109–182.
5. Strickland, J., Nenchev, B., Dong, H. (2020) On directional dendritic growth and primary spacing — A review. *Crystals*, **10**, 627. DOI: https://doi.org/10.3390/cryst10070627
6. Richter, G., Rühle, M. (2006) Insight into the atomic-scale mechanism of liquid metal embrittlement. *Appl. Phys. Lett.*, **89**, 121911. DOI: https://doi.org/10.1063/1.2356322
7. Luo, J., Asl, M., Kiely, C.J., Harmer, M.P. (2011) The role of a bilayer interfacial phase on liquid metal embrittment. *Science 23 Sep. 2011*, **333**, 6050, 1730–1733. DOI: https://doi.org/10.1126/science.1208774
8. Cantwell P.R., Tang M., Dillon S.J. et al. (2014) Grain boundary complexions. *Acta Materialia*, **62**, 1–48.
9. Borisov, V.T., Cherepanov, A.N., Predtechenskii, M.R., Varlamov, Yu.D. (2003) Effect of wettability on the behavior of a liquid drop after its collision with a solid substrate. *J. of Applied Mechanics and Technical Physics*, **44**, 803–808.
10. Rohrer, G.S. (2011) Grain boundary energy anisotropy: A review. *J. of Materials Sci.*, **46**, 5881–5895.
11. Mullins, W.W. (1957) Theory of thermal grooving. *J. of Applied Physics*, **28**, 333. DOI: https://doi.org/10.1063/1.1722742
12. Dillon, S.J., Rohrer, G.S. (2009) Mechanism for the development of anisotropic grain boundary character distributions during normal grain growth. *Acta Materialia*, 57(**1**), 1–7.
13. Babu, S.S., Specht, E.D., David, S.A. et al. (2007) Time-resolved X-ray diffraction investigation of austenite and transformation to bainite. In: *Proc. of the 1st Inter. Sym. on Steel Science (IS3-2007). The Iron and Steel Institute of Japan*, 93–99.
14. Rohrer, G.S., Anthony, J.G., Rollett D. (2008) A model for the origin of anisotropic grain boundary character distributions in polycrystalline materials. *Applications of Texture Analysis*, **17**, 10. https://doi.org/10.1002/ 9780470444214.ch36
15. Cahn, J.W. (1977) Critical point wetting. *The J. of Chemical Physics*, **66**, 8. DOI: https://doi.org/10.1063/1.434402
16. Ebner, C., Saam, W.F. (1977) New phase-transition phenomena in thin argon films. *Physical Review Letters*, 38(**25**), 1486–1489.
17. Straumal, B., Baretzky, B. (2004) Grain boundary phase transitions and their influence on properties of polycrystals. *Interface Sci.*, 12(**2–3**), 147–155.
18. Chatain, D., Rabkin, E., Derenne, J., Bernardini, J. (2001) Role of the solid/liquid interface faceting in rapid penetration of a liquid phase along grain boundaries. *Acta Materialia*, 49(**7**), 1123–1128.
19. Porter, D.A., Easterling, K.E., Sherif, M.Y. (2009) *Transformations in metals and alloys*. Third Ed. by Taylor & Francis Group. International Standard Book Number-13: 978-1-4398-8357-0 (eBook-PDF).
20. Yang, Y., Luo, S., Wang, P. et al. (2021) Multiphase field modeling of dendritic solidification of low-carbon steel with peritectic phase transition. *The Minerals, Metals & Materials Society and ASM Inter.* DOI: https://doi.org/10.1007/s11663-021-02297-1
21. Suito, H., Ohta, H., Morioka, S. (2006) Refinement of solidification microstructure and austenite grain by fine inclusion particles. *ISIJ Inter.*, 46(**6**), 840–846.
22. Holovko, V.V., Stepanuk, S.M. (2022) Nanoscale modification of weld metal microstructure. *Global J. of Science Frontier Research; 1 Interdisciplinary*, 22(**1**), 10.

ORCID

V.V. Holovko: 0000-0002-2117-0864

CORRESPONDING AUTHOR

V.V. Holovko
E.O. Paton Electric Welding Institute of the NASU
11 Kazymyr Malevych Str., 03150, Kyiv, Ukraine.
E-mail: v_golovko@ukr.net

SUGGESTED CITATION

V.V. Holovko (2022) Features of the influence of grain boundaries during δ-γ -transformation on the formation of weld metal structure (Review). *The Paton Welding J.*, **11**, 3–7.

JOURNAL HOME PAGE

https://patonpublishinghouse.com/eng/journals/tpwj

Received: 08.09.2022
Accepted: 29.12.2022

DOI: https://doi.org/10.37434/tpwj2022.11.02

PROBLEMS AND PROSPECTS OF STUDYING THE PROCESSES OF SELECTIVE LASER MELTING OF MATERIALS FOR AEROSPACE ENGINEERING (REVIEW)

M.V. Sokolovskyi

E.O. Paton Electric Welding Institute of the NASU
11 Kazymyr Malevych Str., 03150, Kyiv, Ukraine

ABSTRACT

In this work, a literary review of the materials devoted to different directions of research of SLM technology was made, in order to determine the relevant directions of research of different scientific components of the process of selective laser melting (SLM), as well as technological measures affecting the final structure, mechanical and service characteristics of a manufactured part. The directions of scientific works considered in this review were: research and deepening knowledge on the influence of the energy component of SLM process; possibilities of SLM process modification by the control of laser defocusing amount; study of modes and methods of SLM processing, as well as final microstructure of the specimens; study of corrosion resistance of products, manufactured using SLM. Based on the results of the literary analysis, the problems and prospects of studying SLM processes for materials of aerospace industry are shown, the need in creating a systematic comprehensive approach to the study of the components of SLM process, as well as deepening knowledge about the technological capabilities of its application is substantiated.

KEYWORDS: selective laser melting (SLM), additive manufacturing, powder metallurgy, control of focal spot size, scanning strategy, aerospace industry metals

INTRODUCTION

Selective laser melting (SLM) is one of the modern technologies of additive manufacturing, used in manufacture of products of a complex shape and structure from metal powders. This process consists in successive layer-by-layer melting of powder material by powerful laser radiation. Selective laser melting allows creating unique products of a complex profile without the use of machining or complex expensive fixtures, in particular, due to the possibility of controlling the physico-mechanical properties of products.

SLM technologies have the ability to solve complex problems of aerospace, power, oil and gas and other mechanical engineering industries, as well as of metal processing, medicine and jewelry. However, despite the numerous advantages, the main disadvantage of SLM, compared to methods of manufacturing various parts and structures based on the deposition process, is a relatively low productivity of this technology. Increase of laser beam diameter improves SLM build-up rate, but leads to loss of precision. At the same time, it is necessary to understand that in order to produce a fully solid piece without defects (pores or other stress raisers), the metal powder particles should be completely melted. In this case, it is rational to use sufficiently high laser power. It should be noted, however, that at selection of excess power, the process may go into a less stable form, resulting in appearance of such defects as "balling effect" and excess local concentration of internal stresses that may cause deformation of the part or initiation of internal microcracks [1, 2].

These and other issues [3–5] raise the problem of studying the SLM-process components. For this purpose a number of works were reviewed, which are related to SLM processing of some of the most common aerospace materials, namely AISI 316L steel, as well as Inconel 625 and 718 alloys. All these materials are extensively applied in the aerospace industry due to their corrosion resistance and high working temperatures.

The objective of this work is determination of relevant direction of studying different scientific components of SLM process, as well as technological measures, affecting the final structure of the manufactured part and its mechanical and service characteristics.

ANALYSIS OF DIFFERENT DIRECTIONS OF STUDYING THE SLM PROCESS COMPONENTS

The issue of studying the selective laser melting process is complex. It requires analysis of various factors, which would take into account all the mechanical and physical properties of the manufactured structures and parts. Information and analytical studies showed that different methods are used to solve this complex of problems. These methods are concentrated on optimization of one or two characteristics, influencing the running of the process of analysis of different ways of studying the SLM process components. The scientific works discussed in this study are focused on SLM process optimization by the following methods:

- investigations and deepening of the knowledge on the influence of energy components of SLM process on its result;
- possibilities of modification of SLM process by controlling the laser defocusing amount;
- determination of the modes and methods of SLM processing, as well as final microstructure of the specimens. Studying the corrosion resistance of SLM products.

INVESTIGATIONS OF ENERGY COMPONENT OF SLM PROCESS

Earlier investigations [1–6] of the energy component of SLM process showed that laser power and energy density are important factors, influencing the quality of parts manufactured by this technology. The methods developed in works [3–5] would be beneficial for studying this process parameters. These methods involve orthogonal array design and analysis of HAZ dimensions. Thus, application of the normalized processing map, developed in the work by Thomas [6], which brings to the fore the use of dimensionless parameters of the process energy component for calculations, leads to the conclusion that the most significant factor is the normalized laser power q^*, influencing a large number of process variables. The same model emphasizes the importance of the magnitude of normalized equivalent energy density (E_0^*) as a key parameter influencing the properties of the manufactured parts [6–11].

In the study by Jiang [12], a normalized dimensionless technology map of SLM process was accepted for experiment planning. The effectiveness of its application was demonstrated by papers [2, 7, 9, 10]. This work analyzed the influence of normalized equivalent power density E_0^* and dimensionless laser density q^* on SLM process to study the developing defects, shape of the melt pool, as well as primary interdendritic spacing for the microstructure of parts built from 315L steel by SLM method.

Dimensionless laser power q^* is found from the following equation:

$$q^* = Aq/[R\lambda(T_m - T_0)], \quad (1)$$

where A is the surface absorption factor; q is the laser power (W); R is the laser beam radius (m); λ is the heat conductivity (W·m^{-1} K^{-1}); T_m is the melting temperature (K); T_0 in the melting temperature of the initial (or powder) material (K).

Equivalent power density E_0^* can be represented by the following equation (2):

$$E_0^* = q^*/(v^* l^* h^*) = [Aq/2vlh]\ [1/pC_p(T_m - T_0)], \quad (2)$$

where q^* is the dimensionless power density (1); v^* is the dimensionless speed of laser scanning; l^* is the dimensionless height of the deposited layer; h^* is the dimensionless distance between the axes of scan passes (3):

$$v^* = vR/a,\ l^* = 2l/R,\ h^* = h/R, \quad (3)$$

here, v is the laser scanning speed (m/s); α is the heat conductivity coefficient in the melting point (m^2·s^{-1}); l, h is the layer thickness (μm) and distance between the scan pass axes (μm).

The dendrite microstructure obtained during the experiment through calculations by this model, reflects a combined influence of the process parameters and features of material phase composition on its final state in the HAZ. The study revealed that the low values of E_0^* parameter can lead to increase of the cooling rate, resulting in a structure with smaller interdendritic spacing. It was experimentally derived in the work that when manufacturing a part which must withstand considerable tensile stresses, the process parameters should be selected so as to ensure relatively low E_0^* values. In works [1, 11] it was proved that the shape of the melt pool, as well as the size of the HAZ are controlled by laser power. The specimen studied in the work by Sun et al. [1] had a melt pool of a narrow deep shape, demonstrating better mechanical properties compared to a specimen with a wide and shallow shape of the weld pool. The narrow deep pool is formed at a combination of the high value of dimensionless parameter of laser power, q^* and sufficiently high value of normalized equivalent power density E_0^*. However, the scientific work by Ma et al. [11] revealed that such a combination increases the instability of the melt pool, causing *keyhole* defects. It is pointed out that for each technical assignment there exist optimal values of q^* and E_0^* parameters. Here, the results of work [12] emphasize that at application of SLM technology without subsequent heat treatment to relieve the residual stresses, high complex characteristics of strength and ductility of the produced part can be achieved with the use of a rather low value of E_0^* parameter. Influence of process parameters on the microstructure of stainless steel 316L was also studied in the work by Kurzynowski et al. [13]. However, reaching similar conclusions, he noted that the SLM process is highly localized and rapid that made it complicated to achieve a deeper understanding of the mechanism of formation of various morphologies of the material, as well as microstructures of the manufactured part surfaces. So far just a few investigations were devoted to this problem, in the majority of which experimental results were studied using local X-ray visualization [13, 14].

An alternative method of studying the structure of parts produced by SLM process is computational modeling and predictive modeling. This method is becoming ever wider accepted in modern research on this subject. So, the work by Tang et al. [15] demonstrated a 3D model developed for simulation of for-

mation of traces of 316L stainless steel melt during SLM process. Here it was proved that surface tension and recoil pressure were exactly the two key factors in formation of the macrostructure of single-pass deposited specimen of both spherical and irregular shapes.

Work [16] is a study of the features of the surface of Inconel 718 specimens, produced by SLM at different laser power and scanning speeds, while correlating the combinations of these values with the known principles of molten powder behaviour. Both experimental and model approaches were applied for investigation of surface morphology and solidification microstructure of Inconel 718 alloy, using a mezoscale 3D model of the height function of lattice-Boltzmann method (HF-LBM) [17, 18]. It was found that it is exactly the surface tension, and not the recoil pressure, as previously thought [18], that sucked the molten powder into the melt pool during SLM. As regards the low level of applied energy, the powder melt merges with unmolten particles before penetrating into the melt pool, which was determined to be the main cause for formation of surface fluctuations in the melt pool and further formation of closed surface pores. Deng et al. [19] noted that when the laser input energy exceeds the limit, the "balling effect" will be manifested in the melt pool.

In his dissertation Kempen et al. [20] came to the conclusion that the first step for enhancement of SLM process capabilities is précising the scanning path of single-line tracks with different combinations of laser power and scanning speed for a preset laser beam diameter and layer thickness. After that he stated the need to perform structure analysis in the melt pool, in order to select an optimal parameter series for further construction of a 3D-model of the manufactured part. The next step mainly includes determination of optimal scanning strategy and hatch spacing between the adjacent tracks. So, for instance, Wang et al. [21], as well as Yadroitsev et al. [22], studied the correlation of heat input and material morphology obtained after single-line scanning, namely in these works the influence of linear energy density Θ — a ratio of laser power P and scanning speed v — on the final structure of SLM part was investigated. On the whole, these studies confirm the theories given in works [14, 16, 20], but question the use of experimental single-pass specimens, as a mulitpass procedure is envisaged in practical manufacturing of the parts.

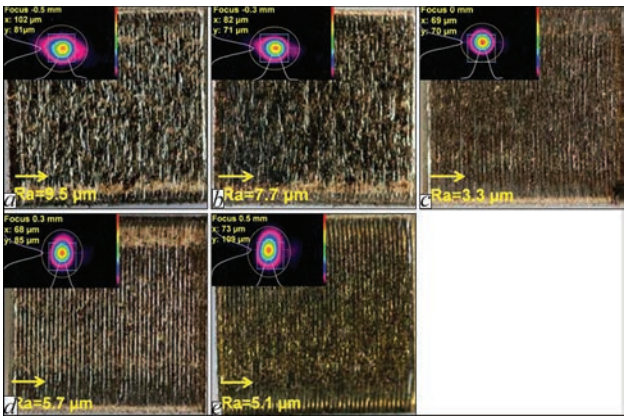

Figure 1. Macroscopic top view of SLM specimens produced with different defocusing amount, mm: *a* — –0.5; *b* — –0.3; *c* — 0; *d* — 0.3; *e* — 0.5 [25]

POSSIBILITIES OF SLM PROCESS MODIFICATION BY CONTROLLING LASER DEFOCUSING AMOUNT

In his study Promopattum et al. [23] reported that application of high laser power and small beam diameter does not lead to a stable SLM process, as concentration of a large amount of energy in a small point may lead to evaporation of the processed material and keyhole formation. After experimental tests he came to the conclusion that at a constant scanning speed increase of the laser spot diameter allows application of high-power lasers without overheating of the processed material. It, however, complicates maintaining the specified level of accuracy and surface roughness.

This problem can be prevented using the shell-core strategy, which envisages a set of high performance working parameters for the part core and high-precision operating modes for the surface layers of the manufactured part [24]. This procedure combines the high speed, geometrical precision and low surface roughness. The set of the main parameters of the operating modes in such a case usually includes increase of the defocusing amount that leads to increase of the melt pool size and greater thickness of the processed layer. Here, the need to maintain the minimal required power to conduct an SLM process operation is pointed out.

In work [25] the melt pool morphology was analyzed, taking into account SLM parameters, including laser power, scanning speed and defocusing distance. The bulk energy density, normalized enthalpy and an analytical approach using Rozenthal equation were applied to correlate the melt pool morphology and heat input. This equation was derived for classical fusion welding methods. However, due to the closeness of these processes to those occurring at SLM, Metelkova et al. [25] decided to apply the design parameters derived from this calculation equation with its condi-

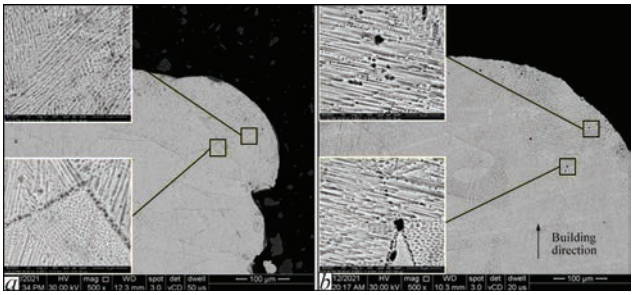

Figure 2. Porosity at negative (*a*) and positive (*b*) defocusing amount [27]

tions for computation of SLM processes. During work performance, the suitability of normalized enthalpy as a design parameter for prediction of the melt pool depth was emphasized, and the usability of Rozenthal equation for pool width prediction was proved. This investigation shows that realization of the proper defocusing amount may lead to a significant increase of potential productivity of the laser unit. However, one can note that the increase in productivity is achieved due to partial increase in roughness (Figure 1).

In work [26] the influence of negative (–0.5 mm, –0.3 mm) and positive (0.3 mm, 0.5 mm) values of defocusing distance in part manufacturing by SLM was conducted (Figure 2), to assess the influence of the defocusing amount on the melt zone width, height and depth, surface roughness, its density and tensile strength of parts.

One can see from the results of work [27] that the defocusing distance has a great influence on surface quality. Application of negative defocusing distances provides a melting mode in Inconel 625, where the melt pool is of a small depth and spherical shape. And contrarily, use of positive distances generates a keyhole melting mode, where the melt pool depth is greater than its half-width.

However, McLouth et al. [28] noted in his research results that despite the similarity of different processes of additive manufacturing, the influence of the defocusing amount on porosity and microstructure cannot be generalized for the processes for even one alloy type, as this value is influenced by a large number of parameters.

STUDYING SLM-PROCESSING MODES AND METHODS, FINAL SPECIMEN MICROSTRUCTURE AND CORROSION RESISTANCE OF SLM PRODUCTS

When trying to get a deeper insight into SLM, significant attention is attracted to studying the factors affecting the material corrosion resistance. Resistance of a heat-treated specimen of 316L steel, where the melt pool temperature reached a subcritical value of 950 °C, was better than that of the specimen, where temperature reached 1100 °C [27]. Another work [29] showed that residual compressive stresses, caused by SLM processes, can improve the growth of the passive film, and reduce the driving force of repassivation, leading to a slight improvement of point corrosion resistance of 316L steel. Pores detected in SLM specimens, compared to those made by traditional technologies, were described as such which promoted cracking and pitting which probably formed in extremely aggressive media [30]. Other defects, forming during SLM, namely defects of melt pool boundaries, nonequilibrium microstructure and nonuniform distri-

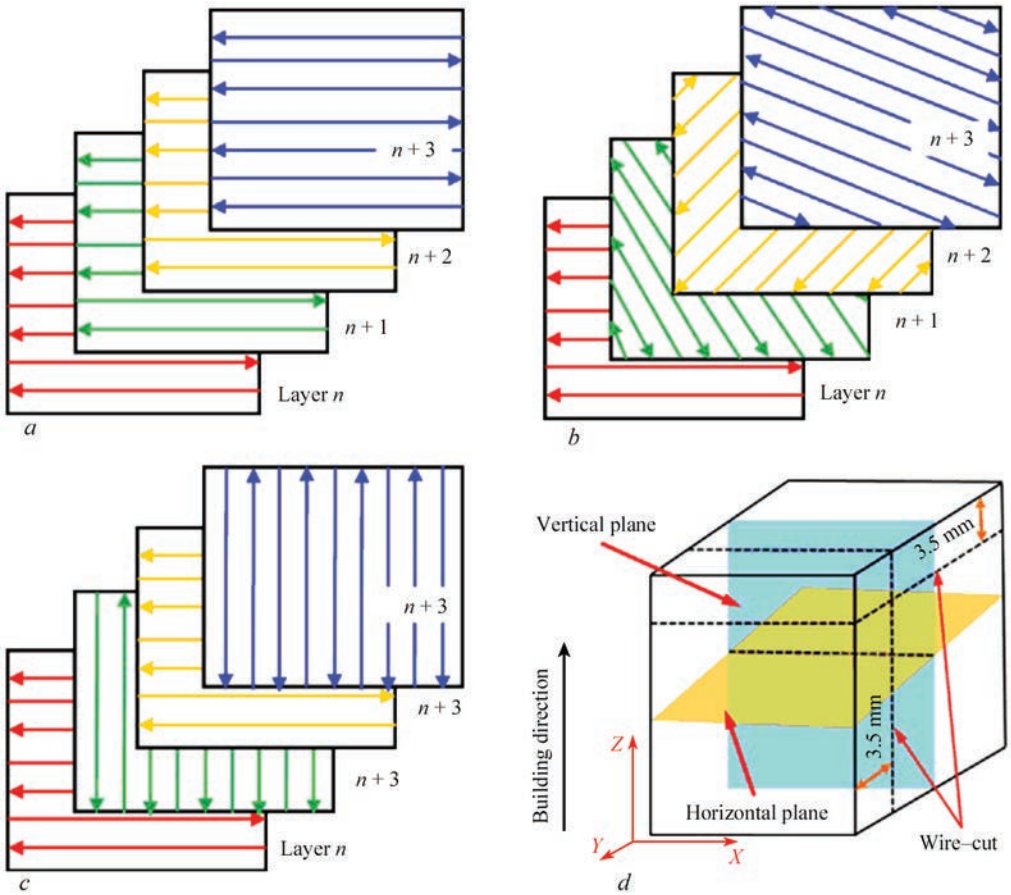

Figure 3. Scanning strategies used in [33]: *a* — without rotation; *b* — with rotation by 67.5°; *c* — with rotation by 90°; *d* — indication of vertical and horizontal planes

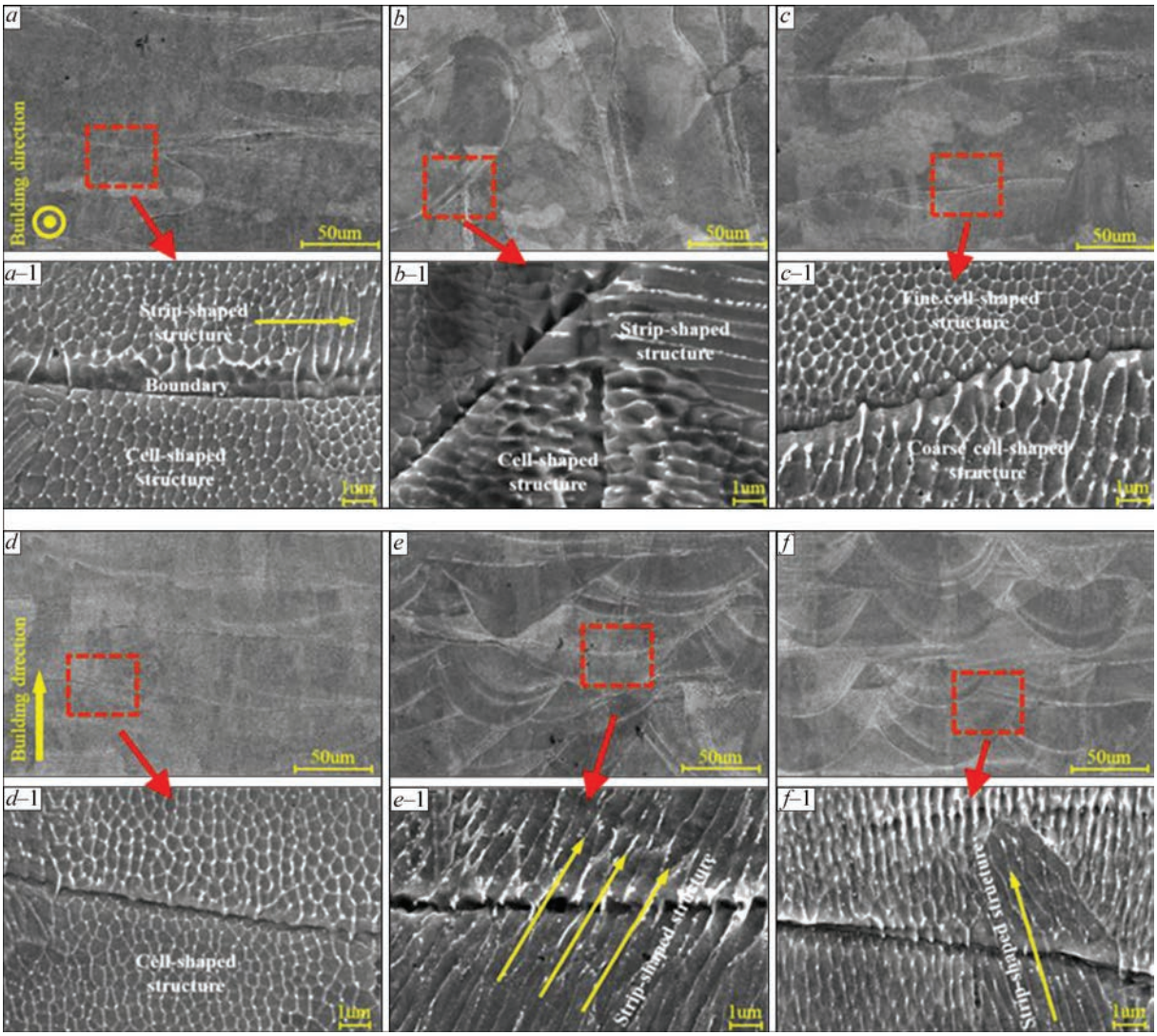

Figure 4. SEM micrograph of specimens: *a*, *d* — *XY* and *XZ* planes with strategic rotation angle of 0°; *b*, *e* — *XY* and *XZ* planes with strategic rotation angle of 67.5°; *c*, *f* — *XY* and *XZ* planes with strategic rotation angle of 90° [34]

bution of the solute, can also lead to deterioration of corrosion resistance [31, 32]. Thus, homogeneous microstructure and thicker surface film which may form after recrystallization heat treatment, can effectively improve the corrosion resistance of SLM specimens.

Laser scanning strategy and directions of building the grains and their bonds also have a strong influence on the microstructure and mechanical properties of final parts manufactured by SLM. Such a search for optimal scanning strategy (Figure 3) can be also used in SLM manufacture of parts with higher mechanical properties [33]. Moreover, at application of scanning strategy with rotation in each next pass, a porous structure was found on the upper surface of the manufactured part, and a columnar (dendritic) structure was present on its side surface. Their formation directly affects the mechanical properties of the part.

In work [34] use of various scanning techniques was studied during SLM of test specimens made from 316L steel, in order to determine the optimum scanning strategy at application of this material. Microstructure analysis using EBSD and SEM-microscopy (Figure 4) shows that the scanning strategy influences the continuity of grain growth through the adjacent layers and grain growth inside the melt track. Electrochemical testing pointed to an obvious difference in the corrosion resistance normal and in parallel to the scanning direction and with different techniques. Point corrosion is the main form of corrosion in 316L stainless steel, and it arises predominantly on the melt pool boundaries.

There is a large number of experimental research on the microstructures and mechanical properties of specimens produced from Inconel 718 by SLM. However, there are just a few studies of the influence of laser radiation parameters on the microstructure and mechanical properties of such parts [35]. Strossner et al. [36] proved that the microstructures of SLM specimens of Inconel 718 were very fine and oriented along the building direction. Yi et al. [37] found formation of a bright area in the form of a crescent on the lower edge of the melt pool of parts produced from Inconel 718 alloy. This area consisted of thinner

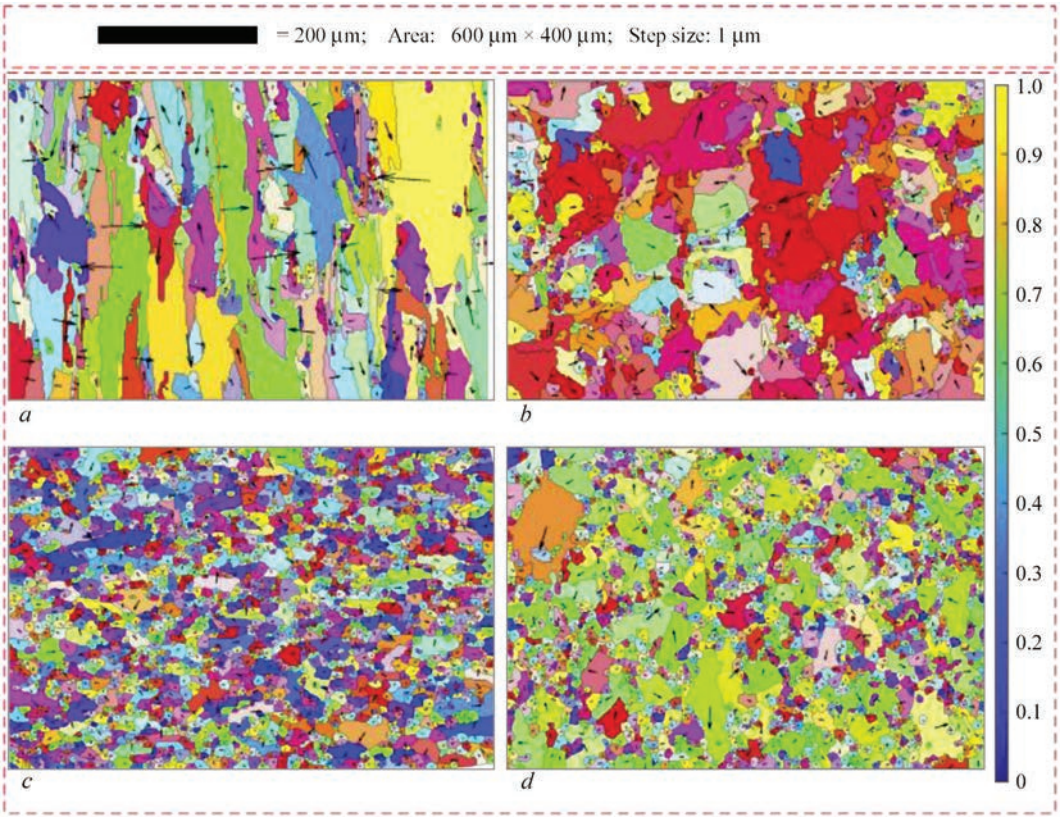

Figure 5. Grain microstructure in deformed (*b*, *d*) and undeformed (*a*, *c*) specimens of Inconel 718 alloy, produced by forging (*c*, *d*) and selective laser melting (*a*, *b*) technologies [42]

columnar dendrites of the same orientation as on the melt pool surface. Wan et al. [38] studied the influence of scanning strategy on the microstructure and texture of SLM Inconel 718, establishing a number of dependencies, pointing to a direct influence of scanning strategy on mechanical properties of the produced parts. Popovich et al. [39] proved the ability of additive manufacturing to produce individual microstructures with specified mechanical properties. In addition to these studies, many researchers focused on investigation of the influence of further treatment to achieve a comprehensive improvement of the part mechanical characteristics. Amato et al. [40] noted that the microstructure of a portion of an SLM part demonstrates columnar grains, irrespective of whether it was parallel or normal to the building direction, and studied the microhardness (Vickers) of rolled material produced by HIP and of annealed material.

Investigations of the structure of high-strength Inconel 718 alloy produced by SLM, was described in [41]. The influence of density of laser input energy (E, J/mm^3) on the density, phase composition, microstructure, homogeneity and mechanical properties of SLM specimens was analyzed in detail. Proceeding from experimental data of this study, it was noted that the surface morphology and density of SLM specimens were controlled by the power density value. The authors believe that it is possible to control also the dendrite structure in the same way by controlling the power density value, as increase of power density reduced the thickness of dendrites in experimental specimens.

Results of work [42] (Figure 5) showed that SLM Inconel 718 alloy demonstrates a slight coarsening of grain boundaries in the metal structure, as well as weakening of manifestation of its texture that differs from the phenomena of grain boundary coarsening and slight enhancement of the texture of cast Inconel 718 alloy. The SLM specimen has lower residual compressive stresses, compared to the wrought alloy, while the values of tool wear, surface roughness and microhardness are higher then those in a micromilled part.

Most of the current works on corrosion resistance report that SLM parts from 316L steel demonstrate better corrosion resistance, compared to parts from 316L steel with the structure produced at material forging. The results, however, cam be relatively fragmented [43-45]. In work [46] the corrosion behaviour of steels 316L(WS — forged structure), 316L(SLM) and 316L(SLM-1050 — annealing at 1050 °C for 15 min and quenching in water) was analyzed, allowing for their microstructure, residual stresses and physico-chemical properties of passively formed films. This work is a rather profound study of corrosion behaviour of these materials, taking into account the alloying additives and impurities (Figure 6).

CRITICISM OF WORKS

The works, in which the influence of energy component of SLM processes on its results was studied,

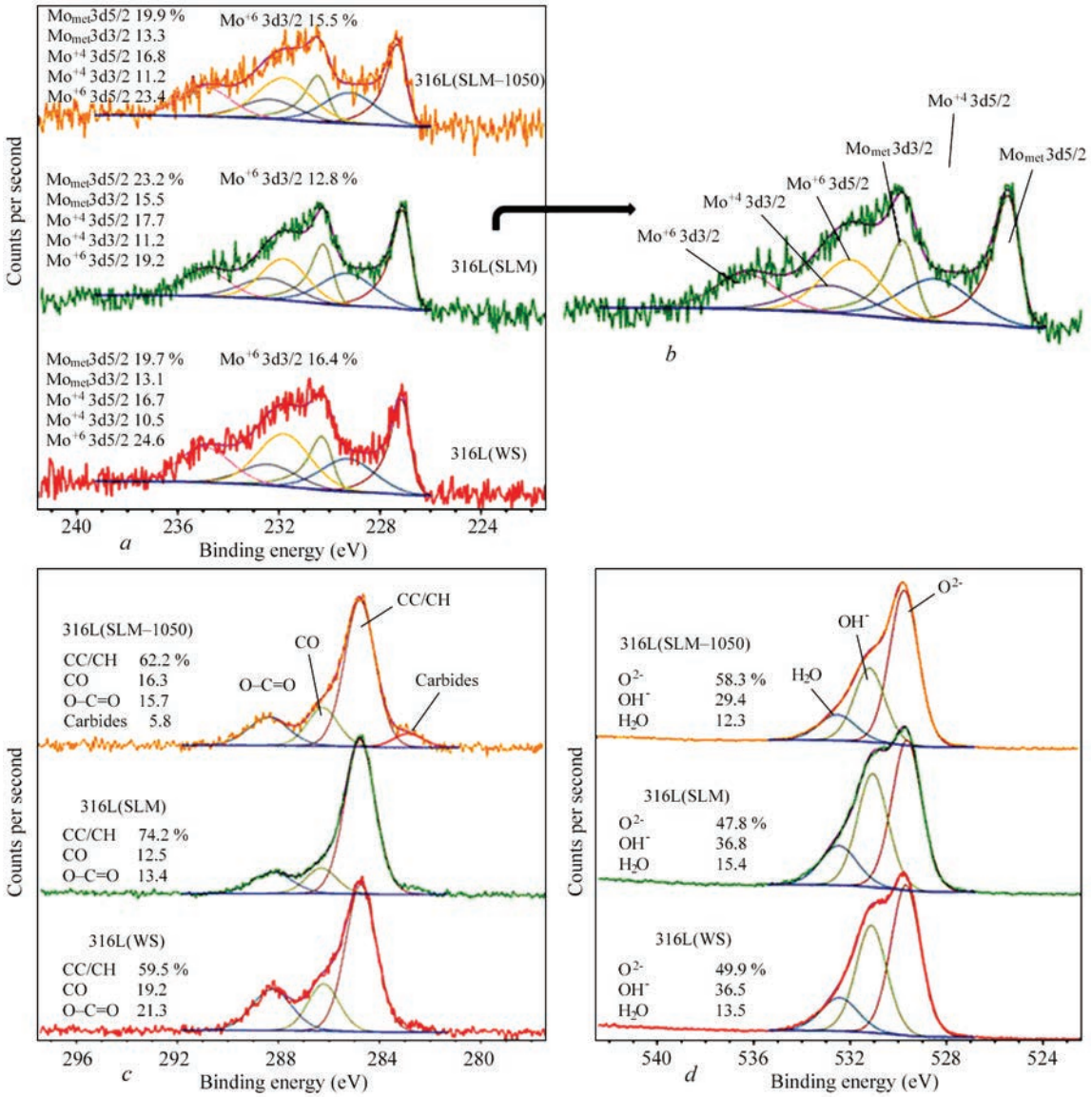

Figure 6. XPS-spectroscopy results of varieties of 316L steel after surface treatment: *a*, *b* — molybdenum levels; *c* — carbide levels; *d* — oxide levels [46]

considered individual cases of SLM process analysis for performance of certain tasks. Attempts to create a general model to study the influence of variables of SLM process energy component were noted. So, results of modeling the structure of upper layers of the processed surface in work [16] were compared with those of the experiment. Despite the fact that these results were in good agreement, this model did not become widely accepted, because of a lack of assessment of its capabilities under different conditions. Here, this model was not taken to such a condition that would allow its application for general computation of SLM processes. This, in its turn, leads to cardinally different works being the base for studying similar processes in work [12].

The works in which the possibilities of SLM process optimization by controlling the amount of laser radiation defocusing were analyzed, provided a rather profound study of both their advantages and disadvantages, related to such an application of SLM process. However, because of a relatively small number of works considering these possibilities, the general assessments of the effectiveness of this work are empirical, and not been brought to a holistic theory confirmed by general regularities.

The considered studies of the methods of improving the adaptability-to-manufacture of SLM specimen microstructure, focused on two directions, namely control of the process of microstructure formation by finding the optimum path of scanning and powder feed, as well as removal of undesirable admixtures in the structure of SLM specimen. The works, focusing on finding a more effective path of scanning and powder feed, demonstrated rather big problems with this component, as the movement pattern of the head of laser technological complex (LTC) has an important role in this process, both as to the microstructure and further characteristics of the part. So, a large number of parts studied in [36]

were found to have point corrosion and pitting, which adversely affect the part performance. Although other works indicate that in certain cases the SLM parts demonstrate better corrosion resistance than do parts with a forged metal structure, the question of general resistance of SLM parts remains quite relevant.

Analysis of investigations of SLM-manufacturing of parts from a number of widely accepted metals revealed that there are numerous experimental studies, which analyze the final microstructure and mechanical properties of SLM parts. On the other hand, in the opinion of the author, there are not enough studies focused on determination of the influence of laser radiation parameters on the final microstructure and mechanical properties of the parts. Certain regularity was noted: control over SLM process is considered in the form of special processing modes, individual for each technical assignment. However, the obtained research data is insufficient to formulate the regularities of the influence of individual laser radiation characteristics on the microstructure in SLM parts.

CONCLUSIONS

PROBLEMS OF DEEPENING THE KNOWLEDGE ON SLM PROCESS

The main problem of further optimization of SLM process is absence of general regularities of the influence of SLM parameters on structure formation, geometry and level of mechanical characteristics of the produced specimens, which could be taken into account at development of the respective procedure of controlling the technological process parameters. It would allow increasing the quality and level of service and functional properties of the produced specimens and developing technological recommendations on product manufacturing for different industries, allowing for the respective service requirements. A literature review of the state of research into the processes of SLM manufacturing was conducted to verify this thesis.

Therefore, it is considered rational to emphasize the need to create a systematized comprehensive approach to optimization of SLM process. Obtained using this approach regularities of the influence of laser radiation characteristics on the microstructure and mechanical properties of SLM parts, can be used to develop a complex of technological measures for SLM manufacturing processes. Introduction of this complex of SLM technological measures, in the opinion of the author, will allow solving a large variety of tasks, posed by different industries at manufacturing a wide range of products.

REFERENCES

1. Sun, Z., Tan, X., Tor, S., Chua, C. (2018) Simultaneously enhanced strength and ductility for 3D-printed stainless steel 316L by selective laser melting. *NPG Asia Materials*, 10(**4**), 127–136.
2. Wang, Y., Voisin, T., McKeown, J. et al.. (2017) Additively manufactured hierarchical stainless steels with high strength and ductility. *Nature Materials*, 17(**1**), 63–71.
3. Yang, W., Tarng, Y. (1998) Design optimization of cutting parameters for turning operations based on the Taguchi method. *J. of Materials Processing Technology*, 84(**1–3**), 122–129.
4. Mukherjee, T., Manvatkar, V., De, A., DebRoy, T. (2017) Dimensionless numbers in additive manufacturing. *J. of Applied Physics*, 121(**6**), id.064904.
5. Ion, J., Shercliff, H., Ashby, M. (1992) Diagrams for laser materials processing. *Acta Metallurgica et Materialia*, 40(**7**), 1539–1551.
6. Thomas, M., Baxter, G., Todd, I. (2016) Normalised model-based processing diagrams for additive layer manufacture of engineering alloys. *Acta Materialia*, **108**, 26–35.
7. Jiang, H., Li, Z., Feng, T. et al.. (2019) Factor analysis of selective laser melting process parameters with normalised quantities and Taguchi method. *Optics & Amp.; Laser Technology*, **119**, id.105592.
8. Darvish, K., Chen, Z., Pasang, T. (2016) Reducing lack of fusion during selective laser melting of CoCrMo alloy: Effect of laser power on geometrical features of tracks. *Materials & Amp; Design*, **112**, 357–366.
9. Li, Z., Voisin, T., McKeown, J. et al.. (2019) Tensile properties, strain rate sensitivity, and activation volume of additively manufactured 316L stainless steels. *Inter. J. of Plasticity*, **120**, 395–410.
10. Hou, H., Simsek, E., Ma, T. et al.. (2019) Fatigue-resistant high-performance elastocaloric materials made by additive manufacturing. *Science*, 366(**6469**), 1116–1121.
11. Ma, M., Wang, Z., Zeng, X. (2017) A comparison on metallurgical behaviors of 316L stainless steel by selective laser melting and laser cladding deposition. *Materials Sci. and Eng.: A*, **685**, 265–273.
12. Jiang, H., Li, Z., Feng, T. et al.. (2020) Effect of process parameters on defects, melt pool shape, microstructure, and tensile behavior of 316L stainless steel produced by selective laser melting. *Acta Metallurgica Sinica*, 34(**4**), 495–510.
13. Kurzynowski, T., Gruber, K., Stopyra, W. et al.. (2018) Correlation between process parameters, microstructure and properties of 316 L stainless steel processed by selective laser melting. *Materials Sci. and Eng.: A*, **718**, 64–73.
14. Martin, A., Calta, N., Khairallah, S. et al.. (2019) Dynamics of pore formation during laser powder bed fusion additive manufacturing. *Nature Communications*, 10(**1**). DOI: https://doi.org/10.1038/s41467-019-10009-2
15. Tang, C., Tan, J., Wong, C. (2018) A numerical investigation on the physical mechanisms of single-track defects in selective laser melting. *Inter. J. of Heat and Mass Transfer*, **126**, 957–968.
16. Zheng, M., Wei, L., Chen, J. et al.. (2021) On the role of energy input in the surface morphology and microstructure during selective laser melting of Inconel 718 alloy. *J. of Materials Research and Technology*, **11**, 392–403.
17. Zheng, M., Wei, L., Chen, J. et al.. (2019) A novel method for the molten pool and porosity formation modeling in selective laser melting. *Inter. J. of Heat and Mass Transfer*, **140**, 1091–1105.
18. Zheng, M., Wei, L., Chen, J. et al.. (2019) Surface morphology evolution during pulsed selective laser melting: Numerical and experimental investigations. *Applied Surface Sci.*, **496**, id.143649.
19. Deng, C., Kang, J., Feng, T. et al.. (2018) Study on the selective laser melting of CuSn10 powder. *Materials*, 11(**4**), 614.
20. Kempen, K. (2015) *Expanding the materials palette for selective laser melting of metals (Ph.D.)*. KU Leuven University, Belgium.

21. Wang, L., Wei, Q., Shi, Y. et al.. (2011) Experimental investigation into the single-track of selective laser melting of IN625. *Advanced Materials Research*, **233–235**, 2844–2848.
22. Yadroitsev, I., Yadroitsava, I., Bertrand, P., Smurov, I. (2012) Factor analysis of selective laser melting process parameters and geometrical characteristics of synthesized single tracks. *Rapid Prototyping J.*, 18(**3**), 201–208.
23. Promoppatum, P., Yao, S., Pistorius, P., Rollett, A. (2017) A Comprehensive comparison of the analytical and numerical prediction of the thermal history and solidification microstructure of Inconel 718 products made by laser powder-bed fusion. *Engineering*, 3(**5**), 685–694.
24. Brandt, M. (2016) *Laser additive manufacturing: Materials, design, technologies, and applications*. Duxford: Woodhead Publishing, 259–279.
25. Metelkova, J., Kinds, Y., Kempen, K. et al.. (2018) On the influence of laser defocusing in selective laser melting of 316L. *Additive Manufacturing*, **23**, 161–169.
26. Paraschiv, A., Matache, G., Condruz, M. et al.. (2021) The influence of laser defocusing in selective laser melted IN 625. *Materials*, 14(**13**), 34–47.
27. Zhou, C., Hu, S., Shi, Q. et al.. (2020) Improvement of corrosion resistance of SS316L manufactured by selective laser melting through subcritical annealing. *Corrosion Sci.*, **164**, id.108353.
28. McLouth, T., Bean, G., Witkin, D. et al.. (2018) The effect of laser focus shift on microstructural variation of Inconel 718 produced by selective laser melting. *Materials & Design.*, **149**, 205–213.
29. Laleh, M., Hughes, A., Xu, W. et al.. (2020) Unanticipated drastic decline in pitting corrosion resistance of additively manufactured 316L stainless steel after high-temperature post-processing. *Corrosion Sci.*, **165**, id.108412.
30. Duan, Z., Man, C., Dong, C. et al.. (2020) Pitting behavior of SLM 316L stainless steel exposed to chloride environments with different aggressiveness: Pitting mechanism induced by gas pores. *Corrosion Sci.*, 167, id.108520.
31. Kong, D., Ni, X., Dong, C. et al.. (2018) Heat treatment effect on the microstructure and corrosion behavior of 316L stainless steel fabricated by selective laser melting for proton exchange membrane fuel cells. *Electrochimica Acta*, **276**, 293–303.
32. Trelewicz, J., Halada, G., Donaldson, O., Manogharan, G. (2016) Microstructure and corrosion resistance of laser additively manufactured 316L stainless steel. *JOM*, 68(**3**), 850–859.
33. AlMangour, B., Grzesiak, D., Yang, J. (2017) Scanning strategies for texture and anisotropy tailoring during selective laser melting of TiC/316L stainless steel nanocomposites. *J. of Alloys and Compounds*, **728**, 424–435.
34. Zhao, C., Bai, Y., Zhang, Y. et al.. (2021) Influence of scanning strategy and building direction on microstructure and corrosion behaviour of selective laser melted 316L stainless steel. *Materials & Amp; Design*, **209**, id.109999.
35. Wang, X., Kang, J., Wang, T. et al.. (2019) Effect of layer-wise varying parameters on the microstructure and soundness of selective laser melted Inconel 718 Alloy. *Materials*, 12(**13**), id.2165.
36. Strößner, J., Terock, M., Glatzel, U. (2015) Mechanical and microstructural investigation of nickel-based superalloy IN718 manufactured by selective laser melting (SLM). *Advanced Engineering Materials*, 17(**8**), 1099–1105.
37. Yi, J., Kang, J., Wang, T. et al.. (2021) Microstructure and mechanical behavior of bright crescent areas in Inconel 718 sample fabricated by selective laser melting. *Materials & Amp; Design*, **197**, id.109259.
38. Wan, H., Zhou, Z., Li, C. et al.. (2018) Effect of scanning strategy on grain structure and crystallographic texture of Inconel 718 processed by selective laser melting. *J. of Materials Sci. & Amp; Technology*, 34(**10**), 1799–1804.
39. Popovich, V., Borisov, E., Popovich, A. et al.. (2017) Functionally graded Inconel 718 processed by additive manufacturing: Crystallographic texture, anisotropy of microstructure and mechanical properties. *Materials & Amp; Design*, **114**, 441–449.
40. Amato, K., Gaytan, S., Murr, L. et al. (2012) Microstructures and mechanical behavior of Inconel 718 fabricated by selective laser melting. *Acta Materialia*, 60(**5**), 2229–2239.
41. Liu, X., Wang, K., Hu, P. (2021) Formability, microstructure and properties of Inconel 718 superalloy fabricated by selective laser melting additive manufacture technology. *Materials*, 14(**4**), 991.
42. Ji, H., Gupta, M., Song, Q. et al.. (2021) Microstructure and machinability evaluation in micro milling of selective laser melted Inconel 718 alloy. *J. of Materials Research and Technology*, **14**, 348–362.
43. Sander, G., Thomas, S., Cruz, V. et al.. (2017) On the corrosion and metastable pitting characteristics of 316L stainless steel produced by selective laser melting. *J. of The Electrochemical Society*, 164(**6**), 250–257.
44. Chao, Q., Cruz, V., Thomas, S. et al.. (2017) On the enhanced corrosion resistance of a selective laser melted austenitic stainless steel. *Scripta Materialia*, **141**, 94–98.
45. Zhang, Y., Liu, F., Chen, J., Yuan, Y. (2017) Effects of surface quality on corrosion resistance of 316L stainless steel parts manufactured via SLM. *J. of Laser Applications*, 29(**2**), 022306.
46. Vignal, V., Voltz, C., Thiébaut, S. et al.. (2021) Pitting corrosion of type 316L stainless steel elaborated by the selective laser melting method: Influence of microstructure. *J. of Materials Eng. and Performance*, 30(**7**), 5050–5058.

ORCID
M.V. Sokolovskyi: 0000-0003-3243-5060

CORRESPONDING AUTHOR
M.V. Sokolovskyi
E.O. Paton Electric Welding Institute of the NASU
11 Kazymyr Malevych Str., 03150, Kyiv, Ukraine.
E-mail: m_sokolovskyi@paton.kiev.ua

SUGGESTED CITATION
M.V. Sokolovskyi (2022) Problems and prospects of studying the processes of selective laser melting of materials for aerospace engineering (Review). *The Paton Welding J.*, **11**, 8–16.

JOURNAL HOME PAGE
https://patonpublishinghouse.com/eng/journals/tpwj

Received: 30.06.2022
Accepted: 29.12.2022

DOI: https://doi.org/10.37434/tpwj2022.11.03

JOINING BUILDING REBARS USING COUPLINGS COMPRESSED BY EXPLOSION

A.G. Bryzgalin, P.S. Shlyonskyi, S.D. Ventsev, E.D. Pekar

E.O. Paton Electric Welding Institute of the NASU
11 Kazymyr Malevych Str., 03150, Kyiv, Ukraine

ABSTRACT

Joining building rebars is a labour-consuming critical process. Arc welding processes are of little use in the cases of application of heat-strengthened building rebars, or such which have a protective layer. It is shown that use of steel couplings, compressed by explosion, allows producing strong and reliable joints of building rebars for various applications. Coupling parameters are calculated under the condition of equal strength with rebars steel. Rupture testing revealed a higher strength of the coupling joint, compared to the strength of rebars beyond which a rupture took place. Cyclic fatigue life testing showed that fatigue resistance of coupling joints is higher than that required by normative documentation. There is experience of application of explosives in large construction sites and in operating industrial facilities.

KEYWORDS: building rebars, rebar joining, coupling, fatigue resistance, strength, explosion compression

INTRODUCTION

The methods for joining rebars in the construction of reinforced concrete objects available for today [1, 2] have a number of disadvantages. Electric arc, pool and resistance welding require the use of special equipment and powerful power sources, which complicates the works in site conditions; heating to melting point at the joining place leads to the softening of the base metal of heat-resistant building rebars (HBR); burnout of elements of a corrosion-resistant protective layer (if such deposited on rebars). Winding of rebars with steel wire leads to an axial displacement of joined rebar elements, it does not always provide equal strength of joint and base metal either, is a very labour-consuming process, especially when joining rebars of a large size. Joint rebars with the use of couplings, which are compressed by hydraulic presses, requires the use of expensive imported equipment and is a labour-consuming process with a low efficiency.

The development of high-efficient, economic and ergonomic methods for joining HBR, providing the strength properties of joints at the level of base metal is an urgent task for today.

One of such methods can be joining rebars by couplings compressed by explosion. The advantages of the explosive method are the lack of softening of the base metal and the need in using special equipment, independence from power supply sources and high efficiency.

Under the action of explosion pressure, the coupling is plastically compressed and forms a mechanical joint with the rebars by gearing the coupling metal with transverse projections of the rebars. The joint strength during tensile loading will be determined by the strength of the coupling metal and the strength of transverse projections of the rebars operating on crumbling. The calculation by these parameters, taking into account providing the equal strength of the joint and rebar metal, will ensure determination of the thickness and length of the coupling. The shear calculation of the transverse projections gives a shorter length of the coupling than the crumbling calculation. All the necessary data for the calculation is given in DSTU 3760 [3].

Schematic diagram of rebar joint by the coupling compressed by explosion is shown in Figure 1. The appearance of joining before and after the explosion is shown in Figure 2.

As an explosive substance, the detonating cord of grade DShE-12 was used, which had a bulk weight of 12 g/m, an outer diameter of 6 mm and was manufactured in industrial way [4].

As was noted above, the greatest difficulties occur when joining rebar elements of a large diameter. Therefore, to evaluate the capabilities of the explosion compression method, in research works, rebars of grade A600 DSTU 3760–98 were used [3] with a rated diameter of the rod of 25 mm, σ_y = 600 MPa, a cross-section area of the main rod of 491 mm^2, the maximum diameter of 28 mm, a cross-projection area near the base of 96

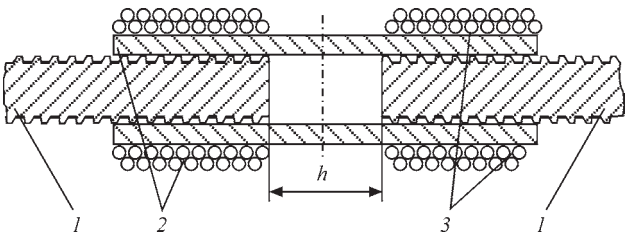

Figure 1. Schematic diagram of joining rebars by the coupling compressed by explosion: *1* — ends of joined rebars; *2* — coupling; *3* — charge from a detonating cord, wound on the coupling; *h* — adjustable gap between rebar ends

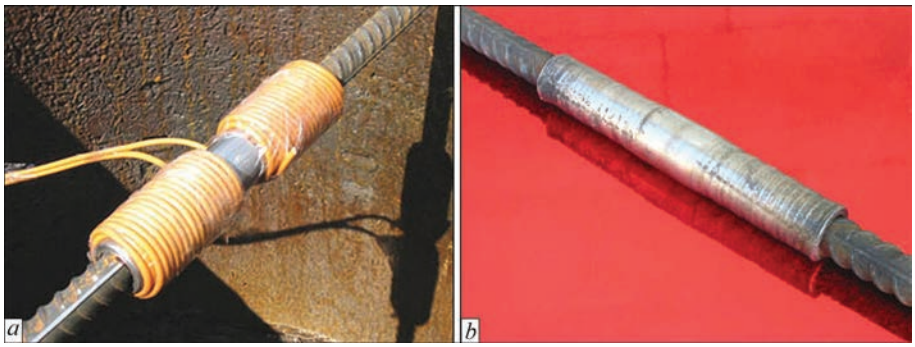

Figure 2. Coupling joint of rebars, prepared before compression explosion (*a*) and coupling joint after explosion (*b*)

mm^2 and an average input number of cross projections (taking into account manufacture defects of rebars in the form of lack of projections) of 114 pcs/m.

Couplings (tubes) were manufactured of steel 06G2B, σ_y = 440 MPa, outer diameter is 44 mm, wall thickness is 6 mm, length is 235 and 255 mm. The cross-section area of the coupling was selected in such a way that its tensile strength was slightly higher than the strength of rebars, i.e., the force at which the yield strength of 315 and 300 kN is respectively reached.

Three specimens of rebar joints were manufactured, whose couplings were compressed by charges consisting of one, two and three layers of DShE-12.

One layer was not sufficient for a reliable compression of the coupling. Two and three layers formed a dense joint of the coupling with rebars.

Additionally, two samples were manufactured with the coupling compression by two layers of the detonating cord with a gap between the rebar ends of 20 and 40 mm, respectively, the length of the coupling was 235 and 255 mm, the lengths of the compressed areas were maintained constant.

During tensile tests of the samples, the fracture occurred on the base metal of the rebars (Figure 3).

The stressed state of the coupling metal in the butt zone is largely determined by the gap between the rebar ends. In the samples with a zero gap during tension, which creates axial stresses close to the yield strength, in the cross-section of the coupling, passing through the butt of the rebar ends, a volumetric stressed state will be created. In this case, the rupture force should increase, and the fracture of the coupling wall should have a brittle nature. As the gap increases, the main stresses in the circumferential direction and across the thickness will decrease, the stressed state will approach the linear state, the overall rupture strength of the coupling metal should reduce and the nature of the fracture will be more tough.

To check the impact of the gap on the strength of joint and the nature of fracture, a series of experiments on the rebars samples of grade A400C of steel 25G2C with d_r = 28 mm was carried out. The coupling metal is steel 20. The inner diameter of the couplings is 32 mm, the calculated outer diameter of the couplings is 43.5 mm. For the purpose of fracture of the joint over the coupling metal, the outer diameter is taken equal to 43 mm, the thickness of the coupling wall was 5.5 mm.

The compression of the couplings was carried out using DShE-12, wound on the couplings in two layers. The samples with a gap between the rebar ends inside the coupling were only compressed on the side of the coupling that was above the rebars. The test results are given in Table 1.

Figure 4 shows the appearance of the cross-section of the couplings after the fracture of the samples with a different gap. It should be noted that the fracture of the samples occurred at stresses close to the tensile strength of the rebars.

Additionally, two series of strength tests (each for 2 samples) were conducted on the samples made

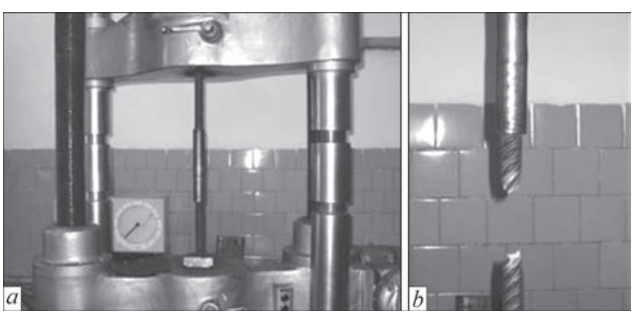

Figure 3. Rupture tests of rebar joints: *a* — sample before test in a rupture machine; *b* — sample after tests

Table 1. Test results of rebar joints with different size of gap between its ends

Number of joint	Size of gap, mm	Average rupture force, kg	Place of gap
1	0	32000	Over the coupling
2	0	36500	Over the base metal
3	0	35500	–»–
4	20	31000	Over the coupling
5	20	27750	–»–
6	20	29000	–»–
7	40	31500	–»–
8	40	33000	–»–
9	40	32750	–»–

Figure 4. Nature of fracture of samples during tensile tests: *a* — sample with a zero gap; *b* — sample with a gap of 20 mm; *c* — sample with a gap of 40 mm

Table 2. Results of fatigue tests of coupling joints

Sample number	Load, tf		Stresses, MPa		Number of cycles
	max	min	max	min	*N*
1	25.1	10.1	306.16	122.50	287840
2	25.0	10.0	304.94	122.0	323390
3	19.0	7.6	231.76	97.70	837680
4	28.0	11.2	341.50	136.60	289150
5	22.0	8.8	268.35	107.30	529030
6	13.1	5.3	160.0	64.0	2290430 not fractured

from the rebars of grade A500C with d_r = 32 mm. The couplings were made of a low carbon steel with σ_y = = 270 MPa and with σ_y = 400 MPa, the wall thickness was 10.5 and 8 mm, respectively. In all cases, the fracture occurred on the base metal of the rebars.

Bridges and similar reinforced concrete structures undergo variable loads from transport moving across them.

In DBN B.2.3-14 [5], the formulas for calculation of the fatigue strength of the rebars during tensile tests are shown. DSTU 3760 [3] regulates carrying out cyclic tests in such a way: "Reinforced rolled metal of grades A400, A500, A600, A600C, A600K, A800, A800K and A1000 should withstand 2 mln load cycles at a maximum stress, which amounts to 6 0 % of the normalized tensile yield strength without the fracture. In this case, the range of stresses should amount to 180 N/mm ^{2}".

The fatigue tests were performed in the laboratory conditions of the PWI on a soft mode of axial harmonic tension in a multicyclic area of fatigue life with a frequency of 5 Hz and the cycle asymmetry coefficient ρ = 0.4. The studies were performed on the rebars of grade A500 (A IV) with a diameter of 32 mm of a total length of 800 mm, σ_y = 500 MPa, σ_{max} = = 300 MPa, σ_{min} = 120 MPa.

The criterion for completion of the tests was a complete fracture of the sample. The samples were fractured inside the coupling at a distance of 10–35 mm from its edge. The results of the studies are presented in Table 2, as well as in a graphic form in Figure 5.

The results of the experimental studies allow determining the fatigue resistance of the coupling joints of the rebars of grade A500C of 32 mm diameter at an asymmetric cycle of axial tension ρ = 0.4 in the whole multicyclic region of an alternating load. The fatigue strength of such joints on the base of $2 \cdot 10^6$ cycles is 165 MPa.

In DBN B.2.3-14 [5], the value of the coefficient characterizing the serviceability of rebar joint of grade A500 (A IV) at cyclic tests with an asymmetry coefficient 0.4, is taken equal to 0.75. The value of the coefficient obtained experimentally is equal to 0.87, which is higher than the normative and fully satisfies the requirements of DBN B.2.3-14. Such joints neither in strength nor in fatigue resistance are not inferior to the joints, produced by other methods widely used in industry.

It should be noted that for explosion compression of the couplings, the charges of a low power are used, simultaneously up to 10 charges can be initiated, the safe

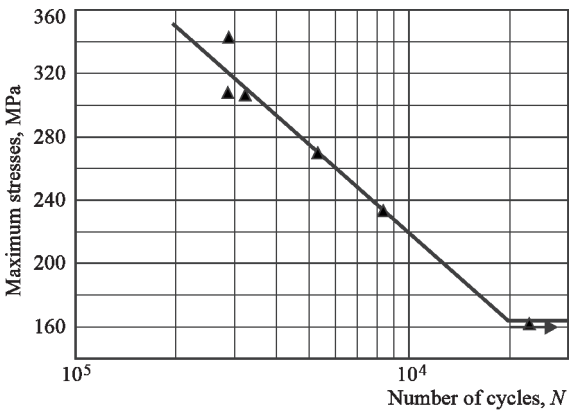

Figure 5. Diagram of fatigue resistance of coupling joints

distance from explosion to the location of a human behind the action of a shock wave is 30 m [6], during a working shift, a team of 7 persons can produce 50–100 butts. The experience of using explosion at operating enterprises [7] indicates the possibility of industrial use of this method on large construction sites.

CONCLUSIONS

1. The use of steel couplings compressed by explosion allows producing joining of HBR, which meet the building standards of Ukraine, which in terms of strength and cyclic fatigue life are not inferior to those produced by traditional methods.

2. Using the method of coupling explosion compression is possible at operating enterprises and large construction sites.

3. The method proposed in this work has a higher efficiency than traditional methods.

REFERENCES

1. DSTU B V.2.6-168:2011: *Welded rebars and embedded products, welded joints of rebars and embedded products of concrete structures. General technical conditions* [in Ukrainian].
2. DSTU B V.2.6-169:2011: *Welded joints of rebars and embedded products of concrete structures. Types, structures and dimensions* [in Ukrainian].
3. *DSTU 3760L:2019: Reinforcing bars for concrete structures. General technical conditions* [in Ukrainian].
4. Petushkov, V.G. (2005) *Application of explosion in welding technology*. Kyiv, Naukova Dumka [in Russian].
5. DBN V.2.3-14:2006: *Bridges and pipes. Design rules* [in Ukrainian].
6. (2013) *Safety rules when handling explosive materials for industrial purposes*. Kyiv, Okhorona Pratsi [in Ukrainian].
7. Lobanov, L.M., Bryzgalin, A.G., Dobrushin, L.D. et. al. (2009) Widening of technological capabilities of explosion treatment for reducing residual stresses in welded joints on up to 5000 m^3 decomposers. *The Paton Welding J.*, **11**, 46–48.

ORCID

A.G. Bryzgalin: 0000-0001-5886-3069,
P.S. Shlyonskyi: 0000-0002-3566-1752,
E.D. Pekar: 0000-0001-5025-4445

CONFLICT OF INTEREST

The Authors declare no conflict of interest

CORRESPONDING AUTHOR

A.G. Bryzgalin
E.O. Paton Electric Welding Institute of the NASU
11 Kazymyr Malevych Str., 03150, Kyiv, Ukraine.
E-mail: andreybag60@ukr.net

SUGGESTED CITATION

A.G. Bryzgalin, P.S. Shlyonskyi, S.D. Ventsev, E.D. Pekar (2022) Joining building rebars using couplings compressed by explosion. *The Paton Welding J.*, **11**, 17–20.

JOURNAL HOME PAGE

https://patonpublishinghouse.com/eng/journals/tpwj

Received: 04.08.2022
Accepted: 29.12.2022

DOI: https://doi.org/10.37434/tpwj2022.11.04

ION-PLASMA NITRIDING OF INNER CYLINDRICAL SURFACES OF PRODUCTS

I.V. Smirnov[1], **A.V. Chornyi**[1], **V.V. Lysak**[1], **M.O. Sysoyev**[2], **G.P. Kysla**[2]

[1]E.O. Paton Training-Research Institute of Materials Science and Welding
of National Technical University of Ukraine «Igor Sikorsky Kyiv Polytechnic Institute»
37 Peremohy Prosp., 03056, Kyiv, Ukraine
[2]PJSC «PlasmaTek»
18 Maksymovych Str., 21036, Vinnytsia, Ukraine

ABSTRACT

Technological modes of pulsed ion-plasma nitriding of inner cylindrical surfaces with application of a hollow perforated anode were developed. It results in formation of diffusion coatings, consisting of areas of different chemical and phase composition. Maximum concentration of nitrogen is observed in the areas opposite holes in the anode, which are made at a certain distance at a certain angle. Accordingly, these same areas contain a hard phase from iron nitride, discretely arranged in a soft matrix of α-iron. Testing under the conditions of dry friction of metal against metal showed that the wear resistance of specimens, taken from different areas of the nitrided specimens, is 3–5 times higher than in the initial non-nitrided specimen that is indicative of a high wear resistance and good prospects for their further investigation.

KEYWORDS: ion-plasma nitriding, discrete-matrix coatings, technological modes, wear resistance, inner cylindrical surfaces

INTRODUCTION

Compared to other nitriding methods, ion-plasma nitriding has a number of technical and economic advantages such, as minimal energy- and labour-intensiveness of the process, high values of contact endurance and fatigue strength of the hardened surface. More over, it allows removing chemical contaminants, which are released into the environment at application of the traditional treatments: chemical, electrochemical, salt and other.

Alongside the environmental friendliness and cost-effectiveness of the process, ion-plasma nitriding allows producing diffusion layers of the specified composition and structure, both with the nitride zone on the surface, and without it. In the first case, high corrosion and wear resistance of friction surfaces is ensured, but crack resistance decreases, and in the second case the alternating loading resistance under the conditions of high pressure and temperature is increased.

Ion-plasma nitriding also allows solving the problem of strengthening especially deep holes, the length of which is greater than their diameter tens of times and that is a rather complex task practically for all the surface engineering methods and requires further studies.

Numerous studies, by both local and foreign researchers are devoted to nitriding technologies, including combined saturation of the steel surface by nitrogen and carbon (carbonitriding) [1–4].

Work [5] gives the results of nitriding by high-density plasma with hollow tubular cathode of small-sized specimens from martensitic stainless steel AISI 420-J2 at the temperature of 673 K. It led to formation of a nitrided surface layer up to 80 μm thick and 31 at.% nitrogen concentration on its surface. In work [6] studies were also performed on nitriding in the hollow cathode mode of products of microtube type from steels AISI 304 and AISI 316 of 5.5 to 30.0 mm length with inner diameter from 0.58 to 16.9 mm and outer diameter from 0.88 to 21.5 mm. A mixture of nitrogen and hydrogen gases was passed through a hole, the internal surface hardness rising to more than 800 *HV*.

Authors of work [7] conducted ion nitriding of tubular specimens from 32CrMoV12-10 steel with hole diameter of 6 and 8 mm and 500 mm length at the temperature of 500 °C for 6 h with a mixture of hydrogen and nitrogen gases. The length of the nitrided layer was 234 mm at hole diameter of 8 mm and 138 mm at hole diameter of 6 mm. Thus, the length of the nitrided layer decreased with decrease of the hole diameter. The nitrided surface consisted of a composite layer on the surface and diffusion transition zone. The specimen surface hardness increased by 100 %. The authors of [8] applied gas nitriding for treatment of bores of small arms of the diameter from 5.56 to 12.5 mm from 38HMJ steel in NH_3 ammonia environment. It resulted in formation of a hardened layer approximately 220 μm thick with subsurface microhardness of 900 *HV*. Here a white layer of iron nitrides with ε + γ′-phase structure of 12–15 μm thickness formed on the surface. It has a high hardness and corrosion resistance, but low crack resistance.

Crack and wear resistance of nitrided layers can be significantly improved by forming discrete structures, which are ever wider applied in different mechanical engineering sectors [9].

Mechanical properties						Heat treatment			
						Quenching		Tempering	
σ_y, MPa	σ_t, MPa	δ, %	ψ, %	a_h, J/cm^2	*HB*	Temperature, °C	Cooling medium	Temperature, °C	Cooling medium
961	1118	21	64	107	195	850–40	Oil	620–60	Water

The principle of a discrete structure consists in replacement of the continuous structure of the surface layer by a discrete-matrix one that greatly improves the limit state of the surface (contact loads, critical deformations of the base, crack resistance, fatigue life), compared to a continuous coating of the same thickness, composition and hardness.

Considering the insufficient research into the phenomena taking place on the discrete structure surface, and absence of its design methods, many studies were directed at optimal design of a discrete structure, allowing for residual stresses [10].

Dimensions and configuration of individual areas are calculated, proceeding from the conditions of minimizing the level of stress-strain state during mechanical and temperature impact, and they are determined by analytical and numerical methods.

The discrete-matrix structure is formed by ion-plasma method using diverse screens, patterns, masks, also in the form of metal grid [11, 12]. The grid geometrical parameters are selected, proceeding from calculation of a discrete area dimensions and continuity with provision of a minimal level of residual stresses in the surface layer. The distance between the screen and backing determines the shape of the edge of an individual discrete area.

Thus, development and investigation of the methods of forming the discrete-matrix structure is one of the relevant tasks in the problem of improvement of physico-mechanical properties of the surface.

The objective of this work is strengthening the inner surfaces of cylindrical holes by forming discrete-matrix coatings at ion-plasma nitriding.

INVESTIGATION PROCEDURE

Investigations were conducted with application of an experimental vacuum unit, fitted with a source of constant regulated voltage, high-frequency generator and pulse modulator, made with vacuum electronic instruments GU-81M. Owing to their characteristics, these instruments automatically limit the current and load by a preset value and interrupt the arcing process, which is accompanied by explosion-like local destruction of the cathode surface.

Experiments were conducted on tubular specimens of outer diameter of 30 mm, and inner diameter of 12 mm and length of 240 mm. The main material was 40KhN2MA steel, as its composition and properties are close to those of a material, from which it is possible to make arms barrels that is highly relevant now for improvement of the defense capability of Ukraine. Chemical composition of this steel is as follows, wt.%: 0.41 C; 0.31 Si; 0.57 Mn; 0.003 S; 0.017 P; 0.8 Cr; 1.37 Ni; 0.07 W; 0.01 V; 0.21 Mo; 0.18 Cu; 0.001 Ti; 0.016 Al; 0.009 N, and its mechanical properties and heat treatment in keeping with the certificate of quality are given in the Table.

Microhardness measurements on the inner surfaces were performed over the microsection using PMT-3 hardness meter with 50 g loading on the indenter; wear resistance was determined by shaft-block schematic, the counterbody was a rod of 10 mm diameter from carbon steel, quenched to 28–35 *HRC* hardness. The coating microstructure and chemical composition were determined in scanning electron microscope REM-1061, fitted with energy-dispersive microanalyzer OXFORD x-act. Diffractometric analysis was conducted using X-ray diffractometer Rigaku Ultima IV.

INVESTIGATION RESULTS

The nitriding process was conducted in the mode of an anomalous glowing discharge, when the entire surface of the cathode electrode (of the part in our case) participates in the discharge and is covered by plasma glow. Voltage in such a discharge is equal to hundreds of volts, and the part current density is up to 10 mA/cm^2.

Parameters of the mode of high-frequency pulsed nitriding that ensures stable burning of the anomalous glowing discharge are given below:

Pressure in the process chamber, Pa 25–350
Voltage U, kV 0.8–1.0
Current density, mA/cm^2 9
Pulse frequency f_0, kHz 10
Pulse ratio Q 1.5–2.0
Process duration, h 5–6

A mixture of 75 % N_2 + 25 % Ar was used as the working gas, and pure argon was applied for surface cleaning at the initial stage.

Specimen temperature during nitriding did not exceed 580 °C. It was regulated by varying such parameters of the pulsed power supply mode as voltage and pulse ratio.

Pulse frequency on the level of 10 kHz was established, proceeding from the conditions of preventing the anomalous glow discharge transition into the arc discharge, which damages the surface of products and may lead to rejects. Thus, application of pulsed nitriding mode ensures stability of the process of diffusion saturation of the surface without electric breakdowns or arcing, and the mode of anomalous glow discharge

is realized in keeping with the volt-ampere characteristic of electric discharge. Pulse ratio has an important role in this process, its reduction leading to localization of the plasma volume in the tubular specimen. It can be compensated by voltage increase. However, it causes overheating on the specimen surface, resulting in undesirable structural transformations. The uniformity of plasma combustion was indirectly evaluated by specimen heating using thermocouples located on specimen edges and in its middle. If the glow discharge is uniformly distributed along the entire specimen length, the temperature difference between the thermocouples does not exceed 10 °C.

Nitriding of inner surfaces of holes in tubular specimens was realized as follows: a tubular anode of 5 mm diameter with side holes and one end plugged was coaxially installed inside the specimen, the anode open end was connected to a pipeline for feeding working gas of 75 % N_2 + 25 % Ar, so that the gas entered through the anode side holes into the specimen cavity and then escaped into the vacuum chamber, which was continuously pumped down (Figure 1). The cathode-specimen and the anode were fixed by special insulators mounted on a common continuous platform.

Holes in the tubular anode were arranged so as to prevent overlapping of nitrided zones with maximum nitrogen concentration (Figure 2, *a*). Taking into account the anode outer diameter, and inner diameter of the hollow cathode, as well as distribution of nitrogen concentration field over the cross-section, the holes were made every 20 mm at an angle of 120°.

The experimental specimen (Figure 2, *b*) was cut up so that a complex of studies could be performed. In the middle part, specimen No.1 was cut out in the form of a ring for microscopic investigations, then specimens Nos 2 and 3 were cut off in the form of semi-rings for wear resistance testing by shaft-sleeve scheme. On the specimen surface one can also see a hole for mounting a tubular thermocouple, which was placed into a ceramic case to ensure electric decoupling.

The fields of nitrogen concentration distribution over the cross-section of specimen No. 1 are given in Figure 3, *a*, which leads to the conclusion about

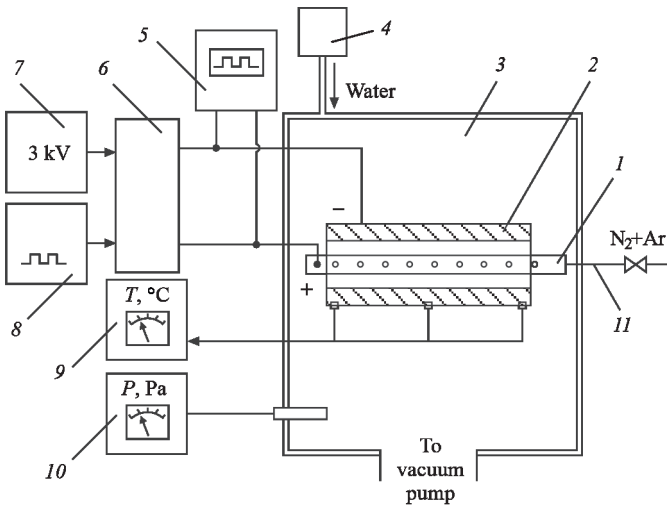

Figure 1. Schematic of an experimental unit for ion-plasma nitriding: *1* — tubular anode with holes for gas feeding; *2* — hollow nitrided cathode-specimen; *3* — vacuum chamber; *4* — vacuum chamber water-cooling block; *5* — oscillograph; *6* — modulator; *7* — DC source with voltage regulation; *8* — pulse generator with variable frequency and ratio; *9* — thermocouples and temperature measuring device; *10* — device for measuring the chamber pressure; *11* — vacuum lead valve for working gas

the nouniformity of nitrogen distribution over the cross-section. The maximum concentration is observed from the side opposite the holes in the tubular anode. The curve of the change of nitrogen concentration in the cross-section (Figure 3, *b*) shows bends, the first small one at 15 μm distance from the surface with nitrogen concentration on the level of 21 at.% and the second one at 60 μm with nitrogen concentration on the level of 6 at.%. No further changes were observed which is related to the low sensitivity of the microanalyzer.

Figure 4, *a* shows the microstructure of a nitrided layer of specimen No. 1 in the area of maximum nitrogen concentration, where surface zones of different nitrogen concentration are observed, and Figure 4, *b* gives the microhardness variation, respectively.

Analysis of the results of determination of the nitrided layer chemical composition showed that the structure is layered, and it consists of several zones: nitride one on the surface where γ′-phase formed and nitrous ferrite. Alloying elements of chromium and

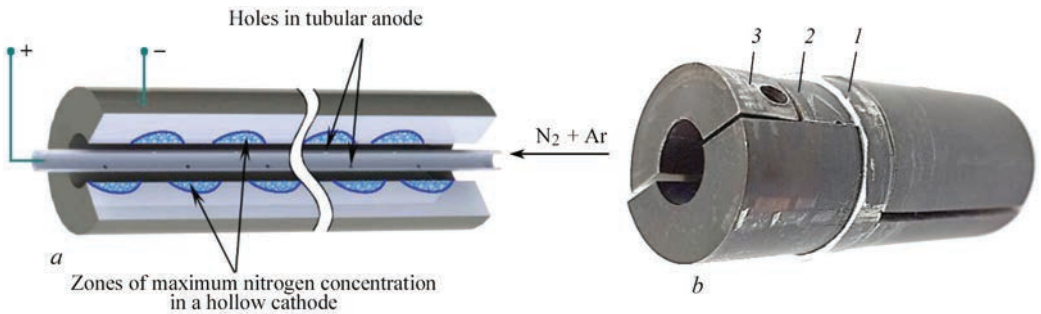

Figure 2. Schematic of location of diffusion zones of discrete-matrix nitriding along the tubular specimen (*a*) and experimental specimen (*b*), cut up into parts (*1–3*) to conduct microscopic investigations and microscopic tests

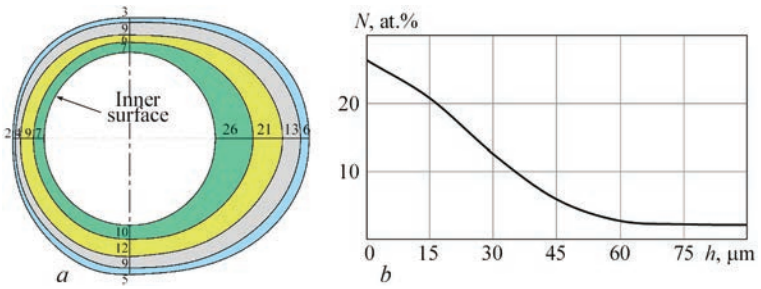

Figure 3. Distribution of nitrogen concentration (at.%) over the cross-section of specimen No. 1 (*a*) and radially from the center in the zone with maximum nitrogen concentration (*b*)

nickel dissolve in ferrite, and increase nitrogen solubility in α-phase, forming special nitrides. Precipitating in the fine-dispersed state these nitrides cause an increase in the nitrided layer hardness, predominantly in lower layer of the saturated zone. Chromium, as a transition element, actively interacts with nitrogen and improves nitrogen solubility in α-phase. Zone I with γ′-phase is very thin and brittle. After nitriding, nitrogen content on the surface of zone I reaches 8.97 wt.% (26.38 at.%). In keeping with iron-nitrogen constitutional diagram, iron nitrides will form at nitrogen concentration of about 20 at.%, which leads to maximum hardness on the level of 805 MPa near the surface. In zone II the chemical composition of the nitrided surface differs both from the initial and the nitrided layer: nitrogen content is up to 6.25 wt.% (20.8 at.%) at 6 μm distance. Zone III, where the nitrided layer formed, also demonstrated changes in the chemical composition: nitrogen amount decreased to 3.5 wt.% (12.6 at.%) at 25 μm distance, the last zone adjacent to the base has nitrogen content of 1.57 wt.% (5.96 at.%) at 46.26 μm distance. At the distance of approximately 100 μm the amount of oxygen is equal to 0.57 wt.% (2.22 at.%).

Results of diffractometric analysis (Figure 5) conducted near the surface of specimen No. 1 showed the presence of Fe_2N phase on the level of 7 %, the balance being α-Fe and Fe_3C at 92 and 1%, respectively.

Based on the obtained data on nitrogen concentration distribution over the specimen cross-section (Figure 3, *b*) showing the presence of a white nitride zone on the surface (Figure 4, *a*) that is confirmed by the results of diffractometric analysis (see Figure 5) we can conclude that application of ion-plasma nitriding of the inner surfaces using a hollow perforated anode results in formation of diffusion coatings, consisting of areas of different chemical and phase composition. Maximum nitrogen concentration is observed in the areas located opposite the holes in the anode, made at a certain distance (see Figure 2, *a*). Accordingly, the same areas contain a hard phase from iron nitride, which corresponds to increased wear resistance of the nitrided surface, i.e. there is every sign of the presence of a certain discrete arrangement of the hard nitride phase in a soft matrix of α-iron that corresponds to discrete-matrix coatings.

In order to confirm this conclusion and study the impact of discrete-matrix coatings produced by

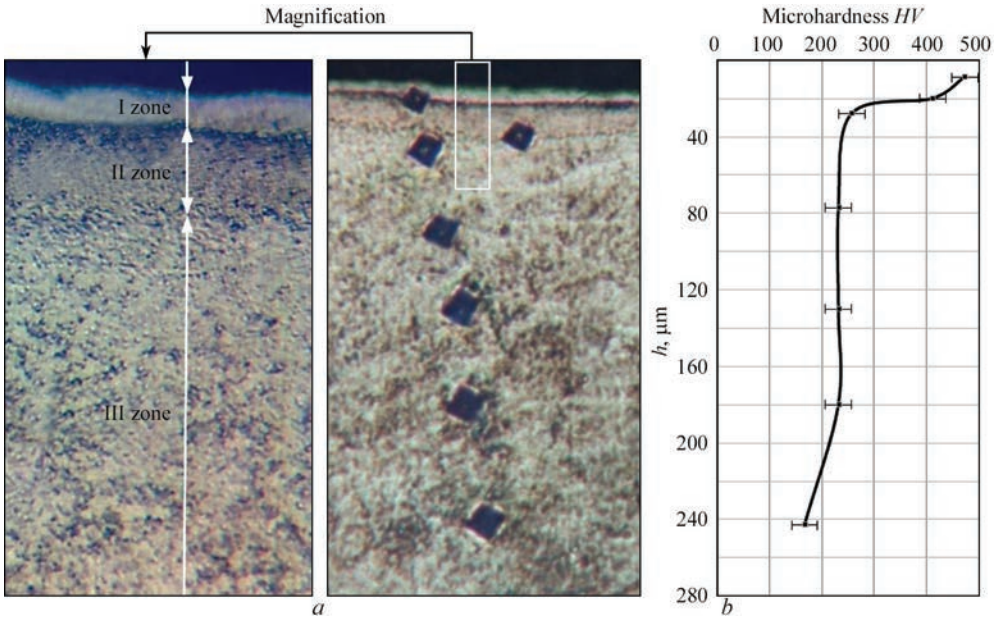

Figure 4. Microstructure of nitrided surface with maximum amount of nitrogen (*a*) and change of microhardness in the cross-section from the tubular specimen surface (*b*)

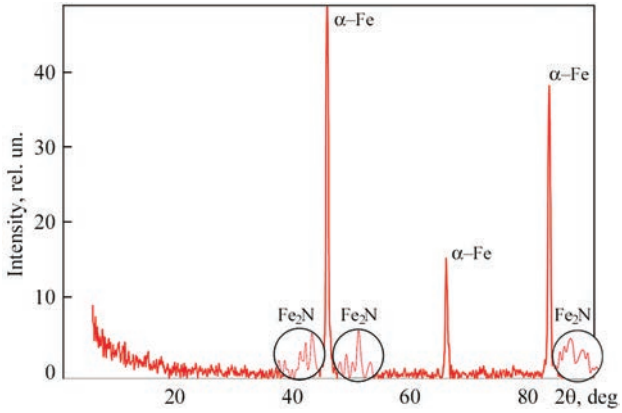

Figure 5. Diffractogram of the surface layer of specimen No. 1 in the area with maximum amount of nitrogen

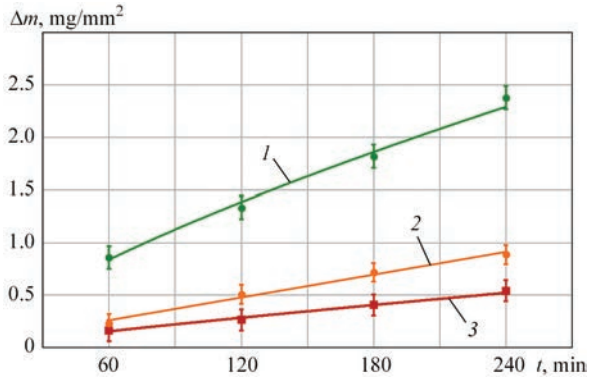

Figure 6. Kinetics of wear of 40KhN2MA steel specimens in the initial condition and after ion-plasma nitriding: *1* — initial specimen; *2*, *3* — nitrided specimens Nos 2 and 3, respectively

ion-plasma nitriding on wear resistance, friction tests were conducted on specimens, cut out of various areas, which have different dimensions, have or do not have nitride zone I with a high nitrogen concentration on the surface and maximum hardness, respectively, that is demonstrated by wear results (Figure 6).

As we can see, the highest wear resistance was observed in specimen No. 3, cut out opposite the hole in the anode. After wearing of the nitride zone with maximum hardness, this specimen demonstrates a loss of mass with its uniform increase. Specimen No. 2 cut out with 15 mm shifting from the hole in the anode, demonstrates a uniform loss of mass, as in the case with specimen No. 3 that is attributable to a more homogeneous structure of the nitrided layer, however, the wear resistance is 1.8 times lower. In general, wear resistance of all the nitrided specimens after testing for 240 min is 2–3 times higher than that of the initial non-nitrided specimen. This is indicative of the good prospects for application of discrete-matrix coatings, and relevance of their further investigations. Obtained results are universal and can be applied for hardening other steels to be nitrided.

CONCLUSIONS

1. Technological modes were developed for pulsed ion-plasma nitriding of inner surfaces on the base of an experimental vacuum unit, fitted with a source of constant regulated voltage, high-frequency generator and pulse modulator. Owing to their characteristics, these instruments automatically limit the load current by a preset value and interrupt the arcing process, which is accompanied by explosion-like local destruction of the cathode surface of the specimen, which is inadmissible.

2. Conducted investigations showed that ion-plasma nitriding of inner surfaces with application of a hollow perforated anode, leads to formation of diffusion coatings, which consist of areas of different chemical and phase composition. Maximum concentration of nitrogen on the level of 8.97 wt.% (26.38 at.%) is found in areas, which were located opposite the holes in the anode, made at a certain distance at a certain angle. Accordingly, the same areas contain a hard phase from iron nitride, discretely located in the soft matrix of α-iron.

3. Testing under the conditions of dry friction of metal against metal showed that the wear resistance of specimens, taken from different areas of the nitrided specimens, is 3–5 times higher than that of the initial non-nitrided specimens that is indicative of their high wear resistance and attractiveness of their further studies.

4. Further on, proceeding from investigation results, it is planned to develop the technological schedule for specific tubular products, the inner holes of which are to be hardened by nitriding.

REFERENCES

1. Pastukh, I.M. (2006) T*heory and practice of hydrogen-free nitriding in glow discharge.* Kharkov, NNTs KhFTI [in Russian].
2. Kaplun, V.G., Kaplun, P.V. (2015) *Ion nitriding in hydrogen-free media.* Khmelnitsky, KNU [in Russian].
3. Pye, D. (2003) *Practical Nitriding and Ferritic Nitrocarburizing.* ASM International Park, Ohio.
4. *Hossein* Aghajani, Sahand Behrangi (2016) *Plasma Nitriding of Steels.* Springer International Publ.
5. Farghali, A., Aizawa, T. (2017) Phase transformation induced by high nitrogen content solid solution in the martensitic stainless steels. *Materials Transact*., **58**, 697–700. DOI: https://doi.org /10.2320/matertrans.M2016418
6. Aizawa, T., Wasa, K. (2017) Low temperature plasma nitriding of inner surfaces in stainless steel mini-/micro-pipes and nozzles. *Micromachines*, **8**, 157. DOI: https://doi.org/10.3390/mi8050157
7. Pokorný, Z., Kadlec, J., Hruby, V. et al. (2011) Hardness of plasma nitrided layers created at different conditions. *Chemicke Listy*, **105**, 717–720.
8. Latas, Z., Michalski, J., Tacikowski, J., Betiuk, M. (2013) Azotowanie regulawane luf broni strzeleckiej. *Inzynieria Powierzchni*, **1**, 26–33.
9. Lyashenko,, B.A., Movshovich, A.Ya., Dolmatov, A.I. (2001) Reinforcing coatings of discrete structure. *Tekhnologicheskie Sistemy*, **4**, 17–25 [in Russian].
10. Lyashenko, B.A., Soroka, E.B., Rutkovsky, A.V. (2002) Determination of discrete structure parameters of coatings taking into account the residual stresses. *Problemy Prochnosti*, **4**, 119–125 [in Russian].

11. Katoh, T., Aizawa, T., Yamaguchi, T. (2015) Plasma assisted nitriding for micro-texturing martensitic stainless steels. *Manufacturing Rev*., **2**, 7. DOI: https://doi.org/10.1051/mfreview/2015004
12. Matveev, N.V. (2007) Vacuum producing of discrete wear-resistant coatings using forming separator. *Svarochn. Proizvodstvo*, **5**, 35–38 [in Russian].

ORCID
V.V. Lysak: 0000-0002-6565-2793,
M.O. Sysoyev: 0000-0001-7243-2388,

CONFLICT OF INTEREST
The Authors declare no conflict of interest

CORRESPONDING AUTHOR
A.V. Chornyi
E.O. Paton Electric Welding Institute of the NASU
11 Kazymyr Malevych Str., 03150, Kyiv, Ukraine.
E-mail: black803@gmail.com

SUGGESTED CITATION
I.V. Smirnov, A.V. Chornyi, V.V. Lysak, M.O. Sysoyev, G.P. Kysla (2022) Ion-plasma nitriding of inner cylindrical surfaces of products. *The Paton Welding J*., **11**, 21–26.

JOURNAL HOME PAGE
https://patonpublishinghouse.com/eng/journals/tpwj

Received: 17.10.2022
Accepted: 29.12.2022

DOI: https://doi.org/10.37434/tpwj2022.11.05

CONTROL OF ENERGY PARAMETERS OF PLASMA FLOWS OF N–O–C–H SYSTEM

V.M. Pashchenko

National Technical University of Ukraine "Igor Sikorsky Kyiv Polytechnic Institute"
37 Peremohy Prosp., 03056, Kyiv, Ukraine

ABSTRACT

The methods to control the plasma flow parameters by changing the geometrical dimensions of the arc channel and superposition of external magnetic fields are discussed. The possibility of increasing the temperature level in the entire volume of plasma flow of N–O–C–H system in the case of increasing the diameter of nozzle opening of the arc channel and compensating the velocity losses without deterioration of temperature characteristics due to a simultaneous increase of plasma-forming mixture flow rate is shown. The effectiveness of application of external transverse magnetic fields for harmonizing the relative position of separate phases of the heterogeneous flow at thermal deposition of the coating was proved. It is shown that transverse field application shifts the spatial position of the high-temperature zone of the plasma flow by 11–12° relative to the arc channel axis. Under the condition of radial feed of the initial material, when the channels of mass transfer of the gas and condensed phases of the two-phase flow do not coincide, it allows increasing the volume of spray-deposited material by 1.5–1.7 times, due to penetration of the greater part of the initial material into the active zone of the flow. Dependence of energy parameters of plasma generator and dimensions of the high-temperature gas jet on the frequency of rotation of the external rotating magnetic field and current in electromagnet windings was studied. It was established that optimization of the rotating field parameters allows significantly (up to 20 %) raising the arc voltage parameters and increasing the volume of the high-temperature zone by 25–30 % with simultaneous equalizing of the parameters over the plasma flow cross-section.

KEYWORDS: plasma generator, arc channel, plasma-forming mixture of air with hydrocarbon gas, temperature and velocity profiles of the flow, active zone dimensions, external transverse magnetic field, angle of flow deviation, external rotating magnetic field

INTRODUCTION

While developing technologies for plasma treatment of materials and in the process of implementing these technologies, methods of controlling the energy parameters of plasma flows by changing the operational parameters of the process: arc current, flow rate and composition of the plasma-forming gas are widely used. In many cases, adjusting the plasma generation mode is sufficient to achieve the aim of the control [1, 2]. However, in some cases, in order to achieve a more radical effect, it is necessary to use means that require optimization of the geometric dimensions of the arc channel or use of additional equipment to implement external effects.

Nowadays, many methods of controlling the energy and spatial characteristics of plasma jets have been developed and are used. This can be a direct effect on the parameters and spatial position of a high-temperature gas flow, or an indirect one, predetermined by the effect on the electric arc already at the stage of the plasma flow formation. The most promising are magnetic and gas-dynamic methods, as well as control of changes in the configuration and geometric dimensions of the arc channel.

Magnetic control due to the effect on the spatial position of the electric arc is widely used in welding technologies and related processes. The use of magnetic fields improves the efficiency of electrode metal melting, makes it possible to control the geometric dimensions of the cross-section of deposited beads and welds, refines the structure of the deposited metal and welds, increases hardness, strength and ductility of the weld metal, increases resistance of welds to hot crack formation [3–6].

By changing the diameter and linear dimensions of the output electrode, it is possible to influence the efficiency of the plasma generator and change the specific energy of the plasma jet, although the distribution of energy in the jet volume changes uncontrollably. For example, an increase in the length of the narrow part of the arc channel or the length of the interelectrode insert increases the value of the voltage drop on the arc, and the use of arc chambers with a diameter extension in the direction of gas outflow allows reducing the level of heat flows into the wall and achieve high values of local efficiency [7].

The use of plasma-forming mixtures of the N–O–C–H system without changing the general trends of control by the mentioned methods makes certain adjustments to the results of the practical implementation of these methods of influencing the energy parameters of the arc and, accordingly, the generated plasma flows. The aim of the work is to study the peculiarities of using methods of external magnetic ef-

fect and changes in the dimensions of the arc channel (in particular, diameter of the nozzle opening of the output electrode) with the aim of correcting geometric dimensions, position in space and parameters of the plasma flow of gas systems N–O and N–O–C–H.

RESEARCH PROCEDURES

An experimental study of the plasma flows of the N–O–C–H system was carried out using the Gray's enthalpy probe [8]. The distribution of parameters in the volume of the plasma jet was studied by moving the sampling probe in space using a three-coordinate manipulator. To determine the enthalpy, using the Gray's probe, the heat flow was measured perceived by the sampling probe when a gas sample was pumped through it at a specific local point of the flow. The chemical composition of the selected sample was analyzed in chromatographs of type KhL-3 and LKhM-8-MD. According to the known composition of the cold gas sample, the real chemical composition of the medium was calculated at the point of sampling, taking into account the actual temperature. The temperature was determined by the results of measuring the probe of enthalpy values at a particular point of the plasma flow. The dynamic pressure of the flow was determined by the U-shaped water manometer, to which a capillary of the sampling probe was joined. The energy characteristics of the plasmatron were determined by the results of measuring current, voltage and heat losses to the structure elements by the known procedures [8].

RESEARCH RESULTS AND THEIR DISCUSSION

The studies were conducted in a two-electrode plasmatron of up to 50 kW capacity with a thermochemical cathode, eddy stabilization of the arc in the center of the arc channel and auto gas-dynamic stabilization of the arc length. The local values of plasma temperature and flow velocity, as well as chemical composition of the medium at local points of the plasma jet volume were determined.

According to the results of the studies, the distributions of temperature, velocity of the medium by the

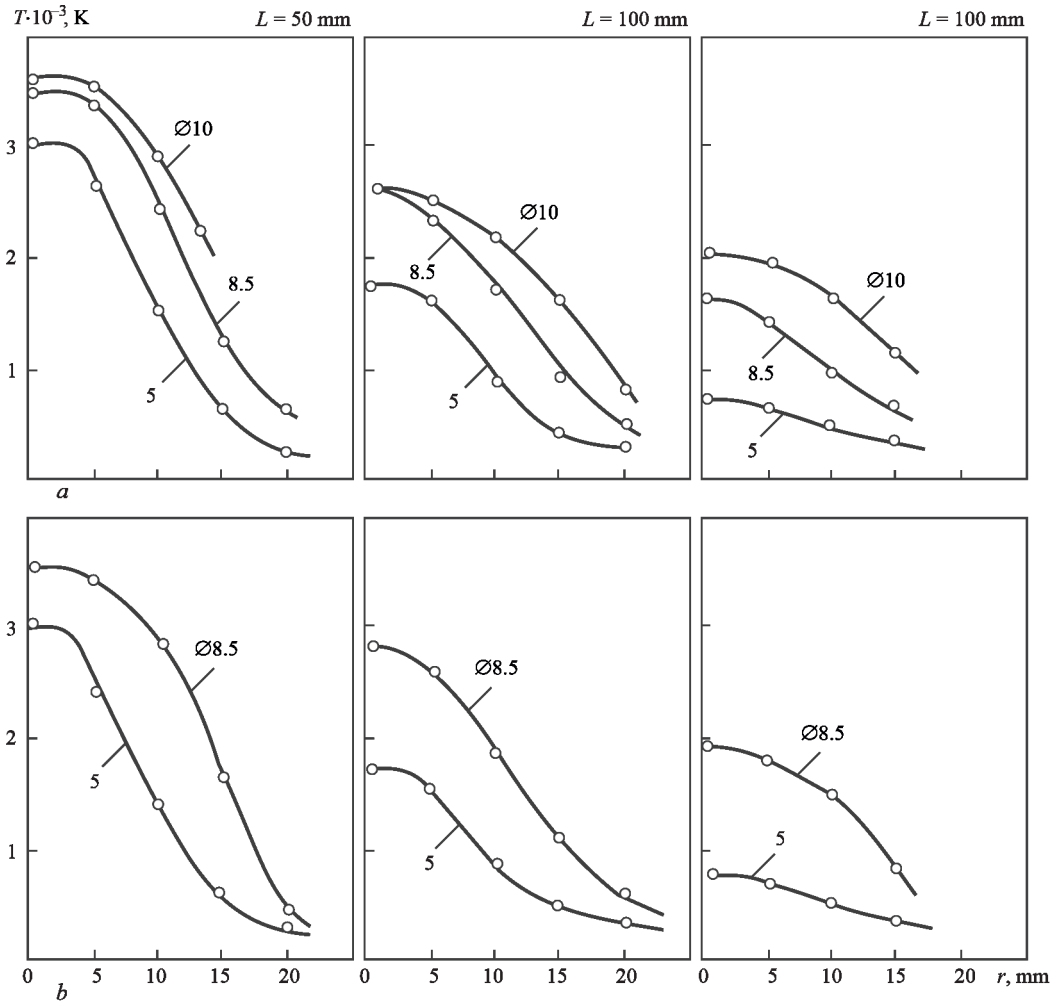

Figure 1. Radial distributions of temperature of plasma gas-air jet under the condition of different diameters of the nozzle opening of the arc channel: *a* — Q_{Σ} = 3.7 m³/h, α = 0.65, *I* = 200 A; *b* — Q_{Σ} = 7.8 m³/h, α = 0.65, *I* = 200 A (r is the distance from the axis of the arc channel on the cross-section of the plasma flow; α is the oxidant flow rate factor)

length of the jet and in its cross-sections were established.

The simplest method as to its technical implementation of effecting the gas-air plasma jet and its sizes on the structure, may be the change in the geometric characteristics of the regions of the arc channel. In particular, it goes about the diameter.

For the studied plasma generator, which was designed for deposition of coatings, the standard diameter of the nozzle part of the output electrode (anode) is 8.5 mm. This size was optimized in terms of achieving a balanced effect in spraying materials of all the most commonly used groups of materials that can be significantly different in melting point and other physicochemical characteristics.

The universal size of the nozzle opening in the arc channel is not always optimal during deposition of specific material. Heating of refractory substances with low thermal conductivity (e.g., oxides) requires an increase in the time of stay of particles in the active plasma jet zone and the sizes of this zone with the preservation (increase) of energy characteristics of the flow. It is not always possible to achieve the required result by a change in the mode characteristics of the process. In addition, the requirement of providing the maximum possible uniformity of temperature and velocity of jet to create the same heating conditions and accelerate the entire array of source material in the whole volume of the two-phase flow should be taken into account. In this case, one of the ways to solve the problem can be a change in the diameter of the nozzle opening of the arc channel.

Figure 1, *a* shows the distribution of the plasma jet temperature for three different diameters of the nozzle opening in the arc channel (the other mode parameters of the plasma generation process being unchanged).

According to the results of the measurements, with an increase in the diameter of the nozzle opening in the arc channel, the temperature at all distances from the section of the plasmatron nozzle (Figure 1, *a*) raises almost proportionally. The relative temperature growth is higher at larger distances. This is the result of intense mixing of a "thin" plasma jet with surrounding air with a reduction in the high-temperature area of plasma jet.

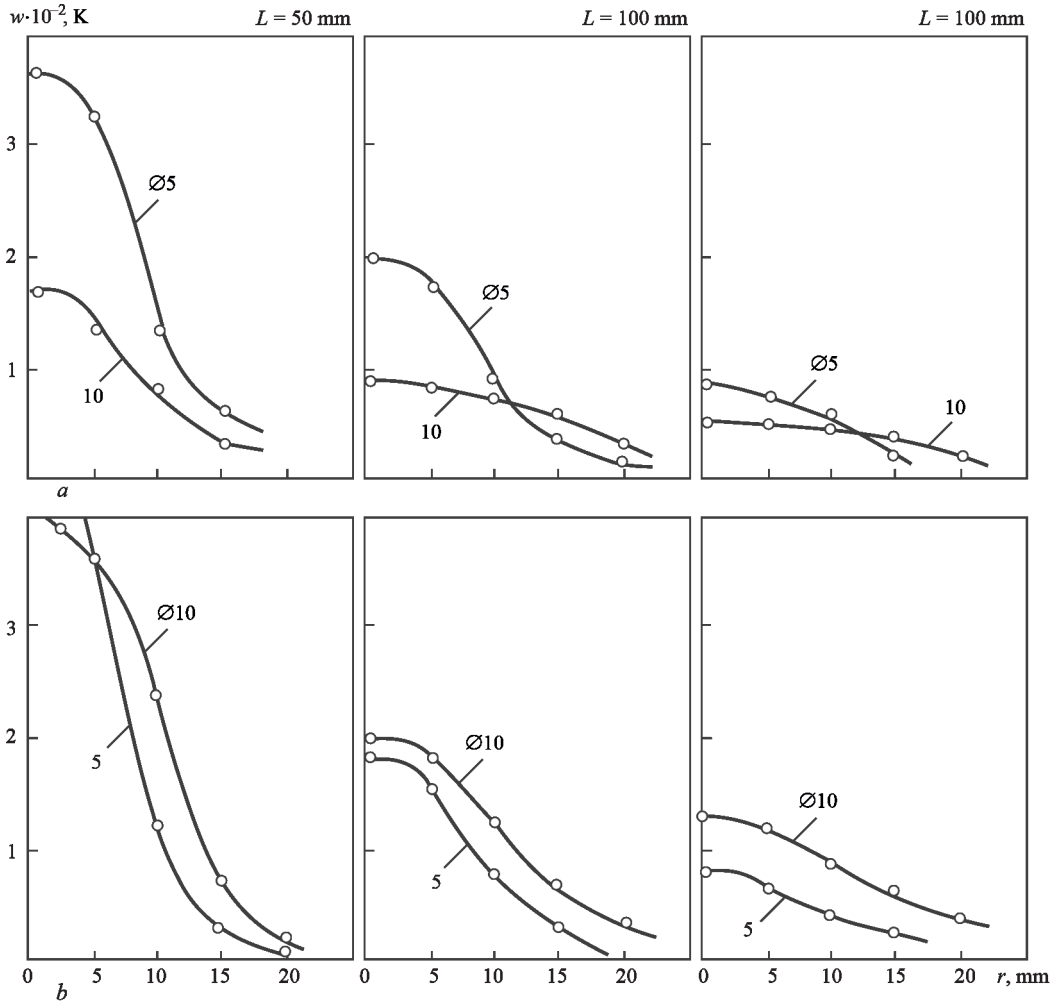

Figure 2. Radial distributions of velocity of gas-air jet under the condition of different diameters of the nozzle opening of the arc channel: *a* — Q_{Σ} = 3.7 m³/h, α = 0.65, *I* = 200 A; *b* — Q_{Σ} = 7.8 m³/h, α = 0.65, *I* = 200 A

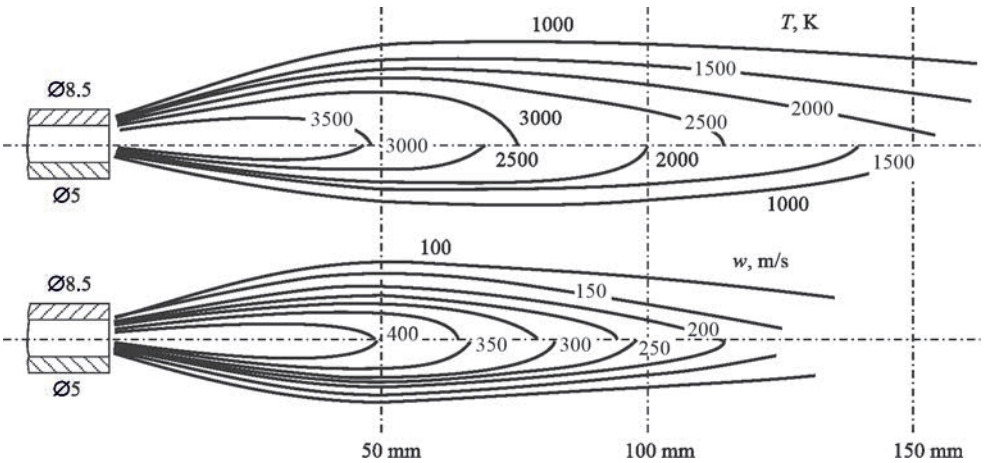

Figure 3. Temperature and velocity profiles for two diameters of the nozzle opening with the compensation for velocity loss by an increase in the flow rate of a plasma-forming mixture

The radial profile of velocities of a "thin" plasma jet is narrower and "sharper" (the absolute value of velocity in the central part of the flow is significantly higher than in the channel velocity profile with a larger diameter). The rate of velocity drop is approximately the same for both diameters, but starting at a distance of 7–8 calibers of the outlet diameter of the arc channel, the generator plasma flow with a larger diameter of the nozzle opening of the arc channel in the peripheral part of the cross-section has already higher velocities than in the plasmatron with a smaller channel diameter (Figure 2, *a*).

Given the abovementioned case, in the general case, an increase in the outlet diameter of the nozzle opening of the arc channel improves the thermal characteristics of the plasma flow of the N–O–C–H system, but, at the same time, its velocity parameters are deteriorated.

A possible compromise may be an attempt to compensate for the velocity drop while increasing the nozzle opening of the arc channel with an increase in the flow rate of the plasma-forming mixture (combination of methods of control of plasma flow energy parameters by changing the plasma generation mode and changing the geometrical sizes of the arc channel). In Figure 1, *b* and Figure 2, *b* present the results of such a control.

A 2.9 times drop in the flow rate due to an increase in the passing opening of the arc channel (from a diameter of 5 mm to a diameter of 8.5 mm) was compensated by a 2.16 times increase in the flow rate of a plasma-forming mixture. Under these clearly worse conditions (compensation for flow rate reduction is inadequate to increase the passing opening), the plasma jet of the generator with a larger diameter of the nozzle opening of the arc channel has higher temperatures at all distances over the whole cross-section of the jet. In this case, the rate of the flow rate drop along the jet axis is lower and the velocity rate on the periphery is higher. While transferring to traditional plasma-forming mixtures, such as air (N–O system) or nitrogen, such effect is not observed.

Given the abovementioned, in the general case, an increase in the outlet diameter of the nozzle opening of the arc channel improves the thermal characteristics of the plasma jet of the N–O–C–H system, but its velocity parameters are deteriorated.

Figure 3 shows profiles of temperature and velocity of plasma jet for the case considered above. The use of plasma generators with an increased diameter of the nozzle opening of the arc channel and a simultaneous compensation of the velocity drop by an increase in the flow rate of a plasma-forming mixture allows increasing the volume of the active plasma flow zone by more than 3 times, and its length — by 1.6 times (without deterioration of the plasma flow).

The use of external effects (in particular, magnetic) to control the plasma flow parameters is somewhat more complex in practical implementation. The effect on the plasma flow is carried out indirectly due to the action on the electric arc. To organize such a control, the use of special magnetic systems is required. Unlike the magnetic effect used in welding and surfacing technologies, the methods of surface engineering, in particular, coating technology, magnetic system is usually located on the plasma generator body, and electromagnetic field acts on the arc, burning in the arc channel within the plasmatron design [8].

External transverse magnetic fields (ETMF) of a permanent and alternating direction and a rotational magnetic field (ERMF) have found practical application in surface engineering technologies.

The aim of the magnetic control of ETMF of the permanent direction during deposition of coating is spatial coordination of channels of mass transfer of the solid and gas phase of the heterogeneous flow. In

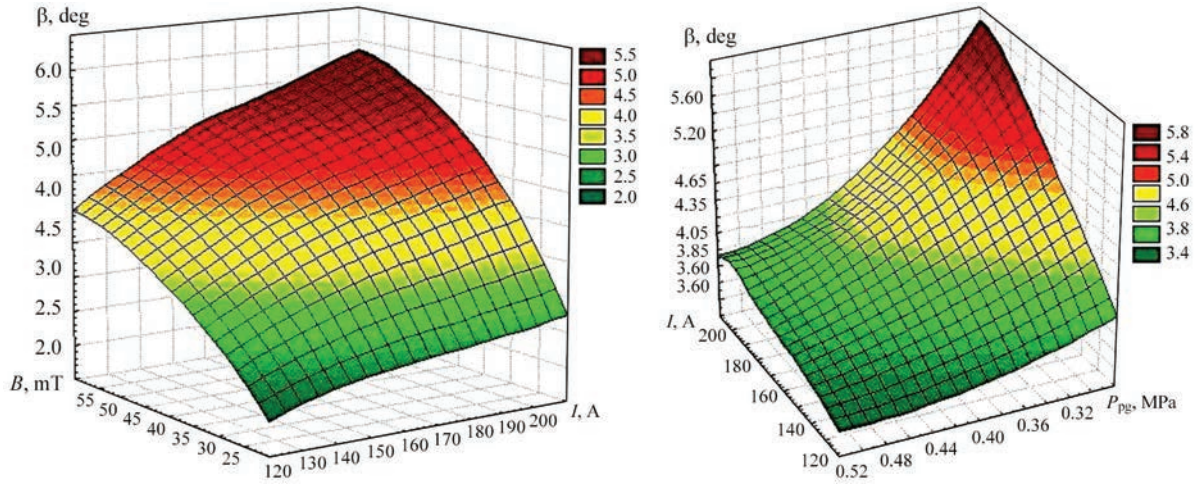

Figure 4. Dependence of the deviation angle of the flow on the mode parameters of plasma generation and magnetic field characteristics

case of using ETMF, the direction of induction of the magnetic field is perpendicular to the current direction in the arc column. By changing the electric arc position within the arc channel and the place of the arc binding by the magnetic field, it is possible to rebuild the energy characteristics of the arc in space (both integral, as well as local values of enthalpy, velocity, chemical composition of the working medium). Practically, the result of ETMF effect is a deviation of the plasma outflow direction from the longitudinal axis of the arc channel. It is known that the direction of transfer of the solid phase in a two-phase flow in the case of using radial supply of the source material in the gas flow, which is the most common in practice deposition of thermal coatings, does not coincide (by a few degrees) with the direction of the plasma outflow from the axisymmetric channel. Thus, using ETMF, it becomes possible to coordinate the directions of transferring the solid phase of the heterogeneous flow and the spatial profiles of temperature and velocity of a high-temperature gas flow. The result of such coordination will be improving the conditions of heating and accelerating of a larger fraction of particles of the source material and, accordingly, the quality of the produced coating and the efficiency of the spraying process.

The direction and deviation angle depend on the direction of the magnetic field induction.

The dependence of the deviation angle of the plasma flow β on the induction of the external magnetic field B and the pressure of the plasma-forming gas P_{pg} at different values of the arc current I_a is presented in Figure 4.

The induction of the magnetic field varied in the range of $18–55 \cdot 10^{-3}$ Tl, and the arc current of the plasmatron I_a varied within 130–200 A. As is seen from Figure 4, an increase in the arc current and the value of the magnetic field induction lead in general case to an increase in the deviation angle of the plasma flow due to a proportional increase in the Ampere force. In the studied range of variation in the mode parameters, the total possible deviation angle reaches 11–12°.

In the case of using ETMF in the course of coating deposition, the effect of the magnetic field can be most clearly observed on the example of the "spraying spot" formation on the surface of the base (Figure 5). The shape of the spraying spot becomes more symmetrical and noticeably increases by area.

Under the condition of using the field of permanent direction, the volume of sprayed material significantly increases (for example, by 1.5–1.7 times for PG-19M-01 powder) and the thickness of the coating layer considerably grows, especially in the central part of the spraying spot.

The aim of the magnetic control of ERMF during deposition of coating is to equalize the parameters of the plasma jet in the cross-sections at the active region of the flow and intensify heat exchange between the phases of a heterogeneous flow. A multipolar magnetic system is used, in which a pair of mutually perpendicular poles of electromagnet is switched on in a certain sequence [8]. As a result, a rotational magnetic field is generated, that changes by the program the direction and speed of rotation, as well as the value of magnetic induction in the gap between the poles.

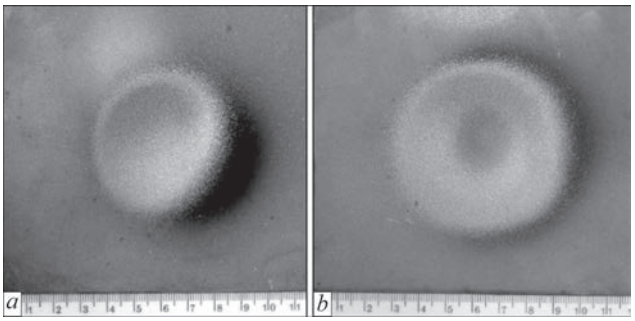

Figure 5. Spot of spraying ferromagnetic material PG-10N-04: *a* — without field; *b* — ETMF of permanent direction

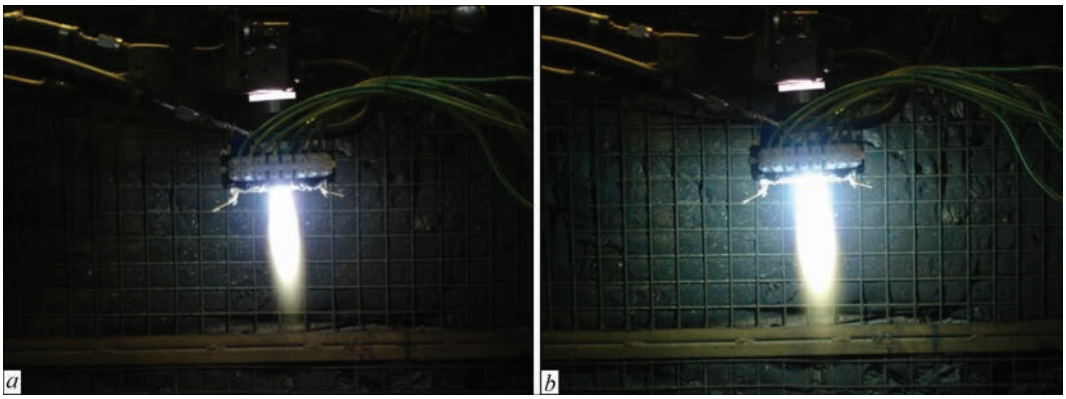

Figure 6. Plasma jet under the condition of action of rotational magnetic field: *a* — at the absence of field; *b* — at the presence of magnetic field

The studies prove that during superposition of the rotational magnetic field, the visible volume of a high-temperature zone of the plasma flow is changed (Figure 6).

The change in volume can be recorded by videos digital camera with the subsequent processing of the obtained by means of the scanning image processing program.

It was established that in the case of coincidence of the rotation directions of the magnetic field and the initial twist of the gas, a significant visible change in the volume of a high-temperature flow area is not observed in the whole studied range of changes in the field rotation frequency. The value of voltage on the arc is also almost does not change.

In the case of opposite directions of the field rotation and the initial twist of a plasma-forming gas due to a significant change in the conditions of heat exchange of arc with gas, the integral value of the arc voltage increases by 15–20 % (obviously, due to a local increase in the field intensity on the part of the arc column and the near-electrode area of the arc on the output electrode) (Figure 7).

The dependencies bear an extreme character. The maximum voltage value is achieved at a certain frequency of field rotation (moreover, the position of the extremum changes depending on the current in electromagnet windings).

Increasing the voltage at a constant current leads to an increase in the power of the device, which, in turn, leads to an increase in the volume of a high-temperature region of the plasma flow (Figure 8). Simultaneously, equalization of temperature and velocity profiles in the plasma jet occurs.

The dependence of the volume of a high-temperature part of the jet on the frequency bears an extreme nature. The position of the extremum to some extent depends also on the current in electromagnet windings: it shifts into the area of lower frequencies with a decrease in current.

The emergence of extremum can be explained by the arc getting in its “hot” trace in the arc channel of

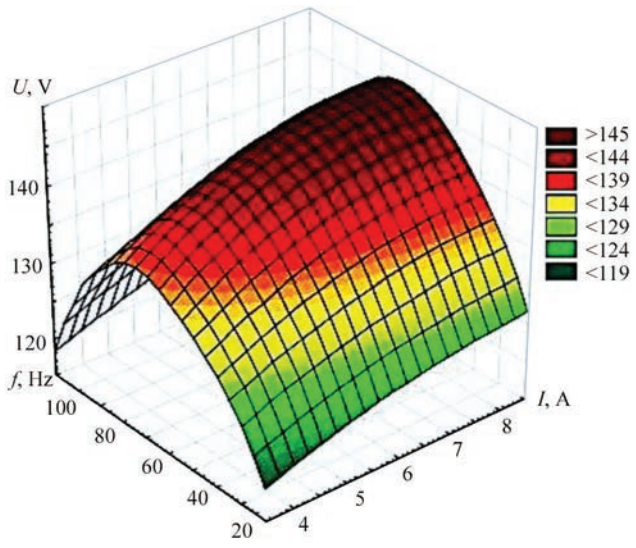

Figure 7. Effect of field rotation frequency and current in electromagnet windings on the integral value of arc voltage

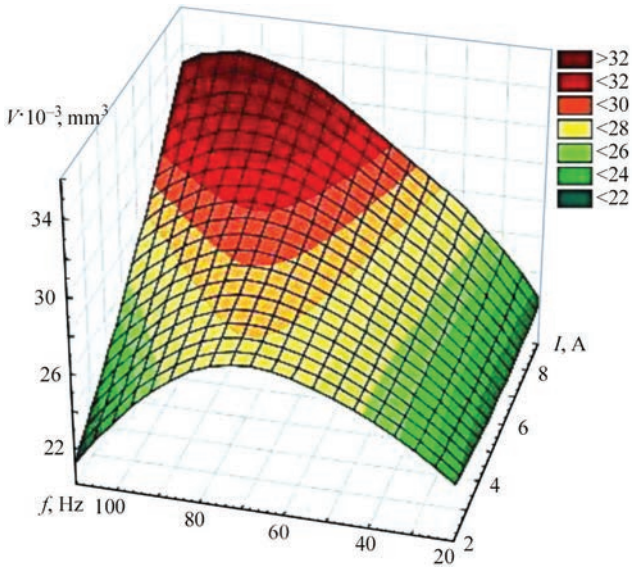

Figure 8. Dependence of plasma jet volume on frequency of external magnetic field and current in electromagnet windings

the plasma generator at an increased frequency of field rotation.

Moreover, the nature of the heat exchange of the arc with gas is noticeably changed by additional factors that affect the appearance of extreme dependence of volume on frequency, is to reduce the radius of the arc precession in case of lagging of its velocity from that of the field, as well as reducing of the effective value of current in electromagnet windings due to an increase in their inductive resistance and reducing the time of current passing in each winding.

CONCLUSIONS

The use of air mixtures with hydrocarbon gases makes the method of controlling the sizes of the active temperature zone of the plasma jet by changing the diameter of the nozzle opening of the arc channel with simultaneous compensation for the loss of velocity by increasing the flow rate of a plasma-forming mixture promising. The use of this method allows increasing the volume of the active plasma flow zone by more than 3 times, and its length — by 1.6 times (without deterioration of the plasma flow velocity characteristics).

The external transverse magnetic field due to the effect on the position of the electric arc in the arc channel of the plasma generator harmonizes the mutual position of the channels of mass transfer of gas and condensed phase of a two-phase flow during radial supply of the source material that allows 1.5–1.7 times increase in the volume of sprayed material and an increase in the thickness of the coating layer, especially in the central part of a spraying spot.

In the case of using a rotational external magnetic field due to a significant change in the conditions of heat exchange of the arc with gas and a change in intensity in individual regions of the arc column and its near-electrode area, the voltage on the arc increases significantly by 15–20 % and the volume of a high-temperature zone increases by 25–30 % with a simultaneous equalizing of the parameters on the cross-section of the plasma flow.

REFERENCES

1. Borisov, Yu.S., Vojnarovich. S.G., Kislitsa, A.N. et al. (2017) Development of technology of microplasma spraying for restoration of local damages of enamel coating. *The Paton Welding J.*, **7**, 28–32.
2. Borisov, Yu.S., Vojnarovich, S.G., Kislitsa. A.N., Kalyuzhny, S.N. (2016) Influence of technological factors of microplasma spraying of TiO_2 on the degree of spraying material utilization. *The Paton Welding J.*, **10**, 46–47.
3. Ryzhov, R.M., Kuznetsov, V.D. (2010) *Magnetic quality control of welded joints*. Kyiv, Ekotekhnologiya [in Ukrainian].
4. Razmyshlyaev, O.D., Ahieieva, M.V., Bilyk, O.G., Khaled, E. (2021) Influence of longitudinal control magnetic field on efficiency of arc surfacing process. *Automatychne Zvaryuvannya*, **8**, 9–13.
5. Kachinskiy, V. (2012) Magnetically-impelled arc butt welding for manufacture of hollow parts of mass production. *Welding Technology J. Japan*, **60.**
6. Hua, A., Yin, S., Chen, S. et al. (2010) Behavior of arc and drop transfer of MAG welding controlled by longitudinal magnetic field. *J. of Mechanical Engineering*, 46(**14**), 95–100.
7. Dautov, G.Yu., Dzyuba, V.L., Karp, I.N. (1984) *Plasmatrons with stabilized electric arcs*. Kyiv, Naukova Dumka [in Russian].
8. Pashchenko, V.M. (2018) *Arc generators in technologies of surface engineering*. Kharkiv, Machulin [in Ukrainian].

ORCID

V.M. Pashchenko: 0000-0003-3742-6913

CORRESPONDING AUTHOR

V.M. Pashchenko
National Technical University of Ukraine
“Igor Sikorsky Kyiv Polytechnic Institute”
37 Peremohy Prosp., 03056, Kyiv, Ukraine.
E-mail: vn.paschenko@ukr.net

SUGGESTED CITATION

V.M. Pashchenko (2022) Control of energy parameters of plasma flows of N–O–C–H system. *The Paton Welding J.*, **11**, 27–33.

JOURNAL HOME PAGE

https://patonpublishinghouse.com/eng/journals/tpwj

Received: 26.09.2022
Accepted: 29.12.2022

DOI: https://doi.org/10.37434/tpwj2022.11.06

EFFECT OF PRELIMINARY ACTIVATION OF TiAl POWDER ON THE PROCESS OF MECHANOCHEMICAL SYNTHESIS OF $(Fe, Ti)_3Al$ INTERMETALLICS

Yu.S. Borysov[1], O.M. Burlachenko[1], N.V. Vihilianska[1], C. Senderowski[2]

[1]E.O. Paton Electric Welding Institute of the NASU
11 Kazymyr Malevych Str., 03150, Kyiv, Ukraine
[2]University of Warmia and Mazury
2 Michata Oczapowskiego Str., 10719, Olsztyn, Poland

ABSTRACT

The effect of mechanical activation of TiAl powder on the structural and phase transformations in mechanochemical synthesis of the powder mixture of the composition 60.8Fe + 39.2TiA1, intended to produce Fe_3Al intermetallics, alloyed with titanium was studied. Using a semi-empirical Miedema's model, the changes of Gibbs energy for the binary Ti–Al, Fe–Ti and Fe–Al systems were calculated. The results showed that the driving force for the formation of intermetallic phases for all the binary systems is higher as compared to the formation of solid solutions and amorphous phases. A range of compositions was established, at which the formation of amorphous phases in the binary Ti–Al and Fe–Al systems is possible. Carrying out the mechanical activation of TiAl intermetallic powder in a high-energy planetary mill allowed reducing the size of a coherent scattering region from 280 to 9 nm with a partial amorphization. The formation of particles with a homogeneous microstructure consisting of intermetallic phase $(Fe, Ti)_3Al$ and Laves phases — Fe_2Ti was revealed in the process of mechanochemical synthesis of a powder mixture 60.8Fe + 39.2 TiAl when using nanostructural TiAl powder. The change in the region of coherent scattering of powders of 60.8Fe + 39.2TiAl mixture, produced by the method of mechanochemical synthesis, was evaluated and it was established that interaction of a nanostructural powder TiAl with Fe begins to occur when the size of a coherent scattering region becomes <70 nm. The resulting product has an amorphous-nanocrystalline structure with a size of the coherent scattering region of <15 nm. The use of the developed powder in thermal spraying technologies will allow producing coatings based on Fe_3Al intermetallics with a nanocrystalline structure, a higher modulus of elasticity and ductility.

KEYWORDS: mechanochemical synthesis, mechanical activation, titanium aluminide, semi-empirical Miedema's model, nanocrystalline structure, amorphous phase

INTRODUCTION

One of the modern technologies for producing powders for thermal spraying (TS) is the method of mechanochemical synthesis (MChS). This method, taken into account its simplicity and cheapness, has found its use for producing nanostructural powders of iron aluminide [1]. The combination of high strength and corrosion properties of iron aluminides makes these alloys promising materials for using as protective coatings on the blades and housings in the compressor of jet engines, design elements of aircrafts, heating elements, in heat exchangers, in components of nuclear reactors, on automobile piston valves, etc. [2, 3]. The main advantage of iron aluminides as compared to heat-resistant nickel alloys and stainless steels is the availability and cheapness of the basic iron component, as well as the ease of their machining. Introduction of iron of the third element to aluminide will allow increasing their mechanical characteristics. As alloying components, Ti, V, Cr, C, etc. are used [4]. The use of titanium as an alloying element leads to the formation of an intermetallic compound Fe_2TiA1 ($L2_{1,}$ triple equivalent Fe_3Al ($D0_3$) structure), which allows increasing the temperature of a phase transition $L2_1 \rightarrow B2$ from 550 to 1215 °C and stabilizing the ordered structure to higher temperatures as compared to binary system [5].

About the formation of an intermetallic compound $(Fe, Ti)_3A1$ during the process of MChS of powder mixtures of the stochiometric composition $Fe_{50}A1_{25}Ti_{25}$ (at.%) was reported in [1, 6]. It was found that the process of formation of $(Fe, Ti)_3Al$ intermetallics depends on the source materials. While using the powders of Fe, Ti and Al as the source materials, the formation of intermetallics passes through the stages of forming layered composites of Fe/Al/Ti with their subsequent transformation into a solid Fe(Al, Ti) solution, and then into the intermetallic phase $D0_3$ $(Fe, Ti)_3Al$ [6]. In the case of using TiAl-Fe as the source powders, the phase transformations are accompanied by the formation of ferrotitanium followed by dissolving of Al in its lattice up to the formation of $(Fe, Ti)_3Al$ intermetallics [1].

The use of preliminary mechanical activation (MA) of the source powders allows increasing the reactivity of solid substances, which is associated with the accumulation of crystalline structure defects and an increase in the enthalpy of a material [7]. The use of MA in the technology of self-propagating high-temperature synthesis (SHS) allows expanding

the capabilities of gas-free burning for a high-temperature synthesis by increasing the burning rate and a significant decrease in the reaction initiation temperature. The burning rate during MA of the powder mixture 27Ti + 13B + 60Cu (wt.%) increases by ~42 % (from 6.25 to 14.8 mm/s), and that of the the mixture $22.4B_4C$ + 77.6Ti (wt.%) grows by ~49 % (from 11 to 22.5 mm/s) [8, 9].

The aim of this work was to study the influence of preliminary mechanical activation of TiAl intermetallic powder on structural and phase transformations occurring in the process of MChS of the powder mixture 60.8Fe + 39.2TiAl, intended to produce Fe_3Al intermetallics alloyed with titanium.

MATERIALS AND RESEARCH PROCEDURES

As the source materials to produce the powder of the Fe–TiAl system, iron powder and TiAl powder were used (Table 1).

The amount of TiAl intermetallic powder, introduced into the mixture with iron powder, amounted to 39.2 wt.%, which, at such a ratio of components, allows producing a single-phase product based on Fe_3Al intermetallic in the MChS process [10].

MA and MChS processes were carried out in a planetary mill (Activator 2S1) at the drum rotation speed of 1500 rpm, the ratio of balls mass to powder mass of 10:1, the medium is air. In order to eliminate sticking of the processed charge on the grinded bodies and drum walls, as well as to intensify the process of synthesis of new phases, a surface-active substance (SAS) — oleic acid ($C_{17}H_{33}COOH$) in the amount of 0.5 wt.% was added to the mixture. The time of preliminary MA was 3 h and the time of MChS was 5 h.

The sequence of structural and phase transformations during MChS in the Fe–Al–Ti system using MA of TiAl powder was studied on the particles removed from the reactors after certain time intervals (0.5, 1.5 and 3 h).

The chemical analysis of the produced composite powders (CP) was studied in the JSM-6390LV scanning electron microscope (JEOL, Japan) with the attachment for energy dispersive analysis INCA ENERGY (Oxford Instruments, Great Britain), in the mode of secondary electrons in a low (10^{-4} Pa) vacuum with an accelerating voltage of 20 kV.

Table 1. Characteristics of source powders used to produce MChS powder of the Fe–TiAl system

Powder	Grade	Chemical composition, wt.%	Particle size, μm
Fe	PZhR	Fe > 98.5	80–100
TiAl	PVT65Yu35	Ti – 67.5; Al – 32.5	<20 μm

X-ray diffraction phase analysis (XRD) was performed using the Ultima IV diffractometer (Rigaku, Japan) in CuK_α-radiation with a graphite monochromator. The phase identification was carried out using the international database ICDD PDF-2 or PDF-4 by computer processing of the received digital data. Using the PDXL program for harmonic analysis, provided by the Rigaku X-ray unit, an evaluation of the coherent scattering region (CSR) was carried out.

THERMODYNAMIC EVALUATION OF THE POSSIBILITY FOR PROCEEDING REACTION IN THE Fe–Ti–Al SYSTEM

The evaluation of the possible reactions proceeding in the Fe–Ti–Al system was carried out for the binary Ti–Al, Fe–Ti and Fe–A1 systems with the calculation of change in the Gibbs energy for the crystalline (intermetallic, solid solution) and amorphous states with a continuous series of component concentrations. The analysis was performed using Miedema's semi-empirical model for binary systems (Figure 1) [11, 12].

The obtained results indicate that the driving force for the formation of intermetallics in all the ranges of compositions for binary systems is higher as compared to the solid solution and the amorphous state. For the amorphous state at certain compositions of binary systems, there are positive values of the Gibbs energy (Table 2).

Based on the carried out calculations, it can be noted that in the Fe–Ti–Al system, the formation of Ti–Al (when Al < 85 mol.%) and Fe-Ti (when Ti > 85 mol.%) compounds is possible. For the Ti–Al and Fe–A1 systems in the range of 32 mol.% < X_{A1} <

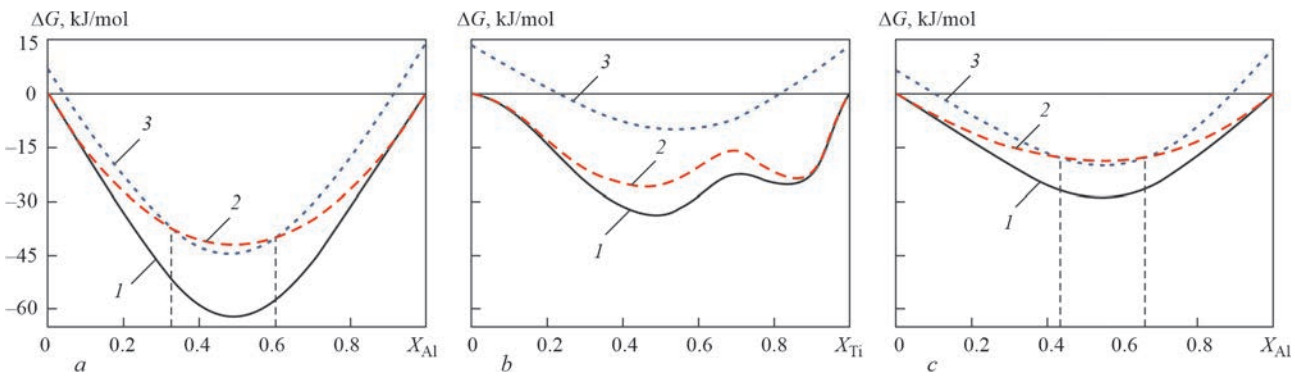

Figure 1. Change in Gibbs energy in the Ti–Al (*a*), Fe–Ti (*b*) and Fe–Al (*c*) systems for: *1* — intermetallics; *2* — solid solutions; *3* — amorphous state

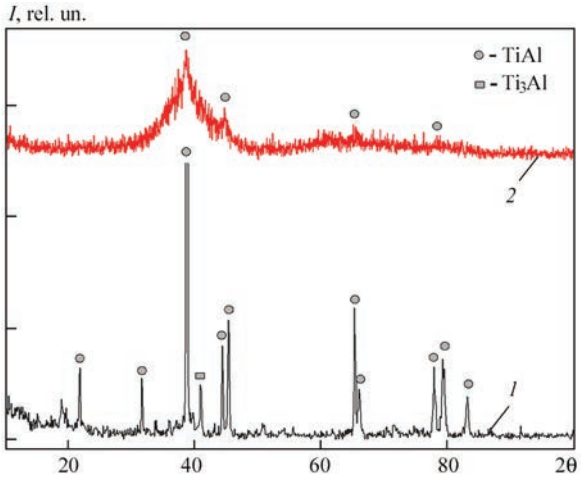

Figure 2. X-ray patterns of TiAl source powder (*1*) and TiAl powder after mechanical activation (within 3 h) (*2*)

< 76 mol.%, the free Gibbs energy for the formation of compounds in the amorphous state is lower than for solid solutions, which indicates the possibility of the amorphous phase formation in these systems [13].

Transferring TiAl into the amorphous state will allow reducing its thermodynamic stability, which can contribute to the intensification of the process of interaction of TiAl with Fe in the MChS process.

RESEARCH RESULTS AND THEIR DISCUSSION

Using the XRD method, it was established that MA of the source TiAl powder during 3 h leads to the broadening of diffraction lines and a decrease in their intensity. A strong blurring of peaks at large angles makes their identification difficult. The calculation of CSR showed a decrease in the average value from 280 to 9 nm. The appearance of a "halo" on X-ray patterns indicates a partial amorphization of the powder (Figure 2).

Table 2. Ranges of compositions, in which the value ΔG of the amorphous phase formation is positive

System	Composition range, mol.%
Fe–Al	$X_{Al} < 0.05$ and $X_{Al} > 0.95$
Fe–Ti	$X_{Al} < 0.2$ and $X_{Al} > 0.88$
Ti–Al	$X_{Al} < 0.03$ and $X_{Al} > 0.97$

The microstructure and appearance of Fe–TiAl powder particles produced by the MChS method at different time of processing are presented in Figure 3.

Analyzing the appearance of the powders, it is possible to note the developed surface of the particles, which indicates that the formation of conglomerates in the MChS process occurs due to welding of small particles of the source components with each other.

Studying the microstructure of particles produced at different stages of MChS, it is possible to note the formation of thin lamellar conglomerates at the early stages and the homogenization of the structure at the later stages.

With the use of X-ray spectral microanalysis, the chemical composition of the powder particles produced at different durations of the MChS process was determined (Table 3). There is no significant difference observed between the calculated composition of the mixture 60.8Fe + 39.2TiAl (wt.%) and the actual chemical composition of the resulting product. Only the presence of oxygen in the amount of 2–5 % is noted, which is associated with the MChS process carried out in air.

The interaction of Fe with a nanostructured TiAl powder in the MChS process takes place in several stages. At the initial stages, refinement of iron takes place. The formation of an amorphous "halo" at the place of the X-ray peak at $2\Theta = 38°$ indicates the amorphization of TiAl. Further, the merging of an amorphous "halo"

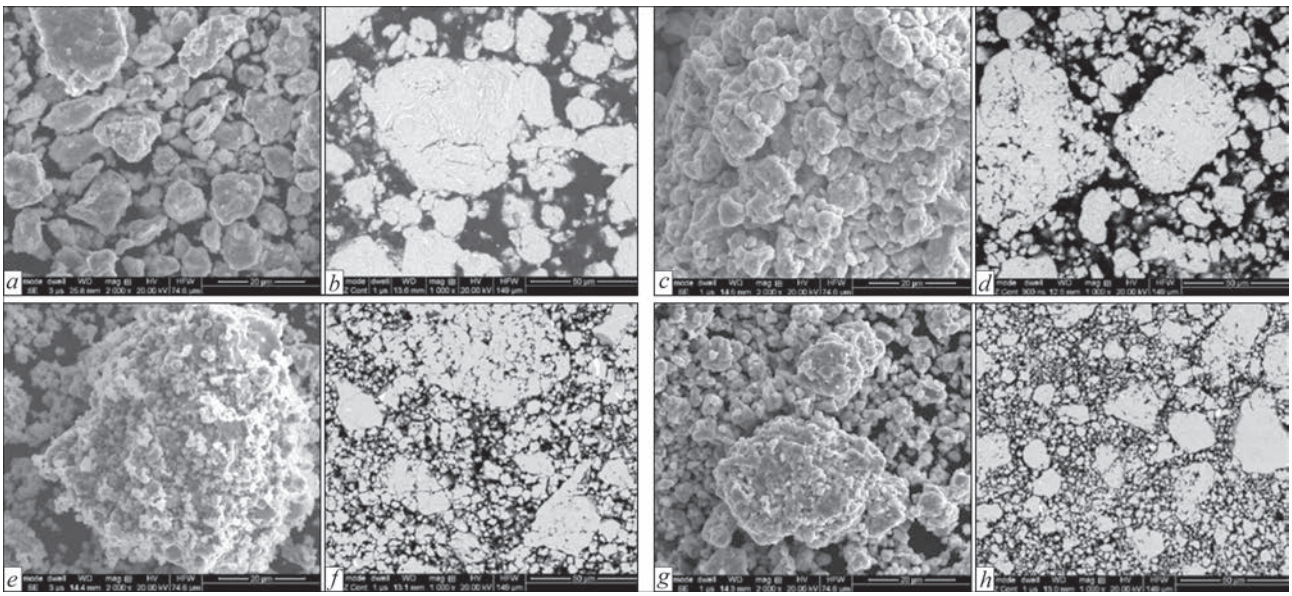

Figure 3. Appearance (*a*, *c*, *e*, *g*) and microstructure (*b*, *d*, *f*, *h*) of particles of a composite powder produced by the MChS method from mixture (wt.%) 60.8Fe + 39.2TiAl (mechanically activated TiAl) within 0.5 h (*a*, *b*); 1.5 h (*c*, *d*); 3 h (*e*, *f*) and 5 h (*g*, *h*)

Table 3. Chemical composition of composite powder particles at different stages of processing the mixture 60.8Fe + 39.2TiAl (wt.%)

Processing time, h	Content of elements, wt.%			
	Fe	Ti	Al	O
Source composition	60.8	26.5	12.7	–
0.5	57.85 ± 1.45	25.05 ± 0.46	14.71 ± 0.22	2.39 ± 0.76
1.5	62.03 ± 1.51	26.13 ± 0.30	9.24 ± 3.65	2.60 ± 0.42
3	53.71 ± 4.38	23.65 ± 1.45	18.27 ± 2.74	5.04 ± 1.27
5	55.38 ± 3.20	24.41 ± 0.91	14.97 ± 0.40	5.24 ± 0.38

of TiAl with the diffraction maximum of Fe and a mutual overlapping of the diffraction lines of TiAl and Fe is observed. This indicates the formation of a ternary intermetallic $(Fe, Ti)_3Al$ compound. At the same time, a strong blurring and a low intensity of Fe peaks at large angles ($2\Theta > 70°$) make their identification difficult. As a result of the interaction of Ti with Fe, after 3 h of processing, a diffraction peak appears in the range of angles $2\Theta = 36–38°$, indicating the formation of Fe_2Ti compound (Laves phase) (Figure 4).

Thus, schematically, the structural and phase transformations in the MChS process of the mixture 61Fe + 39TiAl in the case of using intermetallic TiAl powder with CSR = 9 nm can be represented as follows:

$$\mathrm{Fe(CSR = 276\,nm) + TiAl(CSR = 9\,nm)} \rightarrow$$
$$\xrightarrow{0.5\mathrm{h}} \mathrm{Fe(CSR = 170\,nm) + TiAl_{amorph.}} \rightarrow$$
$$\xrightarrow{+1.0\mathrm{h}(\Sigma 1.5\mathrm{h})} \mathrm{Fe - TiAl(CSR = 54\,nm)} \rightarrow$$
$$\xrightarrow{+1.5\mathrm{h}(\Sigma 3.0\mathrm{h})} \mathrm{(Fe, Ti)_3Al(CSR = 25\,nm) +}$$
$$\mathrm{+Fe_2Ti_{traces}} \xrightarrow{+2.0\mathrm{h}(\Sigma 5.0\mathrm{h})}$$
$$\rightarrow \mathrm{(Fe, Ti)_3Al(CSR \sim 10\,nm) + Fe_2Ti(CSR \sim 15\,nm).}$$

Comparing the scheme of structural and phase transformations occurring during the MChS process using unactivated TiAl powder with CSR = 280 nm, it can be noted that unlike the mixture with a nanostructured TiAl powder, an interaction of titanium with iron occurs with the formation of ferrotitanium, dissolution of aluminium in the ferrotitanium lattice and formation of intermetalic $(Fe, Ti)_3Al$ [1]:

$$\mathrm{Fe(CSR = 276\,nm) + TiAl(CSR = 280\,nm)} \rightarrow$$
$$\xrightarrow{0.5\mathrm{h}} \mathrm{Fe(CSR = 175\,nm) +}$$
$$\mathrm{+TiAl(CSR = 68\,nm)} \rightarrow$$
$$\xrightarrow{+1.0\mathrm{h}(\Sigma 1.5\mathrm{h})} \mathrm{Fe(CSR = 68\,nm) +}$$
$$\mathrm{+TiAl(CSR = 51\,nm) +}$$
$$\mathrm{+FeTi_{traces}} \xrightarrow{+1.5\mathrm{h}(\Sigma 3.0\mathrm{h})} \mathrm{solid\ solution\ Al\ in}$$
$$\mathrm{FeTi(CSR = 44\,nm)} \xrightarrow{+2.0\mathrm{h}(\Sigma 5.0\mathrm{h})}$$
$$\rightarrow \mathrm{(Fe, Ti)_3Al(CSR \sim 30\,nm).}$$

Evaluation of the change in CSR on the broadening of the X-ray lines of iron at the initial stages of the MChS process and $(Fe, Ti)_3Al$ after 5 h of processing the Fe + TiAl mixture in a planetary mill showed that the use of a nanostructured TiAl intermetallics as a source powder leads to producing a final product with a size of CSR <15 nm (Figure 5). The size of CSR of the $(Fe, Ti)_3Al$ phase in the case of using an intermetallic powder with a size of CSR = 280 nm after 5 h of processing reaches ~30 nm.

Analyzing the changes in the phase composition and CSR at different stages of mixture processing, it can be noted that merging of the X-ray peaks of TiAl

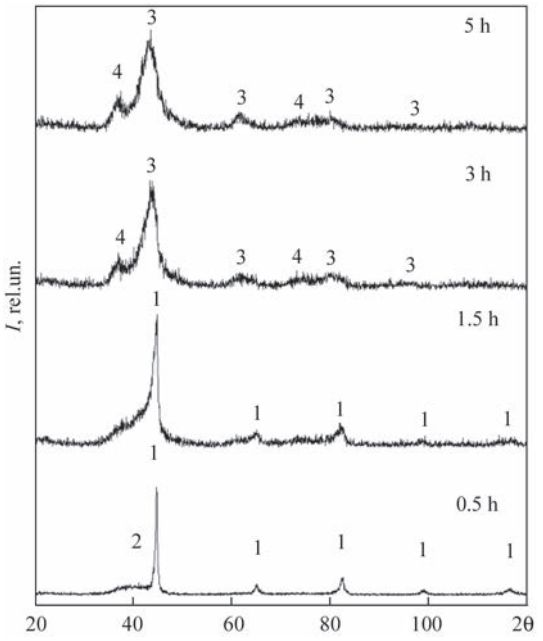

Figure 4. X-ray patterns of MChS powders of the composition 61Fe + 39TiAl (when using nanostructured TiAl powder): *1* — Fe; *2* — TiAl; *3* — $(Fe, Ti)_3Al$; *4* — Fe_2Ti

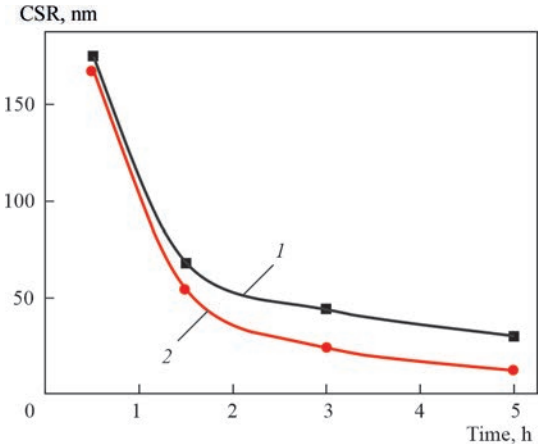

Figure 5. Change in CSR depending on time of MChS of 61Fe+39TiAl mixture (*1* — TiAl, CSR — 280 nm; *2* — TiAl, CSR — 9 nm)

and Fe after 1.5 h of processing occurs when the size of the crystallites becomes <70 nm.

Thus, the use of a preliminary mechanically activated TiAl powder for producing intermetallic (Fe, Ti)$_3$Al powder by the MChS method allows intensifying the process of refining the structure with a reduction in the size of CSR by 1.3 times after 1.5 h of processing (from 68 to 54 nm), and by three times after 5 h of processing (from 30 to 10 nm).

The developed powder of (Fe, Ti)$_3$Al intermetallics can be used in the technology of thermal spraying of intermetallics of coatings with a nanocrystalline structure, increased mechanical characteristics (Young modulus and hardness) and high indices of ductility.

CONCLUSIONS

1. Using the technology of mechanical activation of TiAl intermetallic powder, a nanostructured powder with CSR of ~9 nm was produced.

2. The process of structural and phase transformations occurring in the process of mechanochemical synthesis in a powder mixture of iron and a nanostructured TiAl intermetallic powder was studied. The mechanism of formation of (Fe, Ti)$_3$Al intermetallic consists of producing thin lamellar conglomerates of Fe and TiAl, the subsequent homogenization of the powder microstructure and synthesis of the intermetallic (Fe, Ti)$_3$Al phase (CSR ~ 10 nm) and Laves phase Fe_2Ti (CSR ~ 15 nm).

3. It was revealed that the use of a preliminary mechanically activated TiAl powder to produce intermetallic (Fe, Ti)$_3$Al powder by the MChS method allows intensifying the process of refining the structure, which is confirmed by a reduction in the size of CSR after 1.5 h of processing by 1.3 times (from 68 to 54 nm), and by 3 times after 5 h of processing (from 30 to 10 nm).

REFERENCES

1. Borisov, Yu.S., Borisova, A.L., Burlachenko,A.N. et al. (2017) Structure and properties of alloyed powders based on Fe_3Al intermetallic for thermal spraying produced using mechanochemical synthesis method. *The Paton Welding J.*, **9**, 33–39. DOI: https://doi.org/10.15407/tpwj2017.09.06
2. Cinca N., Lima C.R.C., Guilemany J.M. (2013) An overview of intermetallics research and application: Status of thermal spray coatings. *J. of Materials Research and Technology*, 2(**1**), 75–86.DOI: https://doi.org/10.1016/j.jmrt.2013.03.013
3. Moszner, F., Peng, J., Suutala, J. et al. (2019) Application of iron aluminides in the combustion chamber of large bore 2-stroke marine engines. *Metals*, 9(**8**), 847. DOI: https://doi.org/10.3390/met9080847
4. Palm, M., Stein, F., Dehm, G. (2019) Iron aluminides. *Annual Review of Materials Research*, **49**, 297–326. DOI: https://doi.org/10.1146/annurev-matsci-070218–125911
5. Alonso, P.R., Gargano, P.H., Bozzano, P.B. et al. (2011) Combined ab initio and experimental study of A2+$L2_1$ coherent equilibria in the Fe–Al–X (X = Ti, Nb, V) systems. *Intermetallics*, **19**, 1157–1167. DOI: https://doi.org/10.1016/j.intermet.2011.03.025
6. Rafiei, M., Enayati, M.H., Karimzadeh, F. (2009) Characterization and formation mechanism of nanocrystalline (Fe, Ti)$_3$Al intermetallic compound prepared by mechanical alloying. *J. of Alloys and Compoun*ds, 480(**2**), 392–396. DOI: https://doi.org/10.1016/j.jallcom.2009.02.072
7. Lyakhov, N.Z., Talako, T.L., Grigorieva, T.F. (2008) *Influence of mechanoactivation and phase- and structure formation in self-propagating high-temperature synthesis.* Novosibirsk, Parallel [in Russian].
8. Rogachev, A.S., Mukasyan, A.S. (2012) *Combustion for synthesis of materials: Introduction in structural microkinetics*. Moscow, FIZMATLIT [in Russian].
9. Korchagin, M.A., Dudina, D.V. (2007) Application of self-propagating high-temperature synthesis and mechanical activation for producing of nanocomposites. *Fizika Goreniya i Vzryva*, **2**, 58–71 [in Russian].
10. Borisova, A.L., Timofeeva, I.I., Vasilkovskaya, M.A. et al. (2015) Phase and structural transformations in formation of intermetallic powders of Fe–Al system by mechanochemical synthesis method. *Poroshk. Metallurgiya*, **7–8**, 135–143. DOI: https://doi.org/10.1007/s11106–015–9740–5
11. Mousavi, M.S., Abbasi, R., Kashani-Bozorg, S.F. (2016) A Thermodynamic approach to predict formation enthalpies of ternary systems based on miedema's model. *Metal. Mater. Transact. A*, **47**, 3761–3770. DOI: https://doi.org/10.1007/s11661–016–3533–4
12. Zhang, R.F., Zhang, S.H., He, Z.J. et al. (2016) Miedema calculator: A thermodynamic platform for predicting formation enthalpies of alloys within framework of Miedema's Theory. *Computer Physics Communications*, **209**, 58–69. DOI: https://doi.org/10.1016/j.cpc.2016.08.013
13. Li, H., Lu, X., Liu, Y. et al. (2013) Thermodynamic calculation of glass formation for Co–ETM alloys based on Miedema's model. *Physica B: Condensed Matter.*, **413**, 24–30. DOI: https://doi.org/10.1016/j.physb.2012.12.035

ORCID

Yu.S. Borysov: 0000–0002–6019–8464,
O.M. Burlachenko: 0000–0001–8576–2095,
N.V. Vihilianska: 0000–0001–8576–2095,
C. Senderowski: 0000–0002–0331–3702

CONFLICT OF INTEREST

The Authors declare no conflict of interest

CORRESPONDING AUTHOR

N.V. Vihilianska
E.O. Paton Electric Welding Institute of the NASU
11 Kazymyr Malevych Str., 03150, Kyiv, Ukraine.
E-mail: pewinataliya@gmail.com

SUGGESTED CITATION

Yu.S. Borysov, O.M. Burlachenko, N.V. Vihilianska, C. Senderowski (2022) Effect of preliminary activation of TiAl powder on the process of mechanochemical synthesis of (Fe, Ti)$_3$Al intermetallics. *The Paton Welding J.*, **11**, 34–38.

JOURNAL HOME PAGE

https://patonpublishinghouse.com/eng/journals/tpwj

Received: 25.07.2022
Accepted: 29.12.2022

DOI: https://doi.org/10.37434/tpwj2022.11.07

THE INFLUENCE OF COPPER ON THE HEAT RESISTANCE OF THIN FOILS OF HIGH-ENTROPY ALLOYS OF THE Cr–Fe–Co–Ni–Cu SYSTEM PRODUCED BY ELECTRON BEAM PHYSICAL VAPOUR DEPOSITION METHOD

A.I. Ustinov, S.O. Demchenkov, T.V. Melnychenko, O.Yu. Klepko

E.O. Paton Electric Welding Institute of the NASU
11 Kazymyr Malevych Str., 03150, Kyiv, Ukraine

ABSTRACT

The paper investigated the heat resistance of sheet materials based on the Cr–Fe–Co–Ni–Cu system, depending on copper content in the alloy. It is shown that the content of copper in the composition of high-entropy alloys significantly affects the heat resistance of the material: in the case of CrFeCoNiCu alloy foils, the increase in specific mass at a temperature of 900 °C occurs 8 times more intensively than in CrFeCoNi foils, due to activation of the diffusion of copper atoms, its coming to the surface of the foil and formation of scale based on CuO and NiO oxides with a significant number of defects in the structure. CrFeCoNi alloy foils are characterized by higher heat resistance due to formation of scale based on Cr_2O_3 oxide on the surface with fewer defects and greater continuity. The average mass growth rate of the CrFeCoNi alloy sample is about 0.041 mg/(cm^{2}h).

KEYWORDS: high-entropy alloys, electron beam deposition, ingot, thin foils, heat resistance

INTRODUCTION

Sheet materials are required for fabrication of structures with a low specific weight. Among them special attention is given to thermal protection three-layer honeycomb panels, which are considered to be an efficient means for protection of structural elements of aerospace equipment from heating at their interaction with the atmosphere at high speeds. In view of that, the sheet materials used for their manufacturing should have a complex of properties such as heat resistance, strength and low specific weight. Alloys based on Ti–Al [1], Ni–Cr [2] systems and other are traditionally considered as such materials. Thin foils from these materials are usually produced by rolling bulk cast billets, or they are formed by powder metallurgy methods. Such an approach, however, greatly complicates the technology of producing sheet materials and makes it inefficient in terms of power. In this connection, producing thin foil with the required complex of properties and methods of its joining is still a relevant problem.

Over the recent years, considerable attention has been given to the so-called high-entropy alloys (HEA) [3] which are characterized by high strength and thermal stability, wear and corrosion resistance, as well as hydrophobicity and weldability [4-6]. Owing to such features, HEA are regarded as promising materials for producing functional coatings, foils and other components for aviation and automotive industry [7, 8]. At present HEA thin films and coatings are produced by the methods of magnetron sputtering [9], cathode-vacuum-arc vapour-phase deposition [10], thermal spraying [11] and laser cladding [12]. At the same time, these methods are characterized by relatively low production efficiency.

In earlier works [13–16] the authors showed in the case of CrFeCoNiCu HEA that the method of high-speed electron beam vapour phase deposition (EBPVD) allows producing vacuum foils with a rather wide range of micromechanical characteristics, high damping properties and good weldability. Combination of such properties in the produced foils allows considering such materials as promising for manufacturing structural elements of thermal protection honeycomb panels. At the same time, practical application of such thermal protection panels envisages the possibility of their operation for a long time under higher temperature conditions. In view of that, in this work the heat resistance of foils of HEA of Cr–Fe–Co–Ni–Cu and Cr–Fe–Co–Ni systems made by EBPVD method, was studied.

EXPERIMENTAL

Foils of Cr–Fe–Co–Ni–Cu system alloys with different copper content were produced by electron beam evaporation of the respective ingot-target with subsequent deposition of the vapour phase on the substrate from stainless steel (AISI 302) heated up to specified temperature. Foils of 40–100 μm thickness were deposited at the rate of approximately 100 nm/s at substrate temperatures in the range of 550–750 °C. To ensure foil

separation from the substrate, a thin layer of CaF_2 was first deposited on it. Initial ingots-targets of 50 mm diameter were produced in an induction furnace.

Microstructural studies of the foils and their local chemical analysis were conducted in a scanning electron microscope (SEM) CamScan4, fitted with ENERGY 200 microanalyzer. The foil overall thickness was evaluated by its cross-section in SEM images. X-ray diffractometer DRON-4M (Cu-K_α-radiation) was used to conduct phase analysis.

Heat resistance of the produced foils was studied by the change of specimen specific weight during annealing at the temperature of 900 °C in a shaft-type electric furnace SShOL-2.4/12.5 in atmospheric air.

EXPERIMENTAL RESULTS AND THEIR DISCUSSION

Prior research showed that foils of CrFeCoNiCu alloy are characterized by a combination of quite high values of microhardness and ductility, as well as damping ability on the level of high-damping materials [15, 16].

When studying the heat resistance of CrFeCoNiCu foils it was established (Figure 1, curve *1*) that intensive increase of specific weight occurs during the first 6 hours of heat treatment at the temperature of 900 °C, reaching the values of approximately 8 mg/cm^2. Further soaking for 30 hours does not lead to any significant growth of the foil specimen weight.

According to the results of scanning electron microscopy, in the initial state the thickness of CrFeCoNiCu foil is approximately 60 μm, and it is characterized by a defectfree structure and uniform distribution of the components over the thickness (Figure 2, *a*). Chemical composition, averaged over the foil thickness, is given in Table 1. In the initial state the foil structure consists of two FCC-phases, one of which is enriched in copper, and the other is depleted in copper (Figure 2, *b*) [16]. It should be noted that the two-phase composition is characteristic for foils of this system HEA, deposited at substrate temperature above 750 °C. However, chemical composition of the phases is somewhat different for HEA produced from the vapour phase and by metallurgical methods: in cast alloys copper content in the copper-enriched phase is more than 80 wt.%, while in vacuum foils its content is not higher than 40 wt.% [15, 16]. By the data of electron microscopy, after CrFeCoNiCu foil soaking in the furnace for six hours at the temperature of 900 °C in atmospheric air, foil thickness increases up to 90–95 μm, and layered scale of 15–20 μm thickness forms on the foil surfaces with a considerable number of defects of the type of pores, delaminations and cracks (Figure 2, *c*). Chemical analysis of different scale areas (Figure 2, *d*, Table 1) showed that the surface layers of the scale are represented by iron-based oxides, while deeper-lying scale layers are a complex oxide, which includes all the foil components with the prevailing content of copper. The composition of the foil surface layers is similar which is indicative of the low ability of the formed scale to prevent oxygen atom penetration in-depth of the foil material. Further annealing of samples of CrFeCoNiCu alloy foil at 900 °C temperature for the next 30 hours leads to copper sweating on outer surface of the foil, significant coarsening of the grains and formation of copper oxide-based interlayers and a considerable number of pores of 5–8 μm size (Figure 2, *e*).

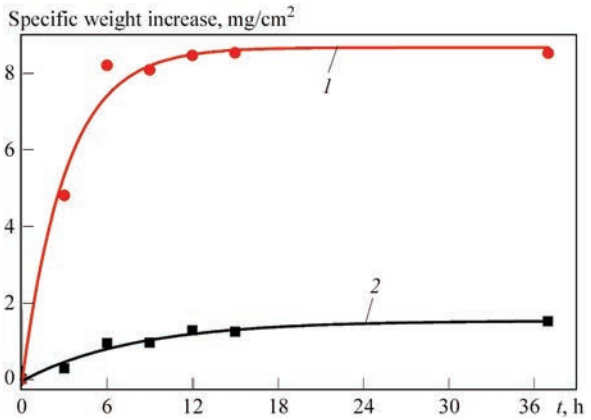

Figure 1. Kinetics of oxidation of CrFeCoNiCu (curve *1*) and CrFeCoNi alloy foils (curve *2*) at 900 °C in atmospheric air

One can also see that nickel-based oxides with loose porous structure and extremely low continuity are present on the scale surface (Figure 2, *e*). In keeping with the data of X-ray structural analysis, the scale on the foil surface consists of copper oxide (CuO) and nickel oxide (NiO) (Figure 2, *f*). We noted further "swelling" of foil during high-temperature oxidation (thickness is increased to 100–115 μm) and formation of a layered structure in the foil, which consisted of interlayers of CrFeCoNiCu phase with a lower content of copper, separated by interlayers of a copper-based phase (Figure 2, *e*). More over, it was found that oxygen is present in a significant amount not only in the surface layers, but also across the entire foil thickness.

It can be assumed that a change in the initial chemical composition of the phases occurs at the initial stages: atoms of other elements are driven from the copper-enriched phase, primarily, those insoluble with it in the solid phase, such as iron and chromium. As a result, iron atoms come to the surface and form scale, leading to rather intensive growth of sample specific weight and increase of its overall thickness (Figure 2, *c*). As this scale is unstable and is characterized by a loose structure, it breaks up (delaminates) at further heat treatment. It can account for lowering of the intensity of the specimen specific weight increase. In parallel, copper atom diffusion becomes much

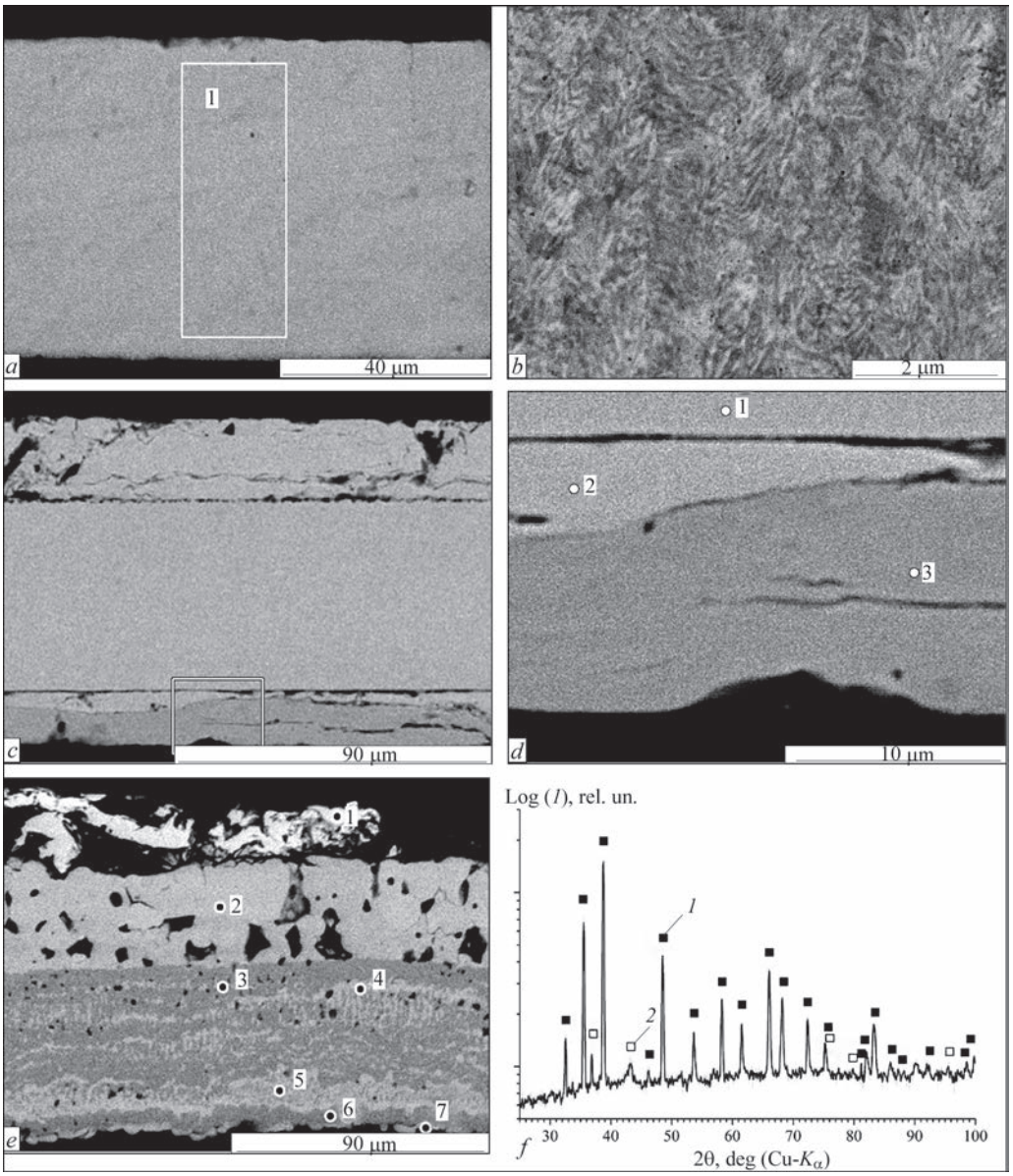

Figure 2. SEM images of cross-sectional microstructure of CrFeCoNiCu alloy foil in the initial condition (*a*, *b*) after annealing at 900 °C in atmospheric air for 6 h (*c*, *d*) and 37 h (*e*); diffraction pattern obtained from the foil surface after annealing at 900 °C in atmospheric air for 37 h (*f*): *1* — CuO; *2* — NiO. Numbers show areas where local chemical analysis was conducted (Table 1)

Table 1. Chemical composition (wt.%) of areas of CrFeCoNiCu foil in the initial condition, and after annealing at 900 °C in atmospheric air (Figure 2)

Foil condition	Area	O	Cr	Fe	Co	Ni	Cu
Initial (Figure 2, *a*)	1	–	14.12	20.38	23.05	22.53	19.92
After annealing for 6 h (Figure 2, *d*)	1	1.14	11.85	16.01	17.17	17.60	36.22
	2	1.44	8.97	16.87	17.11	18.34	37.26
	3	0.85	0.37	98.78	–	–	–
After annealing for 37 h (Figure 2, *e*)	1	1.97	–	0.63	–	97.41	–
	2	19.57	–	0.46	2.39	2.31	75.27
	3	25.44	11.36	18.79	15.7	15.63	13.08
	4	25.99	14.56	18.24	16.37	12.80	12.03
	5	22.76	11.08	11.54	18.08	20.00	16.54
	6	26.10	23.68	18.61	17.49	8.91	5.20
	7	14.43	0.58	1.83	1.83	1.20	80.13

more active under these conditions, coalescence of copper-enriched phase grains and its further refining take place, resulting in copper content increasing up to 93 wt.%.

Thus, structural changes occurring in CrFeCoNi-Cu foils during 37 h of staying at the temperature of 900 °C in air environment actually lead to destruction of the material, essentially limiting the potential

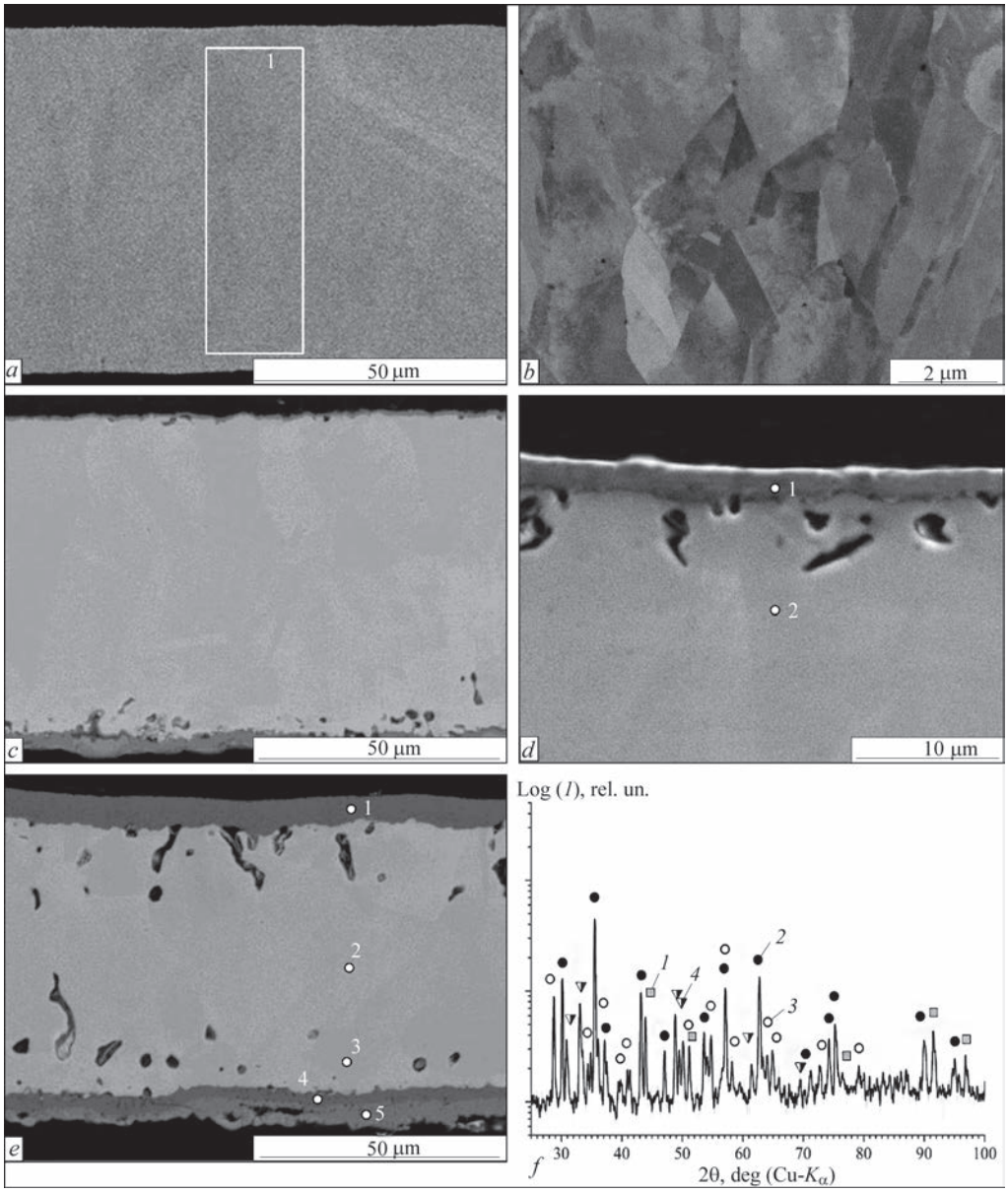

Figure 3. SEM images of cross-sectional microstructure of CrFeCoNi alloy foil in the initial condition (*a*, *b*), after annealing at 900 °C in atmospheric air for 6 h (*c*, *d*) and for 37 h (*e*); diffraction pattern obtained from foil surface after annealing at 900 °C in air for 37 h (*f*): *1* — FCC (CrFeCoNi); *2* — Fe_3O_4; *3* — Cr_2O_3; *4* — (FeCoNi)O. Numbers show the areas where local chemical analysis was performed (Table 2)

Table 2. Chemical composition (wt.%) of areas of CrFeCoNi foil in the initial condition and after annealing at 900 °C in atmospheric air (Figure 3)

Foil condition	Area	O	Cr	Fe	Co	Ni
Initial (Figure 3, *a*)	1	–	20.49	24.73	18.80	35.99
After annealing for 3 h (Figure 3, *d*)	1	33.82	58.25	3.01	1.27	3.65
	2	–	20.43	25.35	19.62	34.60
After annealing for 37 h (Figure 3, *e*)	1	33.23	13.37	27.61	11.23	14.56
	2	–	17.05	25.05	20.47	37.43
	3	–	14.87	23.21	20.92	41.00
	4	34.77	62.08	1.70	0.57	0.89
	5	30.38	13.75	32.07	11.83	11.96

service life of this high-temperature HEA. Analysis of the obtained results shows that the relatively low values of heat resistance of CrFeCoNiCu system alloys can be related, chiefly, to copper content in the foil composition. To verify this assumption under identical conditions, heat resistance testing of foils of CrFeCoNi system HEA was conducted. Investigations were performed in foil of 67 μm thickness, SEM images of the foil cross-sectional microstructure before heat treatment are given in Figure 3, *a*, *b*, chemical composition is shown in Table 2. It is found that in the first 6 h of annealing, the increase of specific weight of CrFeCoNi foils took place almost 8 times slower, compared to CrFeCoNiCu alloy foils (Figure 1, curve *2*). At further soaking of CrFeCoNi alloy foils at the temperature of 900 °C, increase of sample specific weight became considerably slower. Maximum value of specific weight increase for CrFeCoNi alloy foils after heat resistance testing was on the level of 1.5 mg/cm^2.

SEM investigations showed that scale of 3–7 μm thickness with a high degree of continuity and low defectiveness of the structure forms on the foil surfaces after 6 h of heat treatment (Figure 3, *c*, *d*). Chemical analysis of the scale revealed that it is a chromium-based oxide with a small content of other foil components (Table 2). No oxygen was found in the foil surface layers. However, pores of up to 5 μm size are observed, forming along the alloy grain boundaries. After 37 h of annealing at the temperature of 900 °C in air, the thickness of scale on the outer surfaces of CrFeCoNi alloy foil increases up to 10 μm. It was found that the scale structure is layered with a small number of defects: outer layer is represented by iron-based oxide, and inner layer is chromium-based oxide (Figure 3, *e*, Table 2).

X-ray structural analysis showed (Figure 3, *f*) that scale is formed on the base of Cr_2O_3 chromium and iron Fe_3O_4 oxides. The diffraction pattern also shows peaks from complex oxide (FeCoNi)O. No oxygen was found in the foil bulk and surface areas. More over, a significant increase of the number and size of intercrystalline pores in the foil subsurface layers was noted, which is the consequence of Frenkel effect. Foil swelling is practically absent, foil overall thickness somewhat increased to 70–72 μm. On the whole, obtained results show that such a heat treatment did not have an essential influence on the microstructure and phase composition of the foil material, and the presence of oxygen was revealed only in the subsurface layers in the formed oxide composition.

Thus, it was found that copper content in the composition of high-entropy alloys has a negative effect on the material heat resistance as a result of formation of scale based on copper and nickel oxides with a large number of defects and low degree of continuity. Copper absence in HEA composition promotes lowering of the rate of high-temperature oxidation at the temperature of 900 °C in atmospheric air by more than 8 times.

CONCLUSIONS

At testing for heat resistance at the temperature of 900 °C in atmospheric air increase of specific weight of CrFeCoNiCu alloy foil takes place 8 times more intensively than in CrFeCoNi foils. More intensive high-temperature oxidation of CrFeCoNiCu foil is associated with significant activation of copper atom diffusion, their coming to the foil surface and formation of scale with a low continuity based on CuO and NiO oxides with a large number of defects in their structure. Foils of CrFeCoNi alloy are characterized by higher values of heat resistance due to formation of scale based on Cr_2O_3 oxide on the surface with lower defect level and greater continuity.

REFERENCES

1. Ivanov, I.I., Yasinsky, K.K. (1996) Efficiency of application of heat-resistant alloys based on Ti_3Al and TiAl intermetallics for operation at 600–800 °C temperatures in aerospace engineering. *Tekhnologiya Lyogkikh Splavov*, **3**, 7–12 [in Russian].
2. Frolov, G.A., Sontsev, V.P., Tikhij, V.G., Gusarova, I.A. (2011) Advanced materials for multilayer thermal protection structures of reusable space vehicles. *Space Engineering. Rocket Arming*. Dnepropetrovsk, 133–145 [in Russian].
3. Murty, B.S., Yeh, J.W., Ranganathan, S. (2014) Chapter 2. High-entropy alloys: Basic concepts. High entropy alloys. *Butterworth-Heinemann*, 13–35. DOI: https://doi.org/10.1016/B978-0-12-800251-3.00002-X
4. Tong, C.J., Chen, M.R., Chen, S.K. et al. (2005) Mechanical performance of the Al_xCoCrCuFeNi high-entropy alloy system with multiprincipal elements. *Metallurg. and Mater. Transact. A*, **36**, 1263–1271. DOI: https://doi.org/10.1007/s11661-005-0218-9
5. Chuang, M.H., Tsai, M.H., Wang, W.R. et al. (2011) Microstructure and wear behavior of AlxCo1.5CrFeNi1.5y high-entropy alloys. *Acta Materialia*, **59**, 6308–6317. DOI: https://doi.org/10.1016/j.actamat.2011.06.041
6. Wu, Z., David, S.A., Feng, Z., Bei, H. (2016) Weldability of a high entropy CrMnFeCoNi alloy. *Scripta Materialia*, **124**, 81–85. DOI: https://doi.org/10.1016/j.scriptamat.2016.06.046
7. Dafang, W., Liming, Z., Bing, P. et al. (2016) Thermal protection performance of metallic honeycomb core panel structures in non-steady thermal environments. *Experimental Heat Transfer*, 29(**1**), 53–77. DOI: https://doi.org/10.1080/08916152.2014.940433
8. Gusarova, I.A., Parko, M., Potapov, A.M. et al. (2016) Evaluation of high temperature resistance of three-layer honeycomb panel produced from YuIPM-1200 alloy by vacuum diffusion welding, *The Paton Welding J*., **12**, 31–35. DOI: https://doi.org/10.15407/tpwj2016.12.05
9. Braeckman, B.R., Boydens, F., Hidalgo, H. et al. (2015) High entropy alloy thin films deposited by magnetron sputtering of powder targets. *Thin Solid Films*, **580**, 71–76. DOI: https://doi.org/10.1016/j.tsf.2015.02.070

10. Sobol', O.V., Andreev, A.A., Gorban, V.F. (2012) Reproducibility of the single-phase structural state of the multielement high-entropy Ti–V–Zr–Nb–Hf system and related superhard nitrides formed by the vacuum-arc method. *Technical Physics Letters*, 38(**7**), 616–619. DOI: https://doi.org/10.1134/S1063785012070127
11. Huang, P.K., Yeh, J.W., Shun, T.T., Chen, S.K. (2004) Multi-principal-element alloys with improved oxidation and wear resistance for thermal spray coating. *Advanced Engineering Materials*, **6**, 74–78. DOI: https://doi.org/10.1002/adem.200300507
12. Zhang, H., Pan, Y., He, Y. et al. (2010) Synthesis and characterization of NiCoFeCrAl3 high entropy alloy coating by laser cladding. *Advanced Materials Research*, 97(**101**), 1408–1411. DOI: https://doi.org/10.4028/www.scientific.net/AMR.97-101.1408
13. Ustinov, A.I., Polishchuk, S.S., Demchenkov, S.A., Melnichenko, T.V. (2019) Producing of thick vacuum condensates of high-entropic alloys CrFeCoNiCu and AlCrFeCoNiCu by the method of electron beam deposition. *Suchasna Elektrometal*., **2**, 13–21 [in Ukrainian]. DOI: https://doi.org/10.15407/sem2019.02.03
14. Ustinov, A.I., Polishchuk, S.S., Demchenkov, S.A. et al. (2020) Formation of thin foils of high-entropy CrFeCoNiCu alloys by EB-PVD process. *Surf. and Coat. Technol*., **403**, 126440. DOI: https://doi.org/10.1016/j.surfcoat.2020.126440
15. Ustinov, A.I., Skorodzievskii, V.S., Demchenkov, S.A. et al. (2020) Effect of the structure of vacuum condensates of high entropy alloys of Cr–Fe–Co–Ni–Cu system on their mechanical properties. *Suchasna Elektrometal*., **4**, 16–22 [in Ukrainian]. DOI: https://doi.org/10.37434/sem2020.04.03
16. Ustinov, A.I., Demchenkov, S.A., Melnychenko, T.V. et al. (2021) Effect of structure of high entropy alloys CrFeCoNiCu produced by EB PVD on their strength and dissipative properties. *J. of Alloys and Compounds*, **887**, 161408. DOI: https://doi.org/10.1016/j.jallcom.2021.161408

ORCID

A.I. Ustinov: 0000-0002-8855-3499,
S.O. Demchenkov: 0000-0002-2412-4214,
T.V. Melnychenko: 0000-0002-1460-5532,
O.Yu. Klepko: 0000-0003-2014-1938

CONFLICT OF INTEREST

The Authors declare no conflict of interest

CORRESPONDING AUTHOR

A.I. Ustinov
E.O. Paton Electric Welding Institute of the NASU
11 Kazymyr Malevych Str., 03150, Kyiv, Ukraine.
E-mail: ustinov3g@gmail.com

SUGGESTED CITATION

A.I. Ustinov, S.O. Demchenkov, T.V. Melnychenko, O.Yu. Klepko (2022) The influence of copper on the heat resistance of thin foils of high-entropy alloys of the Cr–Fe–Co–Ni–Cu system produced by electron beam physical vapour deposition method. *The Paton Welding J*., **11**, 39–44.

JOURNAL HOME PAGE

https://patonpublishinghouse.com/eng/journals/tpwj

Received: 15.07.2022
Accepted: 29.12.2022

DOI: https://doi.org/10.37434/tpwj2022.11.08

EXPRESS-EVALUATION OF THE QUALITY OF PRODUCING CATERPILLAR TRACKS BY THE RESULTS OF COERCIVE FORCE MEASUREMENT

O.P. Gopkalo[1], **O.Ye. Gopkalo**[1], **M.P. Zemtsov**[1], **Ye.V. Kovalenko**[2], **V.E. Bodunov**[1]

[1]G.S. Pisarenko Institute for Problems of Strength of the NAS of Ukraine
2 Timiryazievska Str., 01014, Kyiv, Ukraine
[2]"SPC Aviation Systems of Ukraine" LLC
8 Redutna Str., 01015, Kyiv, Ukraine

ABSTRACT

Coercimetric testing revealed essential differences in metal structure in the subsurface layer of experimental caterpillar tracks. Obtained experimental results of 4-point bend testing of experimental caterpillar tracks from steels which somewhat differ by their chemical composition, confirmed the possibility of application of nondestructive coercimetric testing for assessment of the initial structural state and level of loading of the metal, which characterizes the degree of obtained damage after loading. Metal of a sound track from steel of 110G13L type in the initial condition should have negative values of the coercive force that is ensured by its optimal structural state. This circumstance can provide substantiation for introducing coercimetric testing for express-evaluation of the quality of castings and their heat treatment.

KEYWORDS: caterpillar tracks, structuroscope, coercive force, structural state

INTRODUCTION

Mechanical properties of metal products depend on its composition and structural state. In this work there was used a nondestructive magnetic method for evaluation of quality of structural state of metal of experimental caterpillar tracks of Hadfield type austenite steel (with some deviation of composition) in initial condition as well as after standard 4-point bend testing by the results of coercive force measurement. Coercive force is an integral characteristic of a structural state of metal which depends on content and concentration of chemical elements in metal and phase and structural constituents.

Table 1 provides composition of Hadfield type steel (110G13L steel grade according to DSTU 8781:2018).

Steel 110G13L has typical for austenite steels toughness and ductility at sufficiently high strength. At low hardness 110G13L steel has extremely high wear resistance at friction with pressure and impacts. This is explained by strengthening (hardening) of austenite at plastic deformation in process of work, i.e. this steel has increased tendency to hardening (sufficiently higher than in common ones with the same hardness). Presence of significant ductility margin of steel 110G13L allows redistributing the stresses of the most loaded areas of the track that provides high integrity of the product.

Hardening results in increase of wear resistance, therefore steel 110G13L is difficult to treat by cutting tools and parts from it are mostly produced by casting without mechanical treatment. Under conditions of purely abrasive wear (for example, at sand friction) there is no effective hardening of steel 110G13L that leads to increase of parts wear-out. Due to unique mechanical properties steel 110G13L has found wide application in manufacture of wear-resistant parts of machines.

PURPOSE OF WORK

Lies in experimental check of the possibility of application of coercimetric testing for express-evaluation of the quality caterpillar tracks manufacture.

INFLUENCE OF COMPOSITION AND STRUCTURAL STATE ON MECHANICAL PROPERTIES OF 110G13L STEEL

Regardless the fact that strength, ductility and wear resistance of high-manganese steels to a great extent

Table 1. Composition of steel 110G13L according to DSTU 8781:2018

Weight fraction, %								
C	Si	Mn	Cr	Ni	Cu	S	P	Fe
0.9–1.4	0.3–1.0	11.5–15.0	Up to 1.0	Up to 1.0	Up to 0.3	Up to 0.05	Up to 0.2	~83

Table 2. Dependence of mechanical properties of steel 110G13L of different manufacturers on composition (standard values are given in brackets)

Composition, %	Manufacturer						
	No. 1	No. 2	No. 3	No. 4	No. 5	No. 6	No. 7
C (0.9–1.4)	0.98	0.94	1.05	1.15	0.95	0.97	1.05
Mn (11.5–15)	11.60	10.50	12.69	13.13	13.47	12.35	13.40
Si (0.8–1)	0.66	0.64	0.46	0.51	0.44	0.51	0.44
Cr (up to 1.0)	0.10	0.59	0.15	0.39	0.14	0.13	0.11
Ni (up to 1.0)	0.18	0.27	0.20	0.16	0.21	0.16	0.27
P (up to 0.12)	0.025	0.057	0.029	0.048	0.025	0.028	0.027
S (up to 0.05)	0.012	0.004	0.005	0.004	0.007	0.006	0.005
Cu (up to 0.3)	0.18	0.17	–	–	0.17	0.12	0.19
Characteristics							
σ_b, MPa	790	610	710	660	850	790	690
$\sigma_{0.2}$, MPa	370	400	440	455	350	375	355
δ, %	38	21.5	24.5	21.5	43	37	27
ψ, %	29	18.5	41	29	39	37	31
KCU^{20}, J/cm^2	242	265	325	234	261	258	262
KCU^{-60}, J/cm^2	90.5	39	159	45	–	–	–
Hardness, *HB*	202	202	187	187	–	–	–
Grain size number	3	1	1	0	–	–	–

are determined by DSTU and technical conditions of different suppliers, sufficiently wide variation of content in metals is allowed even of such main alloying elements as C, Mn, Si, S, P that is clearly not justified [1]. To increase wear resistance of castings of 110G13L steel its alloying with titanium (to 0.05 %), vanadium (to 0.3 %), molybdenum (to 0.2 %) [2] is allowed. Vanadium alloying increases up to 30 % wear resistance and decreases cold resistance, however affects strength characteristics.

It is determined that addition of 2 % of vanadium to 110G13L steel results in five times increase of wear resistance at conservation of impact toughness. Chromium alloying (to 1.5 %) [2] rises strength and wear resistance properties of steel. At that ductility and toughness are little bit reduced, however remain at the level that exceeds these characteristics for common high-manganese steel and provide normal operation of products with increase of wear resistance on average at 15–20 %. In other words, desired indices of wear resistance can be significantly increased [3] at up to 1.0 % chromium alloying of steel 110G13L (within the limits of DSTU requirements).

Increase of content of Cr, Si, Ni, Cu and decrease of Mn concentration in metal provoke rise of the coercive force values. Content in steel of carbon in 0.9–1.0 % limits and phosphorous not more than 0.5–0.55 % minimizes impact toughness. Increase in steel of silicon content decreases impact toughness. Maximum indices of impact toughness at 0.5 % silicon content [3].

The main problem for production of quality castings is selection of casting technology and heat treatment. Quality heat treatment is a key factor for obtaining the desirable metal structures.

Heat treatment of steel 110G13L is regulated by DSTU 8781:2018 — austenization at 1050–1100 °C temperature with cooling in cold water (not more than 30 °C). It should be noted that columnar and dendritic cast structure can not be completely removed by heat treatment and has negative effect on impact toughness, resistance to abrasive wear and dynamic loadings. Increase of hardness promotes increase of coercive force values [2].

Table 2 gives the data [4] of dependence of mechanical properties of steel 110G13L of different manufacturers on composition.

Provided results show that difference of composition of the track metal of different manufacturers promotes scatter of mechanical characteristics on average in the following limits, namely σ_b — 32.9 %; $\sigma_{0.2}$ — 26.1 %; δ — 66.7 %; ψ — 65.6 %; KCU^{20} — 32.6 %; KCU^{-60} — 121.2 %; hardness, *HB* — 7.7 %. Concentration of Mn and Si is lower of the standard values in castings of manufacturer No. 2, promotes the most decrease of strength characteristics σ_b, relative constriction at tension ψ and impact toughness *KCU* at –60 °C in relation to similar indices of metal of castings of other manufacturers [4].

Dependence of Mn/C index for steel 110G13L shows that its growth rises impact toughness. It is believed that the optimum relationship of Mn/C is not less than 10.0. The maximum indices of impact toughness are reached at Mn/C relationship in 12—13 range. P + 0.4C index characterizes an effect of phosphorous which is desirable to be not more than 0.5 %.

Increase of this index for steel 110G13L promotes decrease of impact toughness. At P+0.4C more than 0.5 % the steel is susceptible to crack formation [1].

Nondestructive methods of testing are widely used for diagnostic of the quality of structural state of the products metal in initial condition and evaluation of metal damageability in process of structure operation. Work [5] provides the example of diagnostics of the level of damageability of metal of the caterpillar tracks at their standard 4-point bend testing. The tracks with optimum structural state of metal (austenitic structure) are characterized with absence of magnetic properties of metal in initial condition and, respectively, zero values of coercive force. Elastic-plastic loading deformation provokes increase of the coercive force values and distribution diagrams look like approaching the circle.

Since coercive force is an integral characteristic of metal structural state which depends on content and concentration of elements, phase and structural constituents then application of coercimetric testing allows express-evaluation of the tracks metal quality.

PROCEDURE OF EXPERIMENTAL INVESTIGATIONS

The experimental investigations lied in determination of distribution of the values of coercive force along a surface of 13 experimental caterpillar tracks of steel 110G134L (with some deviation of composition from regulated one) of two different manufacturers in initial state and after 4-point bend testing.

Figure 1 shows the general view of tracks before testing with digital identification of points for further measurement of the coercive force.

Measurement of the coercive force on the track surface in the typical points was carried out using structuroscope KRM-Ts-K2M (developer "Special Scientific Engineering LLC", Kharkiv). Since the tracks have complex volumetric configuration with internal cavity (at wall thickness 4–5 mm), then a compact probe D12 with measurement base 12×12 mm and magnetization depth to 1 mm was used for measurement of the coercive force with registration of possible hardening of the surface layers of metal under operation. Application of such probe allows measurement of the values of coercive force in very limited local areas of the track, which has sufficiently complex surface geometry. Measurement of the values of coercive force with D12 probe showed presence of significant scatter of H_c in the different points of the experimental track surface. In this work in order to obtain more integral values of the coercive force in significantly larger volumes of metal (27×25×4 mm) D27 probe was used. It has measurement base of 27 mm and magnetization depth to 4 mm that allows significantly reducing scatter of the measured values.

Measurement of the coercive force lies in initial magnetization of the metal till saturation with the following next complete demagnetization and further magnetization with magnetic field of opposite polarity for neutralizing the residual magnetism and measurement of H_c values. Duration of a cycle for coercive force determination makes 10 s. It should be noted that in presence of anisotropy of the metal structure, including after plastic deformation, the values of coercive force in the investigated points are changed at variation of measurement directions (orientation of magnetic poles of the probe relatively to the examined surface). Due to this measurement of H_c values was carried out at each 45° turn relatively previous measurement (in total 8 measurements at orientations: 0, 45, 90, 135, 180, 225, 270, 315°), where a direction of measurement of the values of coercive force $H_{c\text{II}}$ (0, 180, 360°) was taken across the track (along the track chain) and $H_{c\perp}$ (90, 270°) — along the track (across the track chain). Measurement of the values of coercive force in typical points of the surface of the tracks was carried out in initial condition and after standard 4-point bend tests.

Testing of tracks in initial condition for 4-point static bending was carried out on tensile-testing machine ZD-40. Loading was performed normal to a track plane as well as along the line tangent to it according to the schemes on Figure 2. First loading of P1 = 300 kN force was carried out normal to the track plane (Figure 2, *a*). If after such loading there were not found the signs of loss of metal integrity (crack appearance), regardless the presence of the residual stresses, then the track was loaded with P2 = –300 kN force (in direction opposite to a force application relatively to first loading (Figure 2, *b*). The next shear

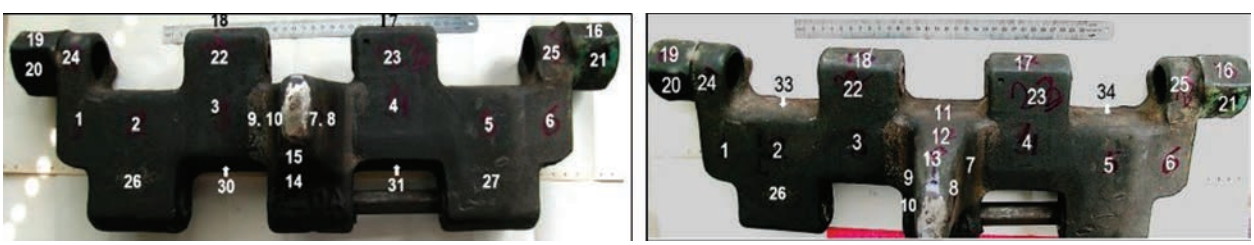

Figure 1. General view of tracks before testing

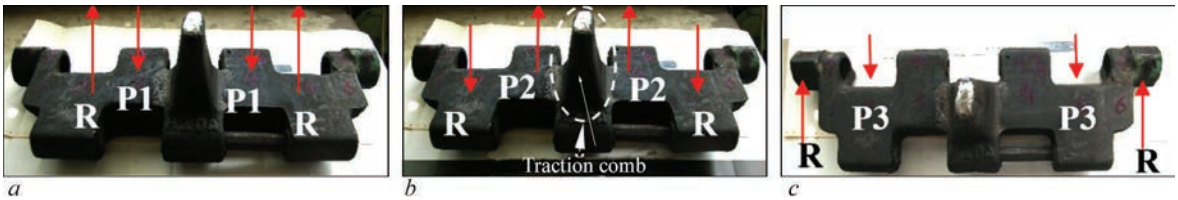

Figure 2. Schemes of loading of track at 4-point static bend tests [5]

loading at 4-point force application after previous loadings was carried out along the tangent line to the track plane of P3 = 240 kN force (Figure 2, *c*).

Under operation conditions the track is affected by roller forces (P) which being equalized by ground pressure (R). In this case the scheme of track loading corresponds to 4-point bend. Operation provokes deformation and hardening of the metal surface layers, including due to contact stresses, taking into account a traction guide lug, which takes forces of a drive gear and the side forces from the suspension rollers during manoeuvres of a vehicle. Nonuniform stress-strain state of different track sections occurs under operation conditions and at bend tests. The most deformed are the metal surface layers. However, due to high ductility of metal in initial condition of the steel as a result of ductility deformation during operation there is a redistribution of stresses in the most stressed areas with neighbor areas that provides structure integrity.

A reference caterpillar track and the experimental tracks, made of metal with some deviations of composition from standard one (tracks Nos 1–4 (2021), Nos 7–8 (2020) 1–5 (2021) and ZP-1, ZP-2 (2021) were subjected to 4-point bend tests. Year of test is given in brackets.

Analysis of composition of the tracks metal was carried out on photoelectric spectrometer Spectrovac-1000 (Baird). Composition of metal of the investigated tracks and steel 110G13L is given in Table 3.

As can be seen from Table 3 the examined experimental tracks from different manufacturers vary by percent of certain chemical elements (C, Si, Mn, Cr, P) between themselves as well as from ones regulated by the normative documents for steel 110G13L.

RESULTS OF EXPERIMENTAL INVESTIGATIONS AND THEIR ANALYSIS

Present work provides the results of comparison of structural state of metal of the experimental caterpillar tracks of different manufacturers with the reference one by the results of coercive force measurement. Figure 3 shows the typical distribution diagrams of coercive force measured with structurescope in the different points of surface of the reference track in initial condition and after testing in different planes. It should be noted that in the main part of the track (for example, points 1–6, Figure 3, *a*) after three loadings by schemes 1–3 (Figure 2) there were no dramatic changes of the structural state where the value of coercive force was equal zero. The most loaded is the metal of traction comb (points 8, 9, Figure 3, *b*) and points 33 and 34 (Figure 3, *c*) in the main part of the track.

Microstructure of fragments of the examined reference track in initial condition in different zones is characterized with austenite of mixed grain-dendrite morphology (cast structure) (Figure 4, *a*) and austenite of grain morphology (Figure 4, *b*) without the signs of microplastic deformation.

The reference track with optimum structural state of metal (austenitic structure, Figure 4) in initial condition is characterized with absence of magnetic properties that is proved by the coercive force measurements (H_c = 0 A/cm). In contrast to the reference track the different areas of the experimental tracks 1–4 (2021) in initial condition had sufficiently high values of coercive force that is related with appearance of ferromagnetic phases.

Concerning the microstructure of other examined samples, despite different grains, etching revealed

Table 3. Composition of metal of examined caterpillar tracks and steel 110G13L

Track number	Weight fraction, %										
	C	Si	Mn	Cr	Ni	Cu	Mo	Ti	V	S	P
Standard	1.09	0.91	13.3	0.90	0.96	0.21	0.19	0.015	0.068	0.014	0.035
1–4 (2021)	1.04	1.25	2.30	1.52	0.33	0.16	<0.1	<0.05	0.036	0.02	0.15
1–5 (2021)	0.44	0.75	15.8	0.71	0.72	0.11	0.056	0.017	0.006	0.015	0.019
7–8 (2020)	0.66	0.34	12.6	0.63	0.18	0.11	0.038	<0.01	0.017	0.016	0.070
ZP-1, ZP-2	0.35	0.42	16.8	1.10	0.080	0.045	0.055	<0.01	0.022	0.013	0.028
Steel 110G13L (DSTU 8781:2018)	0.9–1.5	0.3–1.0	11.5–14.5	1.0 not more than	1.0 not more than	–	–	–	–	0.05	0.12
GOST 2176–77	0.9–1.4	0.8–1.0	11.5–15.0	Up to 1	Up to 1	Up to 0.3	–	–	–	Up to 0.05	Up to 0.12

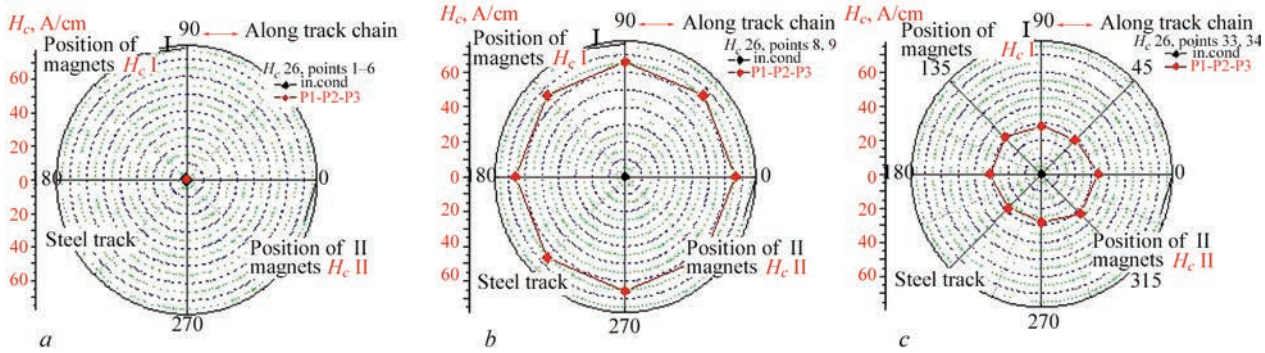

Figure 3. Typical distribution diagrams of the coercive force in different points of surface of the reference track in initial condition and after tests: *a* — points 1–6; *b* — points 8, 9; *c* — points 33, 34. H_c values in initial condition are shown by black and after loading by red. Number of points corresponds to Figure 1

the surface layers (of 300–400 μm thickness) with the signs of microplastic deformation (Figure 5, *a*) in addition to austenite grain morphology. Martensite (α-phase) in different amount respectively for each of the examined samples was detected in the austenite grains of hardened layers between the slip bands. It explains appearance of ferromagnetic properties in these samples of austenite steel. It was found that the values of coercive force rises with increase of portion of α-phase, percent of which was determined using ferritometer of local type Ferrit Gehalt-messer-1.053.

Absence of increase of the coercive force at regulated loads by scheme 1 (Figure 2, *a*) corresponding to the initial condition indicates invariability of structural state of metal at deformation (Figure 6). It is necessary to note the significant scatter of the absolute values of coercive force in the subsurface layers of the different tracks that is a reflection of metal structural state. Thus, within the range of batch of tracks 1–4 (2021): for metal of track No. 1 the absolute values of coercive force of different areas lied in the limits of 21.1–70.5 A/cm; track No. 2 — 29.7–77.6 A/cm; track No. 3 — 4.6–68.1 A/cm; track No. 4 — 14.2–62.7 A/cm.

4-point bend tests showed that tracks 1–4 (2021) withstood only 50 % of the reference load, in other words metal had very low resistance to such loading. At that failure had brittle nature without the signs of

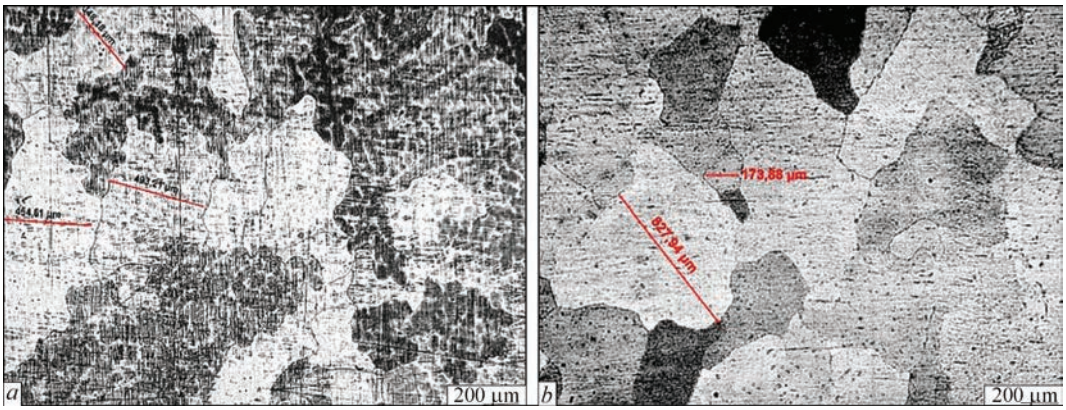

Figure 4. Example of microstructure of fragments of the examined reference track in initial condition in different zones (α-phase ~ 0 %, H_c = 0 A/cm)

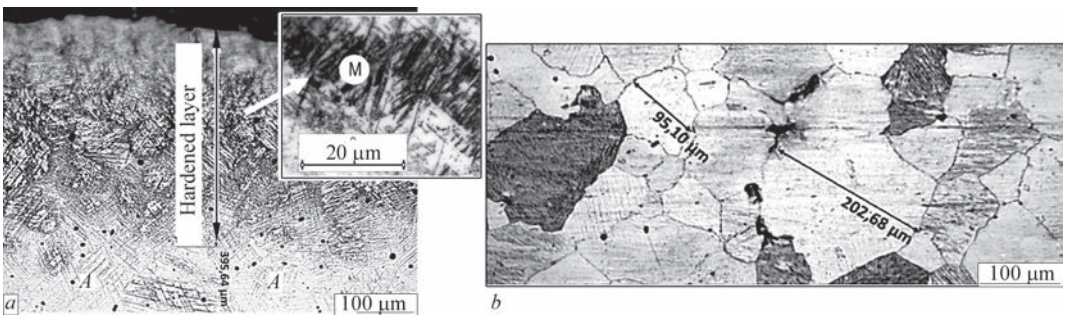

Figure 5. Examples of typical microstructure of the examined experimental tracks (in the cross-section) in initial condition in different zones: *a* — near-boundary (hardened) layer, α-phase ~ 0.3–0.6 %, H_c = 35 A/cm; *b* — austenite base, α-phase ~ 0 %, H_c = 0 A/cm; M — martensite (α-phase)

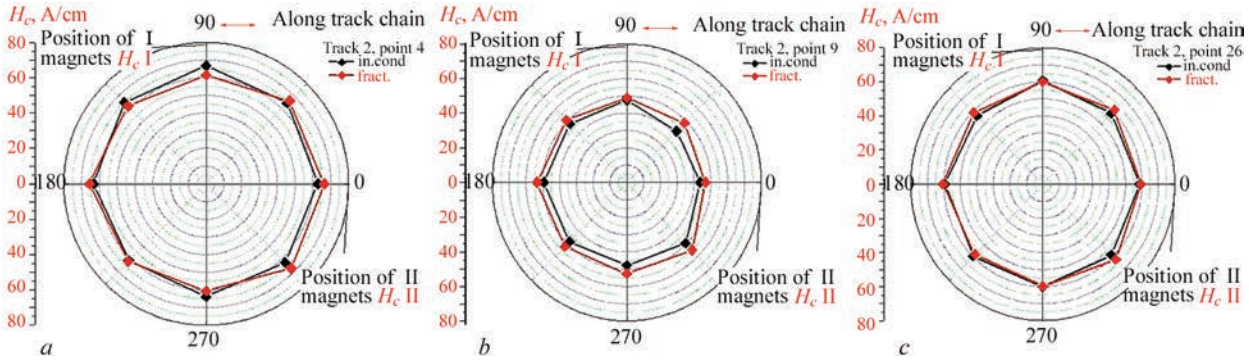

Figure 6. Typical distribution diagrams of the coercive force in different points of surface of the experimental tracks 1–4 (2021) in initial condition and after tests by scheme 1 (Figure 2, *a*): *a* — point 4; *b* — point 9; *c* — point 26

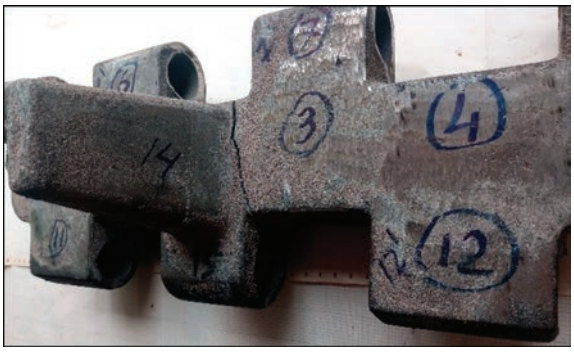

Figure 7. General view of integrity loss (crack formation) of metal of tracks 1–4 (2021) after 4-point bend tests

plastic deformation (including the presence of residual deflection (Figure 7)).

In contrast to the examined tracks 1–4 (2021) the structural state of the experimental tracks 1–5 (2021) (Figure 8) differs by presence of the zones with zero values of coercive force that is typical for austenite structure. Examined tracks 1–5 (2021) as well as tracks 1–4 (2021) are characterized with absence of increase of the values of coercive force at rated loads relatively to the initial condition that indicates invariability of the metal structural state at deformation. A brittle nature of fracture proves absence of metal ductility margin. At that the tracks at loading by schemes 1 and 3 (Figure 2, *a*, *c*) withstood rated loading. At loading by scheme 2 (Figure 2, *b*) the track withstood only 17.7 t of 30 t being rated.

Insignificant increase of the values of coercive force at loading and appearance of plastic deformation signs (slip bands) were found on the surface of tracks 7–8 (2020) in contrast to the mentioned above tracks 1–5 (2021) and 1–4 (2021). At that the tracks withstood the rated loadings with certain values of residual deflection in corresponding planes of the loading. Figure 9 demonstrates the typical distribution diagrams of coercive force in the different points of the surface of experimental tracks 7–8 (2020) in initial condition and after 4-point bend tests.

It also necessary to note a scatter of the absolute values of coercive force, which in initial condition for the experimental tracks 7–8 (2020) lied in 14.3–67.1 A/cm range. However, increase of the values of coercive force took place after tests in the most loaded points of the tracks that allowed evaluating the level of metal damage in deformation [5].

Examined tracks of the other manufacturer (tracks ZP-1 and ZP-2) are also characterized with presence of sufficiently high values of the coercive force and their non-uniform distribution in the different points in initial condition (Figure 10). For comparison Figure 10 shows also the distribution diagrams of coercive force after the rated loadings.

Structural state of metal of tracks ZP-1 and ZP-2 in initial condition, evaluated by the value of coercive force, corresponds approximately to tracks 1–5

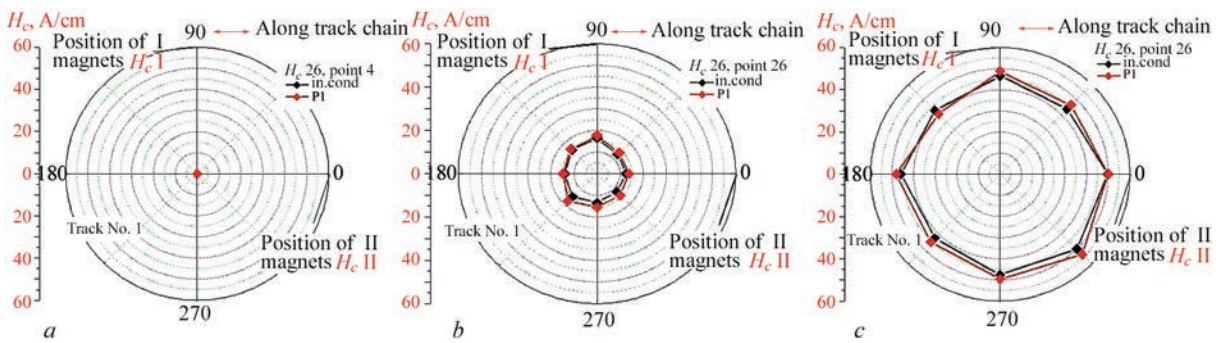

Figure 8. Typical distribution diagrams of the coercive force in different points of surface of experimental tracks 1–5 (2021) in initial condition and after tests: *a* — track No. 1 point 4; *b* — tracks No. 2 point 6; *c* — track No. 1 point 26. H_c values in initial condition are shown by black and after loading by red

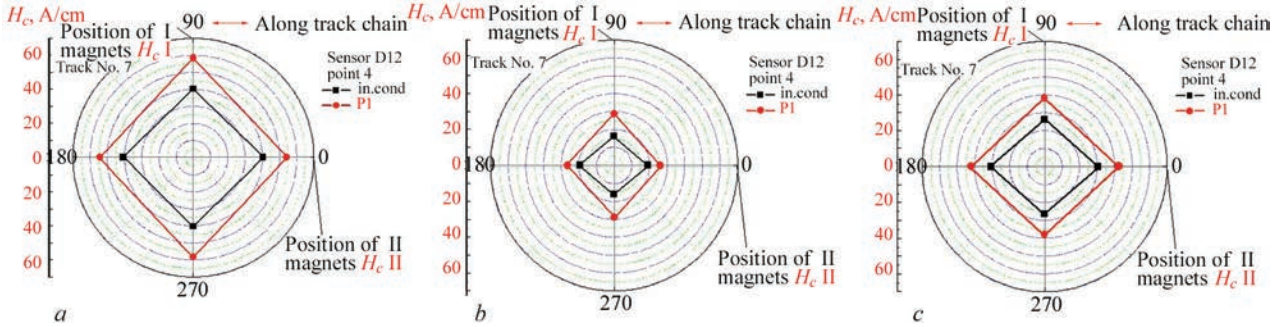

Figure 9. Typical distribution diagrams of the coercive force in different points of surface of experimental track 7–8 (2020) in initial condition and after tests: *a* — point 4; *b* — point 9; *c* — point 26. H_c values in initial condition are shown by black and after loading by red

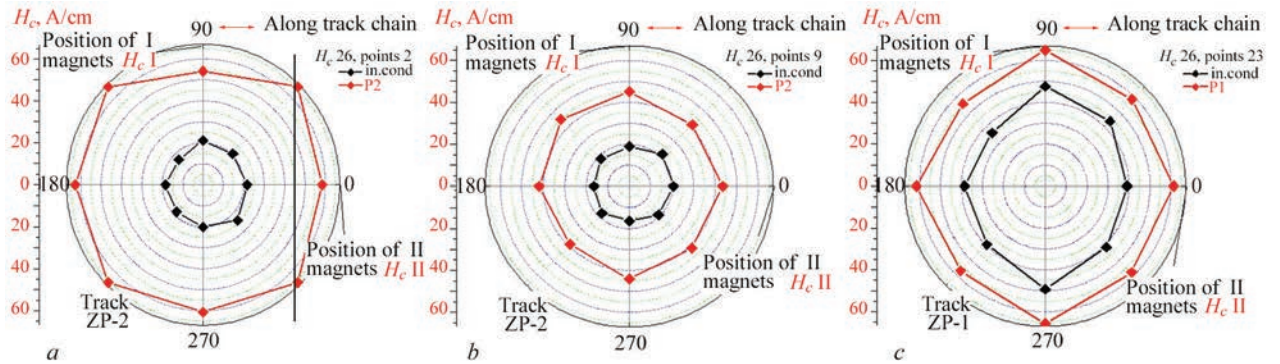

Figure 10. Typical distribution diagrams of the coercive force in different points of surface of experimental tracks ZP-1 and ZP-2 in initial condition and after tests: *a* — track ZP-2 point 2; *b* — track ZP-2 point 9; *c* — track ZP-1 point 23. H_c values in initial condition are shown by black and after loading by red

(2021), 1–4 (2021) and 7–8 (2020). However, for metal of tracks ZP-1 and ZP-2 significant increase of the values of coercive force is typical under the rated loadings relatively initial condition. Significant deformation of tracks took place at 4-point bend loading. Metal had sufficient ductility margin for deformation that resulted in redistribution of loads in the most loaded zone and increased fracture resistance. On loading of tracks ZP-1 and ZP-2 by schemes 1 and 2 (Figure 2, *a*, *b*) plastic deformation started in 24.6 t loading and fracture at 28.9 t.

The authors [1] based on the systematic researches proposed the optimum indices of relationship of elements for steel 110G13L, namely Mn/C ≤ 10 and P + 0.4C ≥ 0.5 %, where growth of Mn/C index provokes increase of impact toughness and the optimum values of Mn/C are in 12–13 range. Rise of P + 0.4C index above 0.5 % provokes increase of steel susceptibility to crack formation.

Indices Mn/C and P + 0.4C of metal of investigated by us tracks in comparison with the optimum ones [1] are represented in Table 4.

Thus, the metal of all examined experimental tracks does not correspond to the requirements as for composition of steel 110G13L according to reference documents (Table 3) and as for the optimum ranges of indices Mn/C and P + 0.4C (Table 4), that found representation on the distribution diagrams of coercive force of the experimental tracks in initial condition.

In addition to the outlined above possibilities of application of the coercimetric testing the developed approach can be used for evaluation of quality of the products of austenite steels for determination of damages obtained in the process of testing or operation [6, 7]. According to it in monitoring of the structural state it is necessary to pay attention not on the maximum values of coercive force, but on process kinetics. Due to static or cyclic operating time the dependence of coercive force on accumulated damages has ascending and descending areas. An area of increase of the coercive force values corresponds to crack nucleation stage and area of their values decrease matches with the stage of crack propagation due to metal integrity loss at pores and crack formation.

Use of coercimetric testing allows performing evaluation of the metal quality in initial condition as well as the level of loading and obtained damages at any of stages in any point of products under operation

Table 4. Indices Mn/C and P + 0.4C of metal of examined tracks in comparison with optimum ones [1]

Index	[1]	Reference	1–4 (2021)	7–8 (2020)	1–5 (2021)	ZP-1, ZP-2
Mn/C	12–13	12.2	2.21	19.1	35.9	48.0
P+0.4C, %	≤0.5	0.471	0.566	0.334	0.195	0.164

condition by means of measurement of the coercive force values.

CONCLUSIONS

There were carried out a nondestructive testing diagnostics of a structural state (by coercive force measurements) of metal of 13 experimental caterpillar tracks of different manufacturers in initial condition and after standard 4-point bend tests.

The structural state of metal of ZP-1 and ZP-2 tracks in initial condition, evaluated by the value of coercive force approximately corresponds to tracks 1–5 (2021), 1–4 (2021) and 7–8 (2020). However, metal of tracks ZP-1 and ZP-2 is characterized with significant increase of the values of coercive force at rated loads relatively initial condition. Significant deformation of the tracks took place at 4-point bend loading. The metal had sufficient ductility margin for deformation that promoted redistribution of loads in the most loaded zone and increased fracture resistance.

In contrast to the reference track the various areas of the experimental tracks 1–4 (2021) and 1–5 (2021) in initial condition had sufficiently high values of coercive force that is related with unconformity of composition and heat treatment to the reference requirements. The metal of mentioned tracks had understated ductility that did not contribute to redistribution of the maximum stresses in the most loaded areas and resulted in brittle fracture after standard 4-point bend tests.

It also necessary to note scatter of the absolute values of coercive force, which in initial condition for experimental tracks 7–8 (2020) lied in 14.3–67.1 A/cm range. However, the most loaded points of the tracks after tests demonstrated increase of the coercive force values that allows evaluating the level of metal damage in deformation [5].

Obtained experimental results of 4-point bend tests of the experimental tracks of austenite steel of Hadfield type with certain deviations of composition from the regulated one proved the possibility of application of nondestructive coercimetric testing for evaluation of initial structural state and level of loading of metal which characterizes the level of obtained damages after loading by the results of coercive force measurement.

REFERENCES

1. Davydov, N.G. (1979) *High-manganese steel*. Moscow, Metallurgiya [in Russian].
2. Solntsev, Yu.P., Andreev, A.K., Grechin, R.I. (1991) *Cast cold-resistant steels*. Moscow, Metallurgiya [in Russian].
3. Zimokos, G.N., Adamenko, L.A., Ivanova, L.Kh. (2011) Influence of chemical composition on the properties of high-manganese steel in armored steel castings of cone crushers. *Metallurgicheskaya i Gornorudnaya Promyshlennost,* **4**, 140 [in Russian].
4. Sharov, N.V., Platonov, A.V., Chumakov, V.A. (2012) Production and quality assessment of castings of rapidly-wearing parts from high-manganese steels. *Gornaya Promyshlennost*, **3**, 18–28 [in Russian].
5. Gopkalo, O.P., Zemtsov, M.P., Gopkalo, O.Ye. et al. (2021) Diagnosis of damage to caterpillar tracks under mechanical loading based on the results of measurement of the coercive force. *Tekh. Diahnost. ta Neruiniv. Kontrol,* **1**, 17–26 [in Ukrainian]. DOI: https://doi.org/10.37434/tdnk2021.01.03
6. Gopkalo, O.P., Nekhotiashchiy, V.O., Bezludko, G.Ya. et al. (2019) Giagnosis of damage in austenitic steel AISI 304 at mechanical loading by measurements of coercive force. *Tekh. Diahnost. ta Neruiniv. Kontrol*, **4**, 12–24 [in Ukrainian]. DOI: https://doi.org/10.37434/tdnk2019.04.01
7. Gopkalo, O., Bezlyudko, G., Nekhotiashchiy, V. et al. (2020) Damage evaluation for AISI 304 steel under cyclic loading based on coercive force measurements. *Int. J. Fatigu*e, **139.** DOI: https://doi.org/10.1016/j.ijfatigue.2020.105752

ORCID

O.P. Gopkalo: 0000-0001-7799-3870

CONFLICT OF INTEREST

The Authors declare no conflict of interest

CORRESPONDING AUTHOR

O.P. Gopkalo
E.O. Paton Electric Welding Institute of the NASU
11 Kazymyr Malevych Str., 03150, Kyiv, Ukraine.
E-mail: apg1947@ukr.net

SUGGESTED CITATION

O.P. Gopkalo, O.Ye. Gopkalo, M.P. Zemtsov, Ye.V. Kovalenko, V.E. Bodunov (2022) Express-evaluation of the quality of producing caterpillar tracks by the results of coercive force measurement. *The Paton Welding J*., **11**, 45–52.

JOURNAL HOME PAGE

https://patonpublishinghouse.com/eng/journals/tpwj

Received: 06.10.2022
Accepted: 29.12.2022